BRUSH-LIKE POLYMERS: NEW DESIGN PLATFORMS FOR SOFT, DRY MATERIALS WITH UNIQUE PROPERTY RELATIONS

William Francis McKemie Daniel Jr.

A dissertation submitted to the faculty at the University of North Carolina at Chapel Hill in partial fulfillment of the requirements for the degree of Doctor of Philosophy in Chemistry in the University of North Carolina at Chapel Hill.

Chapel Hill
2017

Approved by:

Sergei S. Sheiko

Michael Rubinstein

Stephen L. Craig

Valerie S. Ashby

Wei You

© 2017
William Francis McKemie Daniel Jr.
ALL RIGHTS RESERVED

ABSTRACT

William Francis McKemie Daniel Jr.: Brush-Like Polymers: New Design Platforms for Soft, Dry Materials with Unique Property Relations
(Under the direction of Sergei S. Sheiko)

Elastomers represent a unique class of engineering materials due to their light weight, low cost, and desirable combination of softness (10^5-10^7 Pa) and large extensibilities (up to 1000%). Despite these advantages, there exist applications that require many times softer modulus, greater extensibility, and stronger strain hardening for the purpose of mimicking the mechanical properties of systems such as biological tissues. Until recently, only liquid-filled gels were suitable materials for such applications, including soft robotics and implants. A considerable amount of work has been done to create gels with superior properties, but despite unique strengths they also suffer from unique weaknesses. This class of material displays fundamental limitations in the form of heterogeneous structures, solvent loss and phase transitions at extreme temperatures, and loss of liquid fraction upon high deformations. In gels the solvent fraction also introduces a large solvent/polymer interaction parameter which must be carefully considered when designing the final mechanical properties. These energetic considerations further exaggerate the capacity for inconstant mechanical properties caused by fluctuations of the solvent fraction. In order to overcome these weaknesses, a new platform for single component materials with low modulus ($<10^5$ Pa) must be developed. Single component systems do not suffer from compositional changes over time and display more stable performance in a wider variety of temperatures and humidity

conditions. A solvent-free system also has the potential to be homogeneous which replaces the large energetic interactions with comparatively small architectural interaction parameters.

If a solvent-free alternative to liquid-filled gels is to be created, we must first consider the fundamental barrier to softer elastomers, i.e. entanglements - intrinsic topological restrains which define a lower limit of modulus (~10^5 Pa). These entanglements are determined by chemistry specific parameters (repeat unit volume and Kuhn segment size) in the polymer liquid (melt) prior to crosslinking. Previous solvent free replacements for gels include elastomers end-linked in semidilute conditions. These materials are generated through crosslinking telechelic polymer chains in semidilute solutions at the onset of chain overlap. At such low polymer concentrations entanglements are greatly diluted and once the resulting gel is dried it creates a supersoft and super-elastic network. Although such methods have successfully generated materials with moduli below the 10^5 Pa limit and high extensibilities (~1000%) they present their own limitations. Firstly, the semidilute crosslinking methods uses an impractically large volume of solvent which is unattractive in industry. Second, producing and crosslinking large monodisperse telechelic chains is a nontrivial process leading to large uncertainties in the final network architecture and properties. Specifically, telechelics have a distribution of end-to-end distances and in semidilute solutions with extremely low fraction of chain ends the crosslink reaction is diffusion limited, very slow, and imprecise. In order to achieve a superior solvent-free platform, we propose alteration of mechanical properties through the architectural disentanglement of brush-like polymer structures.

In recent year there has been an increase in the synthetic conditions and crosslinking schemes available for producing brush-like structures. This makes brush-like materials an attractive alternative to more restrictive methods such as end-linking. Standard networks have one major control factor outside of chemistry, the network stand length. Brush-like architectures are

created from long strands with regularly grafted side chains creating three characteristic length scales which may be independently manipulated. In collaboration with M. Rubinstein, we have utilized bottlebrush polymer architectures (a densely grafted brush-like polymer) to experimentally verify theoretical predictions of disentangled bottlebrush melts. By attaching well-defined side chains onto long polymer backbones, individual polymer strands are separated in space (similar to dilution with solvent) accompanied by a comparatively small increase in the rigidity of the strands. The end result is an architectural disentangled melt with an entanglement plateau modulus as much as three orders of magnitude lower than typical linear polymers and a broadly expanded potential for extensibility once crosslinked.

Disentangled brush-like molecules are well suited to create biologically soft materials. However such architectures possess multiple characteristic length scales, making quantitative analysis of their structures challenging. Because of their large molecular dimensions, densely grafted bottlebrush structures can be readily measured by molecular imaging techniques. We have combined AFM with other methods to characterize the important molecular parameters of n_{bb} (degree of polymerization (DP) of the backbone) and n_{sc}/n_g (number of side chains monomers per backbone monomer). This technique allows for fast and accurate analysis of molecules for comparison with theory and computer simulation. Taking the analysis one step further, we have also explored the behavior of bottlebrush molecules with bimodal side chain distributions on 2D surfaces. We have shown that side chain adsorption is a statistically random process leading characterizing the adsorbed side chain population as the weight average of all side chains (adsorbed and unadsorbed). This discovery allowed for extraction of the side chain dispersity data using molecular widths taken from Langmuir-Blodgett film AFM analysis.

With the architectural and entanglement properties of the brush-like architectures characterized we turned to designing supersoft elastomers (modulus $<10^5$ Pa). There are two approaches to consider when forming elastomers: (1) chemical crosslinking which offers ease of synthesis and superior environmental stability, and (2) physical crosslinking which allows for reversible self-assembly, molding of complex shapes, and greater control over mechanical performance via microphase separation effects. We first turned to chemical crosslinking in order to explore the potential of simple bottlebrush elastomers. An elastomer series was synthesized with changing network strand degree of polymerization (DP) (n_x) and side chain DP (n_{sc}) using a radical based polymerize-through method. This synthetic technique allowed for bulk polymerization of prefabricated mono-functional side chains (macromonomers) and bifunctional crosslinkers. The resulting networks possessed uniform structures in terms of mesh size and grafting density and could be molded into experimentally useful shapes. The samples were subjected to mechanical testing and analyzed using a universal stress-strain relation developed by A. Dobrynin. It was discovered that the stress evolution of bottlebrush networks could be completely described by two key parameter: the network modulus and the network pre-extension factor (β). The materials' network modulus displayed a linear dependence on network strand DP and side chain DP allowing for easy tuning of modulus from 10^2 to 10^4 Pa. It was discovered that bottlebrush elastomers possess very high values of β (10 to 100 times higher than typical linear architectures). This high pre-extension factor created strong strain hardening behavior (rapid increase in modulus with respect to deformation) while maintaining extensibility and low modulus. The strain hardening behavior was found to scale inversely with respect to modulus as the side chain molecular weight was altered. This correlation allowed for a simultaneous decrease in initial

modulus combined with faster onset of strain hardening which is unseen in single component linear polymer systems.

Transitioning from chemically to physically crosslinked elastomer allows us to create supersoft materials which can be molded into complex shapes and recycled for numerous uses. To facilitate such materials we have generated ABA type triblock copolymers with bottlebrush middle blocks and crystallizable linear A blocks. We have shown the potential for these systems to spontaneously microphase separate into well-defined, super-soft polymer networks which can be easily melted and reformed. The cross-link density was effectively controlled by the DP of the side chains with respect to the DP of the linear tails. Shorter side chains allowed for crystallization of the linear tails of neighboring bottlebrushes forming a soft network without forming a continuous crystalline phase. However, steric repulsion between longer side chains hindered phase separation and crystallization, thus preventing network formation altogether. Initial stress-strain analysis of these networks display even higher values of β (2 to 4 times higher despite possessing longer network strand lengths than those employed by our chemically crosslinked networks). The steric repulsion between the micro phase-separated domains created high pre-extension of the bottlebrush backbones leading to a combination of supersoft modulus with strong strain hardening. Such properties are rarely seen outside of biological tissues and points to ABA type polymers as a forerunner in future research on the topic of mimicking tissue mechanical response.

Our previous work has dealt mostly with highly grafted brush-like materials (dense bottlebrushes). Recently we have developed a reliable method to synthesize materials with well controlled n_g (number of backbone monomers per side chain). These materials displayed a series of mechanical property correlations as functions of the changing molecular parameter triplet

(n_x, n_{sc}, n_g). These trends include: (1) Inverse relations between modulus and extensibility (typical in polymer materials), (2) concurrent increase of modulus and extensibility (unseen in linear systems), (3) and (4) holding one property constant while altering the other (previously impossible without altering chemical makeup). The comb-like materials (high n_g) allow for vast increases in the extensibility of branched networks, beyond the practical limitation set by linear polymer entanglements ($\sim$5 time extension). Control of the completed architectural triplet effectively expanded the possible combinations of mechanical properties from a strain line (trend 1) to a rich 2D space of possibilities (trends 1-4 combined). The implications of these new trends are discussed at the end of the dissertation, as well as how fine control of all three brush-like parameters (n_x, n_{sc}, n_g) represents the future of studies in this field.

To my friends and family who have supported me.

ACKNOWLEDGEMENTS

I would like to acknowledge the many people who helped me during my studies. Foremost, I want to acknowledge my PI, Dr. Sheiko, for valuing education and taking the time to instruct me in both scientific methodology and in practical attitudes and behaviors important to scientific research. Your consistent correction was key in all of my work. I want to thank Mohammad Vatankhah-Varnosfaderani for his hard work and wonderful ideas that provided many of the samples I was privileged to work with. Your conversations have always been enlightening and your gift for new ideas has been a driving force for progress in the lab. I want to thank the rest of the Sheiko lab for providing advice and an inviting atmosphere during my tenure. I want to thank the Colby lab for helping me in my understanding rheology. Thank you Dr. Rubinstein, and Dr. Dobrynin for your theoretical knowledge and mathematical expertise. I want to thank all the hard work put in by my collaborators. I would particularly like to thank Dr. Matyjaszewski and Asia Burzynska for their foundational synthetic work and knowledge that drove the bottlebrush projects forward. I also want to thank Guojun Xie for his hard work continuing the more fundamental aspects of the brush-like research. I want to thank my friends and family for their constant support especially my parents and my friends from around the department for providing the timely distractions from work that I needed.

TABLE OF CONTENTS

LIST OF TABLES

LIST OF FIGURES

LIST OF ABBREVIATIONS AND SYMBOLS

$\langle R^2 \rangle$	Mean square end-to-end
a	Root mean square end-to-end distance of an entanglement
A_0	Area per BA monomer on a Langmuir trough
A_{br}	Area occupied a bottlebrush macromolecule in AFM micrographs
AFM	Atomic force microscopy
ATRP	Atom transfer radical polymerization
b	Kuhn length of chemical monomer
BA	Butyl acrylate
b_k	General Kuhn length
$CDCl_3$	Chloroform
D	Chemical monomer diameter
Đ	Dispersity
DA	Docosyl acrylate
DB	Dense bottlebrush
DC	Dense comb
DP	Degree of polymerization
DSC	Differential scanning calorimetry
E	Young's modulus
EMI	Electro mechanical instability
G	Shear modulus
G^*	Complex modulus

G’	Storage modulus
G”	Loss modulus
G_0	Apparent modulus
G_e	Shear entanglement modulus
$G_{e,lin}$	Shear entanglement modulus of a linear polymer
GPC	Gel permeation chromatography
HEMA-TMS	Trimetylsiloxy)ethyl methacrylate
I_{eff}	Initiation efficiency
K-N	Kavassalis-Noolandi
L	Contour length of a bottlebrush in an AFM micrograph
l_0	Chemical monomer length
LB	Loose bottlebrush
LB-AFM	Langmuir Blodgett deposition-Atomic force microscopy
LC	Loose comb
L_e	Length of an entanglement
L_n	Number average L
l_p	Persistence length
L_w	Weight average L
m	mass
m_0	Molecular weight of a monomer
M_e	Entanglement molecular weight
$M_{e,lin}$	Entanglement molecular weight of a linear polymer
M_L	Linear density

MMA	Methyl methacrylate
M_n	Number average molecular weight
M_w	Weight average molecular weight
n	General degree of polymerization
N	Number of moles of gas
N_{av}	Avogadro's number
n_{bb}	Degree of polymerization of the backbone
n_e	Degree of polymerization of an entanglement
$n_{e,bb}$	Backbone degree of polymerization of an entanglement
n_g	Number of sidechains per backbone monomer
n_g^*	Crossover n_g from combs to bottlebrushes
n_g^{**}	Crossover n_g from loose bottlebrushes to dense bottlebrushes
n_m	Moles of gas per unit volume
NMR	Nuclear magnetic resonance
n_s	Brush-like stand degree of polymerization
n_{sc}	Degree of polymerization of a side chain
n_x	Network strand degree of polymerization
ODA	Octadecyl acrylate
P	Pressure
PAM	polyacrylamide
PDMS	poly(dimethylsiloxane)
P_e	Number of chain segments in an entanglement volume
PLA	poly(lactic acid)

P*n*BA	poly(*n*-butyl acrylate)
P_{sc}	Number of chain segments in a side chain volume
R	Root mean square end-to-end distance
R_0	Root mean square end-to-end distance of an ideal flexible chain
R_g	Root mean square end-to-end distance of a chain segment between to side chains
R_{max}	Contour length of a polymer chain
R_{sc}	Root mean square end-to-end distance of a side chain
r_T	Transfer ration
T	Absolute temperature
THF	Tetrahydrofuran
T_r	Reference absolute temperature
v	Mole density
V	Volume
v_0	Volume of chemical monomer
V_e	Physical volume of an entanglement
VGP	van Gurp Palmen method
$V_{p,e}$	Pervaded volume of an entanglement
W	Bottlebrush width
WLF	Williams–Landel–Ferry
Z	Number of molecules per unit are in an AFM micrograph
α_t	Frequency shift factor
β	Network pre extension factor

ΔH	Heat of transition from DSC
λ	Extension ratio
ρ	Mass density
σ_{true}	True stress
τ_e	Entanglement time
$\varphi_{(w,A)}$	Mass fraction A bocks

CHAPTER 1: ENTANGLEMENT AND THE BOTTLEBRUSH ARCHITECTURE.[1]

1.1 The need for soft materials

Elastomers are essential soft engineering materials which exhibit relatively low modulus (10^5-10^7 Pa) and high extensibility up to 1000%.[1] Much of the early focus in elastomer research was based around enhancing mechanical properties i.e. making them stiffer and tougher.[2-11] Less attention has been paid to reducing elastomer modulus. However, much softer (10-10^4 Pa) materials are needed for a number of vital applications. Reconstructive surgery implants require moduli tuned to match the surrounding tissues (as low as 10 Pa) to avoid two universal issues: mechanical irritation and the immune response's use of mechanical sensing to identify foreign surfaces.[12-15] Immature cells differentiate into functional versions based on mechanical cues from the environment. Because of this synthetic materials scaffolds for tissue growth and cell differentiation require a wide variety of attainable moduli in order to design functional biological samples.[16 - 22] Much like the immune and cell differentiation responses many dangerous microorganisms alter their behavior based on mechanical cues. Specifically on hard surfaces such organisms will switch from vulnerable isolated mobile behaviors to swarming behaviors (a key event in surface fouling and drug resistance in bacterial infection). This makes control of soft mechanical properties key to next generation and antibacterial and antifouling surfaces.[23-26] Other

[1] Much of this chapter previously appeared in *Nature Materials*, The original citation follows Daniel, W. F. M.; Bodynska, J.; Vatankhan-Varnoosfaderani, M.; Matyjaszewski, K.; Paturej, J.; Rubinstein, M.; Dobrynin, A., V.; Sheiko, S. S. Ultrasoft, Superelastic Solvent-free Elastomers. *Nat. Mater.* **2016**, *15*, 183-189.

important potential applications are found in robotics, membranes, energy storage, and biomedicine.[27-52]

In traditional elastomeric materials the lower limit of stiffness *ca*.10^5 Pa is dictated by chain entanglements that are inherent to polymer melts and, therefore, largely independent of the chemical degree of crosslinking.[53-56] In order to achieve moduli lower than 10^5 Pa a liquid fraction is normally added creating a polymer gel. However, along with many positive features,[57-60] the gelation strategy brings about serious limitations due to polymeric gel fragility[61] and inherently heterogeneous structures.[62] Swollen gels may also suffer from environmental instability in the form of phase separations, solvent evaporation, and loss of solvent during deformation.[63] Last but not least, the addition of solvent decreases acoustic contrast of materials (particularly, hydrogels), which adversely effects ultrasound imaging of polymeric implants in a human body composed of *ca*. 60% water.[64-67] Because of the limitations native to gel materials a new class of material needed to be developed which combined the softness of gels with the stability and robustness of elastomers. The first step in the process is to understand the most fundamental mechanical limitation of soft and dry elastomers, the entanglement.

1.2 Linear polymer entanglement

Consider an entanglement as the simple inability for a polymer chain move through its nearest neighboring chains. When a typical liquid is deformed the deformation stress (force per cross-sectional area) is immediately relaxed by bulk flow of the sample, but relaxation in polymer liquids is blocked by interacting polymer chains which are unable to move through each other during their thermal motion. This leads to a period of time where the deformation stress is stored in system just like a permanently crosslinked network. The modulus of a polymer melt can be

expressed in simple and familiar terms. Just as ideal gas pressure ($P \cong n_m RT$) is governed by the number of moles of gas per unit volume ($n_m = N/V$), the modulus of a polymer melt ($G_e \cong \nu RT$) is governed by mole density of mechanically active strands $\nu = \rho/M_e$, where ρ – mass density, R – universal gas constant, T – absolute temperature, and M_e – molar mass of an entanglement strand. When crosslinked the elastomer traps the entanglements which then behave as additional topological crosslinks.[68,69] Trapped entanglements impose a preordained lower limit for the elastic modulus, $G > G_e \cong \rho RT/M_e$, where G – modulus of the crosslinked network. Melts of typical linear polymers possess $M_e \cong 10^3 - 10^4\ g/mol$, creating an intrinsic entanglement modulus $G_e \cong 10^5 - 10^6\ Pa$.[54,55] This leads to the question of how to control M_e.

In order to understand how to control M_e a more detailed look at entanglement is required. Consider a polymer chain with degree of polymerization (DP) n and average distance between its chain ends (end-to-end distance) of $R \approx \sqrt{l_0 bn}$ where l_0 is the length of the chemical monomer unit and b is the Kuhn segment length which represents the stiffness of the chain. This chain exists in a tube of nearby neighbors whose interactions prevent the chain from moving freely due to contact between the chains. For simplicity sake we assume that it requires a constant number of nearest neighbor contacts P_e to effectively block thermal motion and form an entanglement. This means our main chain can be chopped into individual entanglement segments each encompassing one interaction between the main and neighboring chains. These entanglement segments have monomers n_e and an average end-to-end distance or entanglement diameter of $a \approx \sqrt{l_0 bn_e}$. The entanglement occupies a physical volume described as $V_e = M_e/\rho N_{av} = v_0 n_e$ where M_e is the molar mass of the entanglement strand, ρ is the mass density, N_{av} is Avogadro's number and v_o is the physical volume of a chemical monomer. Additionally the polymer chain carves out a quasi-spherical volume in space called a pervaded volume related to the entailment diameter as $V_{p,e} \approx$

$a^3 \approx (l_0 b n_e)^{3/2}$. The ratio of these two volumes gives the number of chains which exist in the pervaded volume of a single chains $P_e \approx (l_0 b n_e)^{3/2}/v_0 n_e$. We can then calculate DP of an entanglement as Equation 1.1.

$$n_e = {P_e}^2 \frac{{v_0}^2}{b^3 {l_o}^3} \tag{1.1}$$

Based on the work from Kavassalis and Noolandi which theorized P_e to be fairly constant between differing chemistries, numerous empirical measurements have found $P_e \approx 20$ for a great many polymers.[70] Taking Equation 1.1 we can simplify the expression and solve for M_e

$$M_e \cong m_0 {P_e}^2 \frac{{v_0}^2}{b^3 {l_o}^3} \cong {P_e}^2 \rho N_{av} \frac{{v_0}^3}{b^3 {l_o}^3} \sim \frac{D^6}{b^3} \tag{1.2}$$

where $m_0 = \rho N_{av} v_o$ is the molar mass of the chemical monomer, and $D \approx \sqrt{v_0 / l_o}$ is the approximant diameter of the monomer. As can be seen Equation 1.2 reduces the entire understanding of M_e and therefore G_e down some chemical constants and the interplay between the stiffness of a polymer chain (b) and its thickness (D). For traditional materials this interplay is well defined by the chemistry of the polymer chains and results in the traditional limit for polymer melt modulus. In order to create soft materials with moduli below the 10^5 Pa a new method for increasing the relative thickness of a polymer chain without significantly increasing its stiffness needs to be developed.

1.3 The bottlebrush architecture

One thought experiment on the controll of chain thickness and stiffness is presented in Figure 1.1a, where affine expansion transitions the system from a melt of polymer chains to a melt

of mesoscopic cylindrical filaments. This simple procedure creates two beneficial outcomes: Increasing (i) length (L_e) and (ii) diameter (D) of the entanglement strand, leading to an increase of $M_e \sim L_e D^2$ and, hence, decrease of the entanglement plateau modulus as $G_e \sim 1/M_e$. However, this naïve approach does not take into account the fact that conventional solid filaments stiffen as the diameter increases leading to higher entanglement densities (Figure 1.1b). The persistent length of solid filaments is shown, both theoretically[71] and experimentally,[72] to raise dramatically with their diameter as $l_p \sim D^4$ (Figure 1.1d) note that $l_p \sim b_k$ were b_k is a general term for the Kuhn length (b) for all archetectures considered in this dissertation. Furthermore, rod-like species ($D \ll l_p$) may undergo nematic transitions during solvent removal, which not only lead to a modulus increase but also introduce anisotropy to mechanical properties. These combined effects make rigid, solid-like filaments unsuitable for the creation of supersoft elastomers.

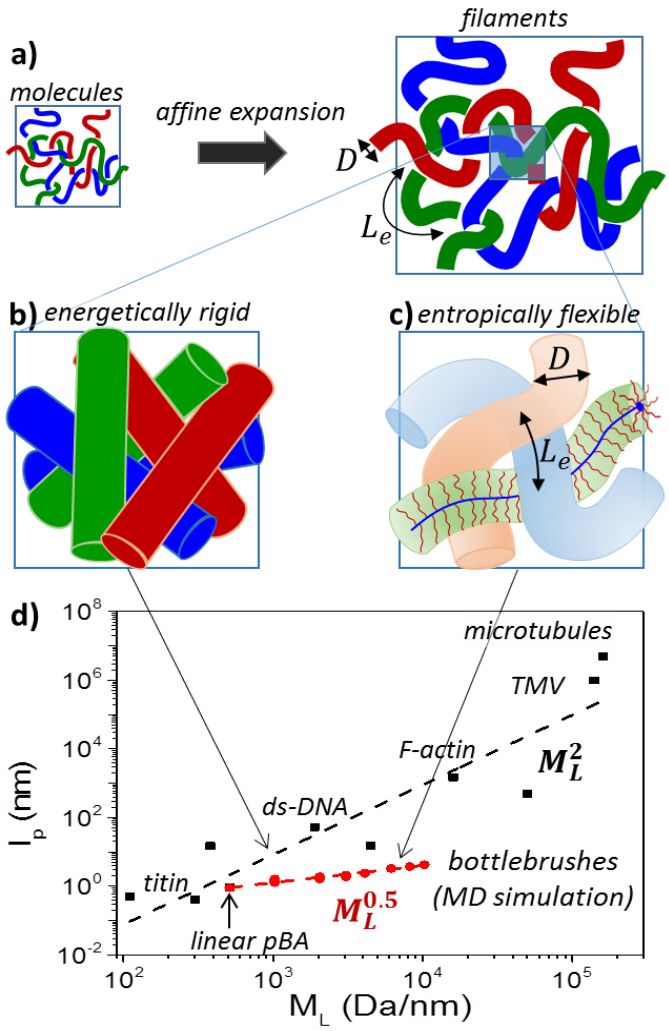

Figure 1.1: Transitioning from polymer molecules to mesoscopic filaments. **a)** A thought experiment: Affine expansion of a melt of linear chains results in reduction of entanglement density (increase of L_e - length of entanglement strand) and an increase of molecule's diameter (D). **b)** The diameter increase causes significant enhancement of rigidity in solid-like filaments, which generally promotes overlapping with neighbors, increasing the entanglement density. **c)** A melt of liquid-like flexible filaments displays lower entanglement density than a melt of conventional linear polymers. One of the cylinders (green) displays its interior brush-like structure explored in this study. **d)** In dilute solution, solid-like filaments display a strong increase of the persistence length with the linear density $M_L = m/L \sim D^2$ as $l_p \sim M_L^2 \sim D^4$, where m and L and mass and contour length of a filament, respectively, while solvent removal causes additional stiffening and ordering of solid filaments.[72] In contrast, bottlebrushes remain liquid and their persistence length in a melt state exhibits a much weaker increase with diameter as $l_p \sim M_L^{1/2} \sim n_{sc}^{1/2} \sim D$, where n_{sc} is degree of polymerization of bottlebrush side chains. [73,74]

This unfavorable realization does not dismiss the idea of the affine expansion (Figure 1.1a); instead it presents us with a challenge to create mesoscopic liquid-like filaments that neither coalesce nor interpenetrate but also remain flexible with increasing diameter (Figure 1.1c). Such filaments can be prepared by dense tethering of long side chains with DP (n_{sc}) and number of side chains per unit backbone monomer (n_g) to a polymer backbone with DP (n_{bb}), which results in comb-like[75-78] and bottlebrush [79-81] architectures (Figure 1.1c). Molecular dynamics simulations of melts of bottlebrush polymers gives evidence that their persistence length behaves as $l_p \sim D$ (Figure 1.1d),[73,74] fulfilling the requirement for filaments that remain flexible with growing diameter. This flexibility is entropic in origin and afforded by the ability of a liquid-like filament to freely reposition its mass (side chain monomers) around its central axis. The unique combination of high flexibility and decreased entanglement density of bottlebrushes opens the path for the creation of a new class of single-component materials with low modulus and high deformability. A scaling relationship between the mass (M_e) and dimensions of the entanglement strand is provided by the Kavassalis-Noolandi (K-N) conjecture as $M_e \approx D^6/l_p^3 \sim D^6/{b_k}^3$ (assuming $l_p < L_e$). This relation reproduces Equation 1.2. Simulation data suggests that the diameter of bottlebrushes is related to the end-to-end distance of the side chain ($R_0 = \sqrt{n_{sc} b l_o}$) which directly suggests that the entanglement modulus of bottlebrush melts is expected to decrease with the degree of polymerization of side chains (n_{sc}) as $G_e \sim M_e^{-1} \sim {b_k}^3/D^6 \sim D^{-3} \sim n_{sc}^{-3/2}$ (taking into account $b_k \sim D$).

1.4 Bottlebrush scaling predictions

Herein is presented a summarized version of the theoretical predictions concerning the entanglement modulus of brush-like polymer melts as a function of n_g and n_{sc}. For a full treatment please see Daniel, W. F. M., et al. *Nat. Mater.* **2016**, *15*, 183-189.

The Molecular conformation and assembly of bottlebrush and comb-like polymers in melts depend on the DP of side chains (n_{sc}) and DP of the backbone spacer per sidechain (n_g) (Fig. 1.2), as well as on the monomeric volume v, the monomeric length l, and the stiffness of polymer chains characterized by the Kuhn length b. Depending on the side-chain length and grafting density, we distinguish four conformational regimes with distinct rheological behaviors (Fig. 1.2), however only the highest grafting density regime is considered in this chapter's experimental results.

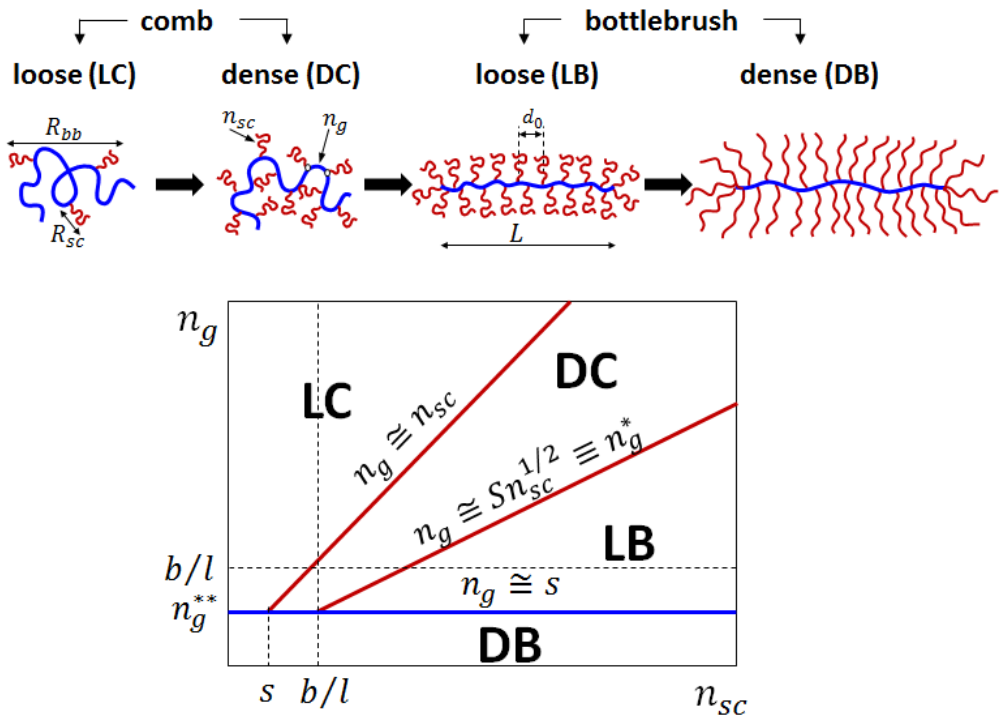

Figure 1.2: Diagrams of states of brush-like polymers. The diagram is presented in terms of degree of polymerization of side chains n_{sc} and backbone spacer between neighboring side chains n_g (logarithmic scales). Comb regimes with almost unperturbed Gaussian backbone and side chains: LC – loosely-grafted combs with strongly interpenetrating neighboring combs, DC – dense combs with weak interpenetration. Bottlebrush regimes: LB – loosely-grafted bottlebrushes with almost unperturbed Gaussian side chains and partially stretched backbone on length scale of side chains, DB – dense bottlebrushes with extended side chains and stretched backbone on length scale of side chains. Dashed lines at b/l correspond to boundaries of stiff side chains (vertical) for $n_{sc} < b/l$, and stiff spacer (horizontal) for $n_g < b/l$. Backbone is almost fully stretched up to length scale of side chain size below the blue horizontal line $n_g \cong n_g^{**} \cong s$.

Loosely-grafted and densely-grafted comb regime (LC and DC). At very low grafting densities $n_g \gg n_{sc}$ the sidechains of so called loose-comb molecules have no interactions with each other because the average distance between grafting points along the backbone ($R_g \cong \sqrt{n_g l_0 b}$) is greater than the side chains own size ($R_{sc} \cong \sqrt{n_{sc} l_0 b}$). This lack of strong interactions between sidechains means that the loosely grafted comb possesses nearly unperturbed random

polymer chain statistics with end-to-end distances $R = \sqrt{n_{bb} l_0 b_{k,LC}}$ where $b_{k,LC} = b$ of the specific chemistry used. At the limit of $n_g \gg n_{sc}$ the contribution of sidechains the total chain volume is negligible and the effective monomer volume is still $v_0 \approx D^2 l_0$. Solving Equation 1.2 reveals

$$M_{e,LC} \approx M_{e,lin} \tag{1.3}$$

$$G_{e,LC} \cong \frac{\rho RT}{M_e} \cong G_{e,lin} \tag{1.4}$$

Where $M_{e,lin}$ and $G_{e,lin}$ are the entanglement mass and entanglement modulus of the linear polymer chemistry. This results in the flat red domain seen in Figure 1.3a,b. However, as n_g decreases the distance between sidechains $R_g \leq R_{sc}$ and the sidechains begin to intrude into each other pervaded volumes. This means the average number of other chains segments within a chains pervaded volume ($P_{sc} \cong R_{sc}^3/(n_{sc} v_0) \cong n_{sc}^{1/2} (b l_0)^{3/2}/v_0$) is partially occupied buy side chains from the same polymer backbone. Since P_{sc} like P_e is a constant there are only two options: (1) the chains begin to stretch out thus increasing either R_{sc} of R_g to make more room, or (2) neighboring polymer combs must separate in space leading to fewer interactions between side chains from different combs and an increased effective polymer diameter. Since the stretching of chains carries a heavy entropic penalty[55] the combs begin to separate in space diluting their backbones just as if we had added solvent to the system. Because of this the comb maintain their unperturbed chain conformation statistics and $b_{k,DC} = b$ leading to the expression.

$$M_{e,DC} \sim \frac{{D_{DC}}^6}{{b_{k,DC}}^3} \sim \frac{{v_0}^3}{{l_o}^3 b^3} \left(\frac{n_{sc}}{n_g} + 1 \right)^3 \tag{1.5}$$

$$G_{e,DC} \cong \frac{\rho RT}{M_e} \sim \left(\frac{n_{sc}}{n_g} + 1\right)^{-3} \quad 1.6$$

where $\left(n_{sc}/n_g + 1\right)^3$ is the effective contribution of the sidechains towards the molecular diameter. This trend results is a sharp change in modulus seen as the red line with slope proportional to $\left(n_{sc}/n_g\right)^3$ in Figure 1.3a,b.

As the density of sidechains along the backbone grows, the pervaded volume as a single side chain becomes increasingly filled with sidechains belonging to the same backbone. This process continues until there is no longer space for neighboring side chains. A section of a backbone passing through the volume R_{sc}^3 contains on average n_{sc} monomers because its conformations are similar to the conformations of side chains. Therefore, n_{sc}/n_g side chains belonging to the same comb molecule and connected to each other through the backbone section containing n_{sc} monomers reside within the volume R_{sc}^3. The number of such groups (branched sections) belonging to different comb molecules overlapping with each other within the volume R_{sc}^3 is

$$Z = \frac{P_{sc} n_g}{n_{sc}} \cong \frac{(bl_0)^{3/2}}{v_o} \frac{n_g}{n_{sc}^{1/2}} \cong \frac{n_g}{n_g^*} \geq 1 \qquad for \quad n_g^* < n_g < n_{sc} \quad (1.7)$$

This allows us to define a transition condition where the combs with ideal chain conformation can entirely occupy the volume R_{sc}^3 with chains from the same comb ($n_g^* = n_{sc}^{1/2} v_o/(bl_0)^{3/2}$). At this point the combs are completely separated in space with an average diameter determined by the ideal R_{sc}. In order to increase the density of side chains beyond this point the conformations of the chain segments must be stretched beyond ideal conformations.

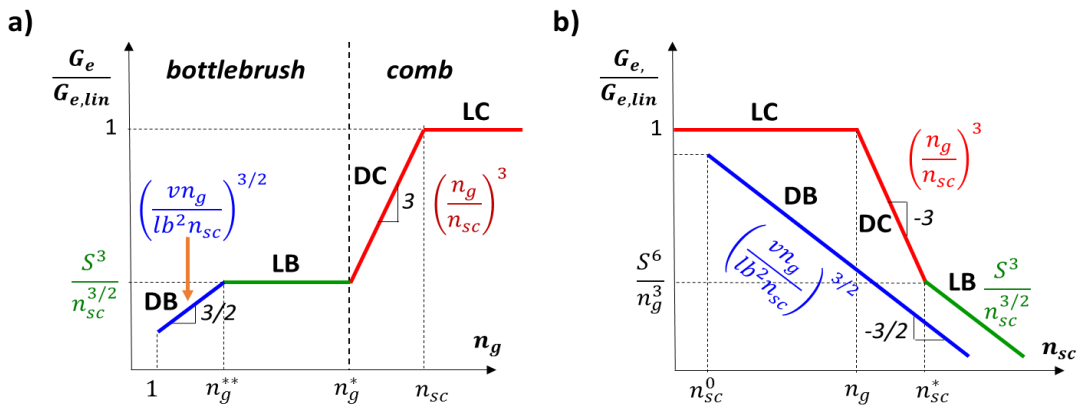

Figure 1.3: Different entanglement modulus regimes of comb-like polymers. (Equations 1.4 1.6, 1.9, 1.11) Presented as a function of **a)** degree of polymerization (DP) of the spacer between neighboring side chains (n_g at constant n_{sc}) and **b)** side chain DP (n_{sc} at constant n_g).

Loosely-grafted bottlebrush regime (LB). In the LB regime further reduction of n_g demands deviation from ideal chain statistics. The entropic penalty for stretching all of the sidechains is considerably larger than the penalty of stretching the backbone. In this regime further addition of side chains results in two counteracting phenomenon. First, adding side chains increases the mass of the polymer strands. Second, it stretches the backbone resulting in larger effective b_k and there for shorter distances between entanglements as shown in Equation 1.1 and 1.2. Because of this the entanglement mass and modulus remain approximately constant while the backbone stretches out leading to the flat green line shown in Figure 1.3a. On the other hand as the sidechain size increases the crossover condition ($n_g^* \sim n_{sc}^{1/2}$) pushes the loose bottlebrush further in the regime. The backbone is stretches increasing the chain stiffness as $b_{k,LB} \sim {n_{sc}}^{1/2}$ while the chains diameter continues to grow with the ideal sidechains size $R_{sc} \sim {n_{sc}}^{1/2}$. This dual effect results in the expressions

$$M_{e,LB} \sim \frac{{D_{LB}}^6}{{b_{k,LB}}^3} \sim {n_{sc}}^{3/2} \qquad 1.8$$

$$G_{e,LB} \cong \frac{\rho RT}{M_e} \sim {n_{sc}}^{-3/2} \quad 1.9$$

It should be noted that realistically the LB regime is short. For $n_{sc} = 100$ the regime takes place for only one order of magnitude in n_g and is much shorter for more typical brushes.

Densely-grafted Bottlebrush Regime (DB). The boundary between the LB and DB regimes ($n_g < n_g^{**} = v_o/bl_0^2$) corresponds to the fully extended backbone state. At this point the conformation of the backbone cannot stretch any further without encountering enormous energetic penalties.[55] At this point the sidechains begin to weakly stretch leading to an increase in both diameter and rigidity of the polymer strand. This regime is short in terms of n_g (assuming $n_g = 1$ is the practical minimum) but can extend in terms of n_{sc} until the sides chains approach the entanglement length of the linear chain chemistry. There is a simultaneous growth of $b_{k,DB}$ and D_{DB} as $\sim(n_{sc}/n_g)^{1/2}$ leading to the equations 1.10 and 1.11 which can be seen in as the blue lines in Figure 1.3a,b.

$$M_e \sim \frac{{D_{DB}}^6}{{b_{k,DB}}^3} \sim \left(\frac{n_{sc}}{n_g}\right)^{3/2} \quad 1.10$$

$$G_{e,DB} \cong \frac{\rho RT}{M_e} \sim \left(\frac{n_{sc}}{n_g}\right)^{-3/2} \quad 1.11$$

Although the DB regime has weaker scaling than the DC regime, dense bottlebrushes still represent the lowest practical limit for entanglement modulus in brush-like architectures. The remainder of this chapter is dedicated to proving the scaling found in Equation 1.11.

1.5 Synthesis of materials

Highly grafted brush-like architectures represent the simplest architecture to produce with reliable homogeneity. They also represent the lowest modulus architectures considered in this dissertation. Because of this, bottlebrushes were chosen as the first architecture for fundamental study. The P*n*BA samples were produced by sequential ATRP steps in which long polymer backbone macroinitiators were synthesized from HEMA-TMS followed by replacing the TMS functionalities with reactive bromine sites and sequential ATRP "polymerize-from" growth of side chains. PDMS samples were produced by ATRP "polymerize-through" of mono-functional macromonomers and difunctional crosslinkers inside an evacuated cylindrical mold. For full synthetic details please see Daniel, W. F. M., et al. *Nat. Mater.* **2016**, *15*, 183-189.

1.6 Molecular characterization

NMR and GPC analysis were used to obtain approximant molecular weights and molecular characteristics.

Monomer conversion and GPC. The conversion of BA was determined from ^{1}H NMR spectra recorded in $CDCl_3$ as a solvent using Brüker 300 MHz spectrometer. Molecular weight distributions of the polymers were characterized by gel permeation chromatography (GPC) using Polymer Standards Services (PSS) columns (guard, 10^5, 10^3, and 10^2 Å), with THF eluent at 35 °C, flow rate 1.00 mL/min, and differential refractive index detector (Waters, 2410). The apparent number-average molecular weights (M_n) and molecular weight dispersities (M_w/M_n) were determined with a calibration based on linear poly(methyl methacrylate) (PMMA) standards and diphenyl ether as an internal standard, using WinGPC 6.0 software from PSS (Figure 1.4). Bottlebrush samples were analyzed by GPC with light scattering detection to measure molecular weight distribution of cleaved side chains (Figure 1.4). The initiation efficiency of the grafting-from reaction was determined as a ratio of the DP values obtained from monomer conversion (NMR) and side-chain cleavage. The average grafting efficiency is about 0.65 (65%) which is close to the grafting density obtained by the LB-AFM techniques. The backbone DP by GPC of the macroinitiator as $n_{bb} = M_{MI}/M_0 = 2{,}035 \pm 100$. The NMR GPC analysis is summarized in table 1.1. However both techniques are less reliable for analysis of branched molecules so additional analysis was conducted using the LB-AFM technique.

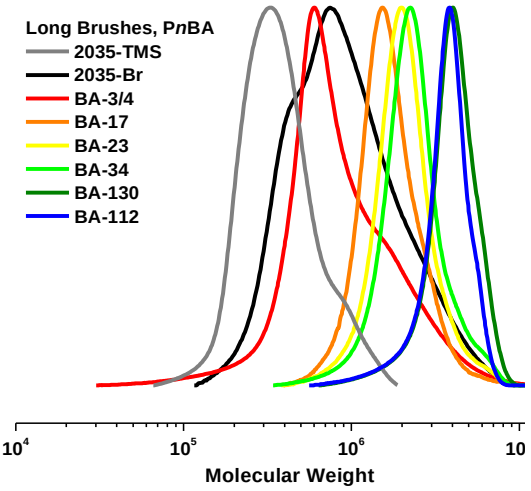

Figure 1.4: GPC traces. Linear (gray) **MI-TMS** and (black) **MI-Br**, and bottlebrushes (red) **BA-3/4**, (orange) **BA-17**, (yellow), **BA-23**, (pale green), **BA-34**, (dark green), **BA-130**, and (blue) **BA-112**.

Table 1.1 Initial characterization of materials

Name	Composition	$n_{sc,NMR}$ [1]	$M_{n,GPC}$ [2]	M_w/M_n [2]	$M_{n,SC}$ [3]	$M_w/M_{n,sc}$ [3]	n_{sc} [4]	I_{eff} [5]
MI-TMS	P(HEMA-TMS)$_{2035}$	-	326,000	1.29	-	-	-	-
MI-Br	PBiBEM$_{2035}$	-	694,000	1.76	-	-	-	-
BA-6	PBiBEM$_{2035}$-*g*-P*n*BA$_{3/4}$	3-4	640,000	1.76	-	-	-	-
BA-17	PBiBEM$_{2035}$-*g*-P*n*BA$_{10}$	10	1,540,000	1.19	2,180	1.12	17	59
BA-23	PBiBEM$_{2035}$-*g*-P*n*BA$_{16}$	16	1,870,000	1.19	3,000	1.18	23	70
BA-34	PBiBEM$_{2035}$-*g*-P*n*BA$_{24}$	24	2,070,000	1.20	4,300	1.30	34	70
BA-130	PBiBEM$_{2035}$-*g*-P*n*BA$_{48}$	48	3,380,000	1.13	16,600	1.10	130	40

[1] Degree of polymerization of side-chains determined from the monomer conversion by ^{1}H NMR, $n_{sc,NMR} = n_{targeted} \cdot M_{conversion}$. [2] Determined by THF GPC using PMMA standards. The GPC data are inaccurate due to the large size and branched nature of the macromolecules. [3] Number average molecular weight and PDI of cleaved side chains determined by THF GPC using PSt standards. [4] Degree of the polymerization of side chains determined from the equation: $n_{sc} = M_{n,sc} / M_{BA}$, where M_{BA}=128 – molecular weight of *n*-butyl acrylate [5] Initiation efficiency determined as $I_{eff} = (n_{sc,NMR} / n_{SC}) \cdot 100\%$.

LB-AFM. The large spatial dimensions of bottlebrush molecules enable visualization by AFM. Combining this with the Langmuir Blodgett deposition technique was shown in the past to be an accurate analysis technique for bottlebrushes.[82] The samples for atomic force microscopy (AFM) studies were prepared by Langmuir-Blodgett (LB) deposition (Figure 1.5). LB films were transferred onto freshly cleaved mica substrates at a constant surface pressure of 0.5 mN/m and a controlled transfer ratio. Imaging of individual molecules was performed in PeakForce

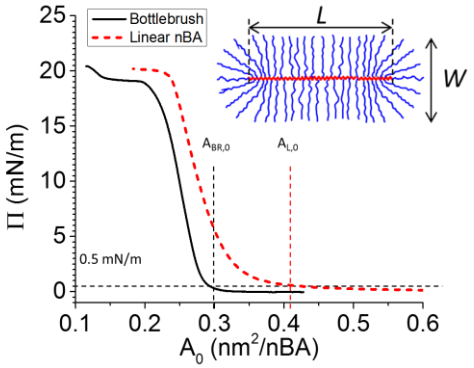

Figure 1.5: LB isotherms of surface pressure versus monomer area of linear and bottlebrush BA samples. The A_{BR} and A_0 values were taken at identical surface pressures (0.5 mN/m) to insure comparison of monolayers at the same level of compression. Schematic displays length *L* and width *W* of an adsorbed bottlebrush.

QNM mode using a multimode AFM (Brüker) with a NanoScope V controller. Silicon probes were used with a resonance frequency of 50-90 Hz and a spring constant of ~0.4 N/m. In-house developed computer software was used to analyze the AFM images. Typically, ensembles of 1000 or more molecules were analyzed to ensure standard deviation of the mean below 10%. The results are summarized in Table 1.2. The number-average contour length (L) were directly extracted from the AFM micrographs of individual macromolecules both in dense and sparse monolayers on a solid substrate (Figure 1.6) as $n_{bb} = L/l = 2{,}040 \pm 60$. All molecular length scales characterized by LB-AFM are disabled in Table 1.2.

From the LB-AFM analysis, we determine the number average mass per unit length of the backbone, which can be directly translated to the side-chain degree of polymerization per monomeric unit of the backbone as

$$\frac{n_{sc}}{n_g} = \frac{r_t A_{br}}{n_{bb} A_0} = \frac{r_t l_0 \left(W + \frac{\pi r_t W^2}{4L}\right)}{A_0} \qquad 1.12$$

Where W- is the number average 2D width measured from AFM micrographs, r_t- the LB transfer ratio, A_{br}- the area occupied a bottlebrush macromolecule in AFM micrographs, and $A_0 = M_0/(mN_{Av})$ is the area per BA monomer on a Langmuir trough as calculated from the known mass of material deposited per unit area of the trough (m) and molar mass of the P*n*BA monomer ($M_0 = 128\ g/mol$). This equation is expounded upon in Chapter 2. The molecular area A_{br} was determined by two methods: (i) counting the number of molecules (Z) in AFM images per unit area, which gives $A_{br} = \mathrm{Z}^{-1}$ and (ii) measuring contour length (L) and brush width (W) that give $A_{br} = LW + \pi W^2/4$ (assuming hemicircular end-caps of adsorbed bottlebrushes, (Fig. 1.6)). GPC measurement of the macroinitiator DP displayed $n_{bb} = M_{MI}/M_{0,MI} = 2035 \pm 100$, in

agreement with $n_{bb} = 2040 \pm 60$ determined by LB-AFM (Table 1.3). The full extension of the bottlebrush backbones is caused by steric repulsion of densely grafted side chains resulting in a backbone tension of the order of 1 nN.[83] The product of linear mass density and bottlebrush contour length gives molecular weight distribution (MWD). Figure 1.7 demonstrates correlation between the MWD data obtained by the GPC and LB-AFM techniques. A slight shift towards higher molecular weights seen in the LB-AFM is due to exclusion of small species analysis software. The number-average contour length were directly extracted from the AFM micrographs of individual macromolecules both in dense and sparse monolayers on a solid substrate (Figure 1.6) as $n_{bb} = L/l = 2{,}040 \pm 60$. The complete molecular characterization is presented in Table 1.3.

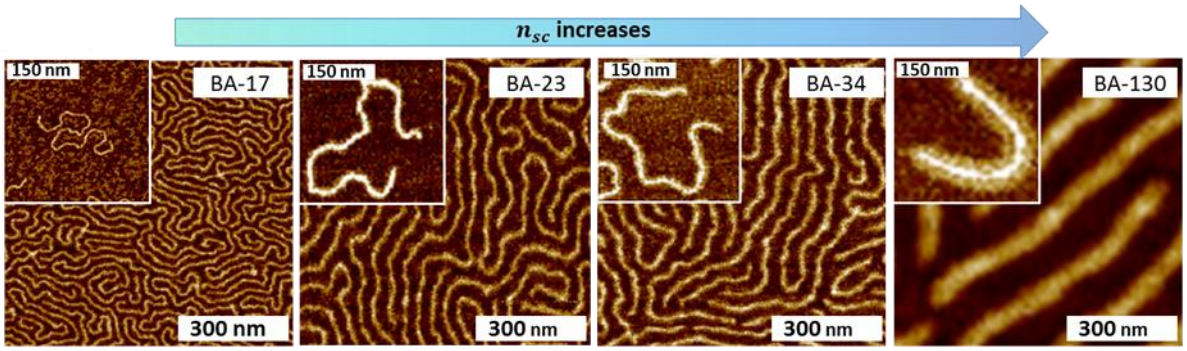

Figure 1.6: AFM of Bottlebrush samples. AFM height images of the P*n*BA bottlebrushes with the same backbone but different side-chain DPs on a mica substrate: Large images - Langmuir-Blodget monolayers. Insets - single molecules prepared by spin-casting. While not equivalent to conformations in bulk melts, the AFM studies qualitatively corroborate the increase in diameter and rigidity of molecular bottlebrushes with increasing n_{sc}.

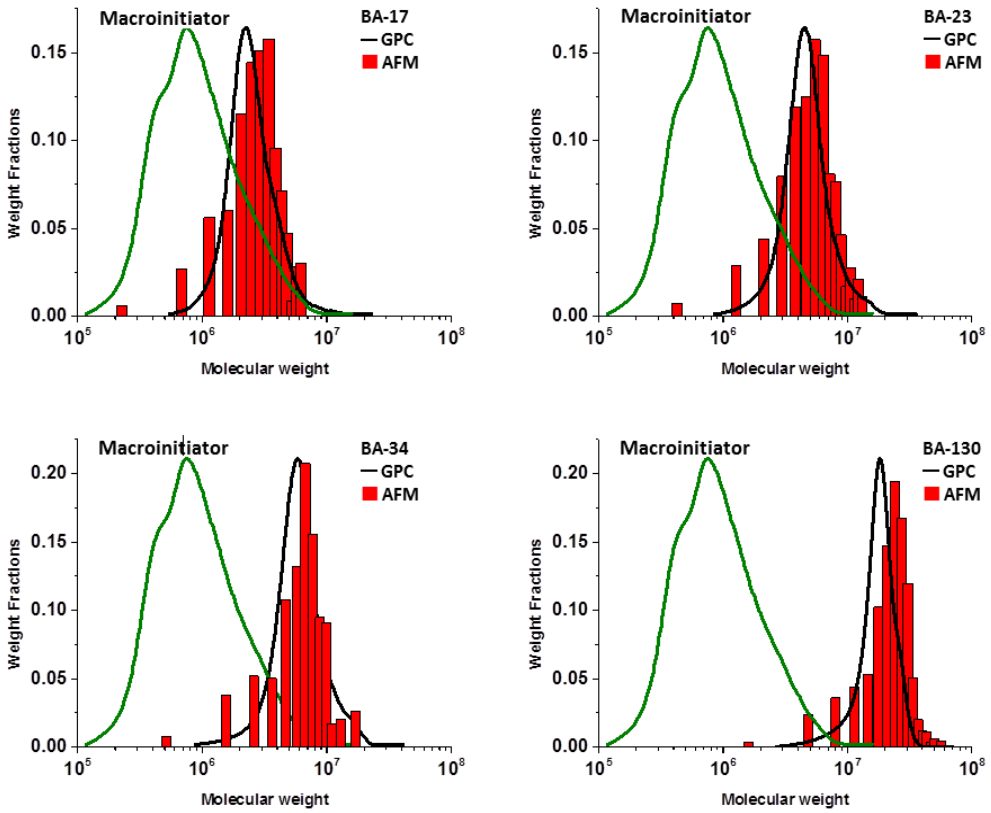

Figure 1.7: Overlay of GPC traces. Bottlebrush samples (red histograms) with LB-AFM molecular weight distribution analysis (black lines). The green lines correspond to molecular weight distribution of the macroinitiators (backbones without side chains).

Table 1.2: LB-AFM analysis of the dimension of P*n*BA bottlebrushes

Sample	r_t [1]	A_{br} (nm^{-2}) [2]	W (nm) [3]	n_{sc}/n_g [4]	L_n (nm) [5]	L_w/L_n [6]	n_{bb} [7]
BA-17	0.88	0.28	11	9	513	1.5	2052
BA-23	0.89	0.29	21	17	515	1.6	2060
BA-34	0.90	0.29	26	21	495	1.6	1980
BA-130	0.98	0.27	69	69	517	1.5	2068

[1]Transfer ratio defined as ratio of change in LB trough area over area of transfer substrate. [2]Area per BA monomer of the Langmuir monolayers on the water surface. [3]Number average width of the P*n*BA bottlebrush samples from AFM. [4]Number average DP of side-chains adjusted for grafting density as measured by LB-AFM (Equation 1.12). [5]Number average contour length of P*n*BA bottlebrush backbone measured using AFM. [6]Dispersity of P*n*BA bottlebrush contour length, PDI=L_w/L_n, where L_w and L_n are weight and number average lengths. [7]Number average DP of the backbone determined from the AFM contour length as $n_{bb}=L/l_0$, where l_0=0.25 nm is the monomer length.

Table 1.3: Final molecular characterization

Sample	M,[1] 10^6 g/mol	n_{sc}[2] (cleavage)	n_{sc}/n_g[3] (LB-AFM)	n_g[4]	$Đ$[5]	G_e, Pa[6]	M_e,[7] 10^6 g/mol	$n_{e,bb}$[8]
MI[9]	0.33[10]	0	0	NA	1.3	NA	NA	NA
BA-6	NA[11]	NA	3	1.75	NA	11432 ± 331	0.2	461±13
BA-17	2.9	17	9	1.96	1.5	2421 ± 75	1.1	784±24
BA-23	4.7	23	14	1.61	1.6	1310 ± 54	2.1	894±37
BA-34	5.8	34	21	1.61	1.6	938 ± 28	2.9	1012±30
BA-130	17.9	130	67	1.89	1.5	178 ± 7	15.2	1728±68

[1]Number average molar mass determined from mass per unit area and molecular area using the LB-AFM method (except MI).[31] [2]Number average DP of side chains determined by GPC of cleaved side chains. [3]Number average DP of side chains multiplied by the grating density n_g^{-1} as measured by LB-AFM (Equation 1.12). [4]Grafting density calculated from LB-AFM n_{sc}/n_g and cleavage n_{sc}. [5]Dispersity of P*n*BA bottlebrush contour length, PDI=L_w/L_n, where L_w and L_n are weight and number average contour lengths of the bottlebrush backbones. [6]Plateau modulus determined as storage modulus at the frequency of the minimum in tan(δ). Modulus error was calculated by taking the standard error of the mean from multiple measurements of the master curve. [7]Molar mass of the entanglement strand calculated as $M_e = \rho RT/G_e$, where $\rho = 1.09\ g/cm^3$ – mass density of P*n*BA. [8]Backbone DP of the entanglement strand calculated as $n_{e,bb} \cong M_e n_{bb}/M$, where M - molar mass of bottlebrush and n_{bb}=2040- average DP of the backbone. [9]Macroinitiator (MI) is a precursor for the backbone. [10]Number average molecular weight measured by RI-GPC using PMMA standards. [11]AFM-based analysis of BA-6 was inaccurate due to closely spaced macromolecules having the shortest side chains.

1.7 Rheology and mechanical analysis

To investigate the effect of n_{sc} on the plateau modulus in the melt of the polymer brushes, the frequency dependence of dynamic moduli was measured in a window of 0.01 to 100 rad/s over a range of temperatures and strains using an ARES-G2 rheometer from TA Instruments. The time-temperature superposition principle was used to construct master curves of modulus versus frequency with a reference temperature of 298 K using the WLF equation. Compression

experiments were done with an RSA-G2 DMA from TA instruments using 25mm compression plates at a constant closure rate of 0.01 mm/s at 25°C. Based on the time-temperature superposition principle, master curves of modulus versus frequency were constructed using TRIOS software from TA instrument. A series of *Williams–Landel–Ferry* (WLF) parameters was generated using eq 1.13 for each sample and used to shift the final master curves to 298 K

$$\log(\alpha_t) = \frac{-C_1(T-T_r)}{C_2+(T-T_r)} \qquad 1.13$$

where α_t -frequency shift factor for a desired reference temperature, $C_1$and C_2-empirical fitting constants derived from manual shifts of data at multiple temperatures, T and T_r - sample temperature and desired reference temperature, respectively.[84] Table 1.4 summarizes the corresponding WLF parameters.

Table 1.4: WLF parameters

sample	C_1	C_2 (K)
BA-6	7.3	129.2
BA-17	3.9	153.9
BA-23	3.5	154.4
BA-34	3.8	161.8
BA-130	3.6	162.5

Three methods were used to analyze the entanglement plateau modulus of the polymer samples. Figure 1.10 shows trends of entanglement moduli versus relative side-chain length. Both methods for assigning entanglement moduli give excellent agreement with theory showing dependence on relative side-chains DP ($G_e \sim (n_{sc}/n_g + 1)^{-3/2}$) as shown in Figure 1.10 below. For the first method the value of the entanglement modulus is taken as the value of G' at the frequency of the minimum in the tangent delta as described in detail by Lomellini[85] (Figure 1.8). Entanglement modulus and tangent delta data is represented in Table S4 and the trend in entanglement modulus versus relative sidechains DP is displayed in black in Figure 1.10.

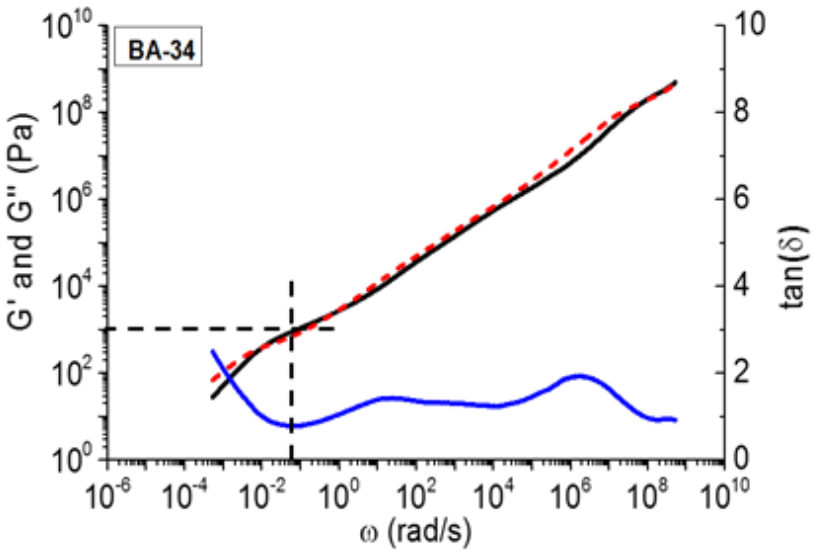

Figure 1.8: Rheological master curve of storage modulus (G'), loss modulus (G'') and the tangent delta (tan(δ)) as a function of angular frequency. The vertical and horizontal dashed line mark the minimum of tangent delta and the entanglement modulus, respectively.

For the second method the van Gurp Palmen method assigns the entanglement modulus as the value of the storage modulus at the minimum in phase angle within the entanglement regime of a VGP plot[86] (Figure 1.9). The moduli versus relative sidechains size are displayed in red in Figure 1.10.

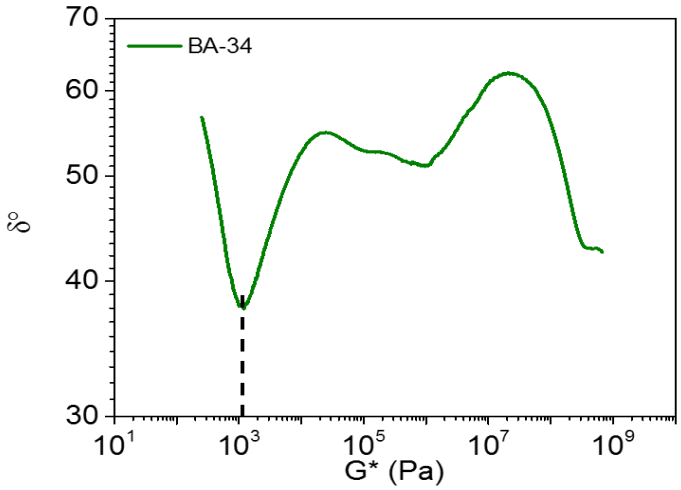

Figure 1.9: Phase angle (δ) vs. complex modulus (G^*). The entanglement modulus is assigned using the van Gurp Palmen method as the value of the G^* at the minimum value of the tan(δ) within the entanglement regime

For the third method, the value of the storage modulus determined by modeling experimental data with a fitting equation described below. To evaluate the rheological data we model the storage modulus $G'(\omega)$ and loss modulus $G''(\omega)$ using the molar mass weight M_e as a fitting parameter. The storage and loss modulus can be presented as the sine and cosine transform of the time dependent modulus G(t)[55,87]:

$$G'(\omega) = \omega \int_0^\infty G(t) \sin(\omega t)\, dt \tag{1.14}$$

$$G''(\omega) = \omega \int_0^\infty G(t) \cos(\omega t)\, dt \tag{1.15}$$

A model for G(t) includes two distinct regions of rheological behavior seen in the bottlebrush sample. These are Region 1: power law relaxation with exponent 0.6 representing transition zone of chain of effective Kuhn monomers, where G_1 and τ_t are the modulus and relaxation time of the effective Kuhn monomer. Note G_1 and τ_t serve to shift the date to allow overlap between the power law and experimental data. As their specific values do not have physical meaning in the application of this theory

$$G(t)_{power} = G_1 \left(\frac{t}{\tau_1}\right)^{-0.6} \tag{1.16}$$

and Region 2: entanglement relaxation. For monodisperse melts, as the entanglement relaxation can be approximated by a single exponential decay

$$G(t)_{Rept} = \frac{\rho RT}{M_e} \exp\left[-\frac{t}{\tau_e \left(\frac{M}{M_e}\right)^{3.4}}\right] \tag{1.17}$$

where ρ, R, and T are the polymer melt density, the gas constant, and the absolute temperature respectively. τ_e and M_e are the entanglement onset time and entanglement molar mass, and M is

the molar mass of the brush species. To account for molar mass polydispersity, we use the double reptation model as the square of the integral of the conventional reptation relaxation multiplied by the weight fraction of each respective species over all molar mass species[88]

$$G(t)_{Reptation} = \frac{\rho RT}{M_e}\left(\int_0^{\infty} w_i e^{-t/\tau_e\left(\frac{m_i}{M_e}\right)^{3.4}}\right)^2 \quad 1.18$$

where w_i and m_i are the weight fraction and molar mass of a species. For discrete molar mass distribution data, the final model was described as

$$G(t) = G_1\left(\frac{t}{\tau_1}\right)^{-0.6} + \frac{\rho RT}{M_e}\left(\sum_{i=1}^{i=k} w_i e^{-t/\tau_e\left(\frac{m_i}{M_e}\right)^{3.4}}\right)^2 \quad 1.19$$

where $G_1/\tau_1^{-0.6}$, M_e, and τ_e are the fitting terms used to fit the model with the experimental data. The entanglement modulus versus the relative side chain DP are displayed in blue in Fig. 1.10. A sample overlay of the fitting and experimental data is shown in Fig. 1.11c.

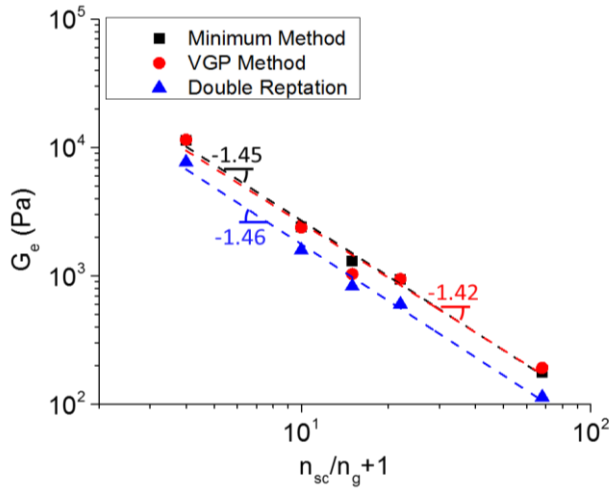

Figure 1.10: Comparison of methods. Comparison of entanglement modulus analysis methods yields excellent agreement with theoretical trend of $G_e \sim (n_{sc}/n_g + 1)^{-3/2}$.

As shown in Figure 1.11c, a double-reptation fit for sample BA-34 provides excellent agreement with the experimental data. Table 1.3 summarize the results of the data analysis, while

Figure 1.11d displays the dependence of the plateau modulus on $n_{sc}/\ n_g + 1$ - reciprocal volume fraction of bottlebrush backbones. To enable comparison with similar structures reported previously by other groups, we plot the modulus ratio of bottlebrush and linear polymers multiplied by a dimensionless parameter $\alpha = (v/b^2 l)^{-3/2}$ accounting for the difference in chemical composition (Equation 1.11). Remarkably, all data points, including that of (i) our P*n*BA bottlebrushes, (ii) pLA bottlebrushes studied by Kornfield et al.,[80] and (iii) dense polyolefin combs studied by Fetters et al.[77] fall on one line with a slope of -1.49±0.05 in agreement with Equation 1.11. The bottlebrush melt ($n_{sc} = 130$) displays modulus on the order of 100 Pa, which is three orders of magnitude lower than the G_e of linear P*n*BA. This low modulus is ascribed to the significant decrease of the entanglement density in bottlebrush melts composed of thick, flexible, and weakly-interpenetrating macromolecules. As shown in Table 1.3, both the molar mass of the entanglement strand ($M_e \cong 10^5 - 10^7\ g/mol$) and the DP of its backbone ($n_{e,bb} \cong 500 - 2{,}000$) are significantly larger than the corresponding values for linear P*n*BA, $M_e \cong 2 \times 10^4\ g/mol$ and $n_e \cong 150$, respectively.

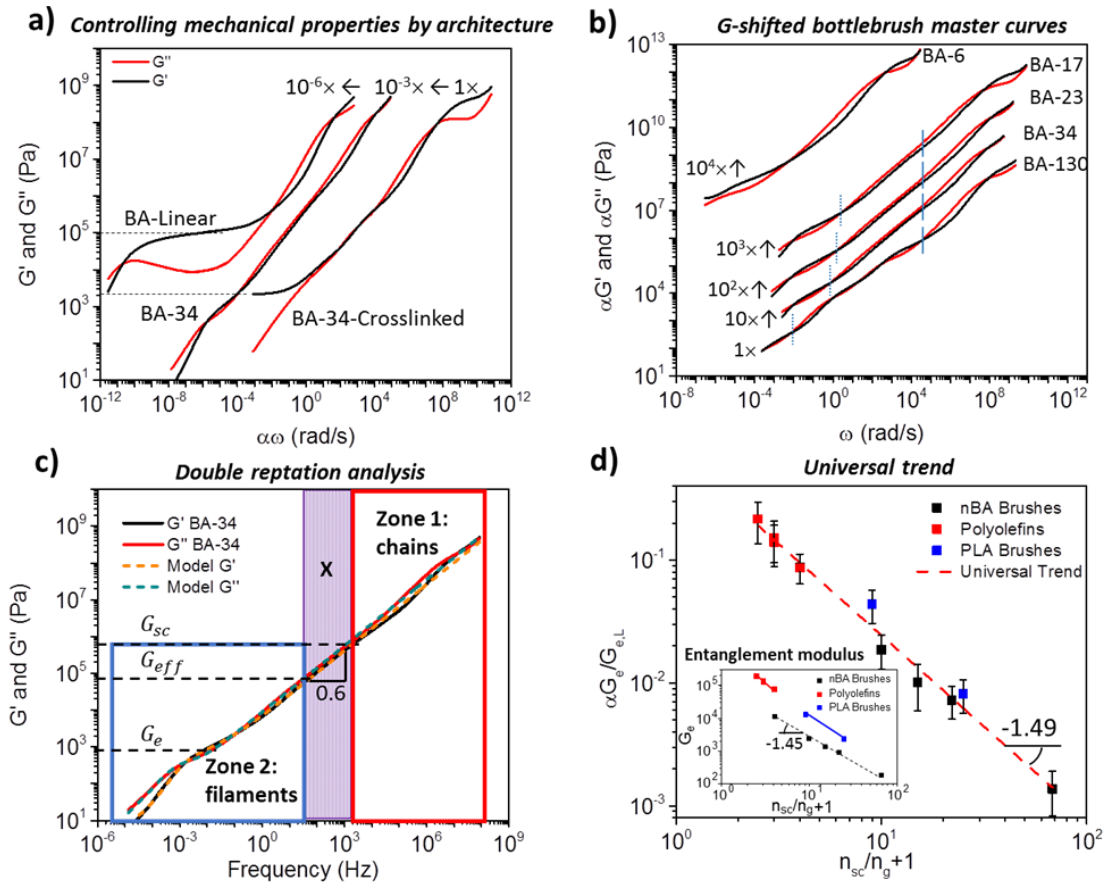

Figure 1.11: Analysis of dynamic mechanical master curves and universal behavior. **a)** Frequency-shifted master curves for the storage (G') and loss (G'') moduli of P*n*BA linear and bottlebrush polymer melts, and a randomly cross-linked bottlebrush elastomer of BA-34 at 25°C. Linear P*n*BA displays characteristic entanglement plateau, while BA-34 display power-law relaxation and weak entanglement plateau at significantly lower modulus. The cross-linked sample displays similar power-law relaxation followed by an elastic modulus ~100 times lower than G_e of linear P*n*BA. **b)** Vertically modulus-shifted master curves of five P*n*BA bottlebrush samples from Table 1.2 **c)** Overlay of experimental rheological master curves (BA-34 at T=25°C) with the double-reptation fit. Two distinct zones (1,2) and a crossover (X) region are observed: (1) relaxation of polymer chains, (2) relaxation of bottlebrush filaments considered as chains of effective monomers, and (X) internal relaxation modes of the effective monomer displaying power-law dependence $G' \cong G'' \sim \omega^{0.6}$. **d)** Log-log plots of the plateau modulus ratio of bottlebrush and linear chain melts ($G_e/G_{e,L}$) as a function of the reciprocal backbone volume fraction determined by DP of bottlebrush side chains (n_{sc}) and grafting density (n_g^{-1}). The data points are normalized to the same chemical composition by $\alpha = (v/b^2 l)^{-3/2}$, while the inset shows the original data for (■) - P*n*BA brushes (double reptation fit of the spectra in b), (■) - polyolefin linear polymers with dense (bottlebrush-like) side groups,[77] and (■) - pLA bottlebrushes.[80] All samples fall on the same universal line with a slope -1.49±0.05, which is consistent with the scaling exponent -1.5 in Equation 1.11.

Additional analysis of the modulus relaxation spectrum identified two characteristic zones in the master curves (Figure 1.11c). Zone 1 (linear chains) includes high frequency glassy and transition relaxation modes of individual chains common to all polymers displaying close match of both the G' curves and G'' curves. Zone 1 has a lower bound corresponding to relaxations on the scale of the side chain (solid vertical lines Figure 1.11b) ($G_{sc} \approx k_b T/n_{sc} v$), beyond which side chains motions become correlated through the backbone. At lower frequencies, we observe Zone 2 (bottlebrush filaments), which corresponds to the relaxation of filament strands comprised of effective monomers of size $D \cong (n_{sc} lb)^{1/2}$ - filament diameter. Zone 2 has an upper bound determined by the size of the effective monomer ($G_{eff} \approx k_b T/D^3$), which indicates the onset of a filament transition zone followed by a short foot of the entanglement plateau (indicated by the crossover in modulus marked with dotted lines in Fig. 1.11b) and the terminal zone. As side-chain DP increases, the plateau becomes less distinct due to growth of the M_e (Table 1.4) resulting in a decrease of the entanglement density. The terminal relaxation zone in the frequency range below the entanglement plateau was not explored in detail due to extremely long relaxation times of large and relatively disperse bottlebrushes, leading to shallower than the classical $G' \sim \omega^2$ and $G'' \sim \omega$ slopes and apparent frequency dependence of the entanglement plateau modulus. The crossover region between Zones 1 and 2 represents a transition from polymer chains to mesoscopic filaments, which includes the internal relaxations within effective monomers composed of side chains coupled through the backbone. In this crossover range, the BA-130 sample also develops an intermediate plateau due to entanglements of its longer side-chains, which do not affect the overall entanglement modulus G_e observed at longer time scales.

1.8 Preliminary elastomers

The architectural reduction of entanglement density within bottlebrush melts provides access to a new range of properties for the design of elastomers with unprecedentedly low elastic modulus and high deformability. In order to expand the super-soft concept from melts into solid materials, and to demonstrate the universality of our method as it relates to differing chemical structures, we have synthesized a series of poly(dimethylsiloxane) (PDMS) bottlebrush elastomers ($n_{sc} = 14$ and $n_g = 1$) with systematically controlled cross-linking densities using ATRP of mono and di-functional macromonomers. For these values of n_{sc} and n_g, our scaling analysis predicts the following dimensions of the entanglement strand: $n_{e,bb} \cong 2{,}900$ (backbone DP) and $M_e \cong 2.9 \times 10^6\ g/mol$ (molar mass). Melts comprised of such PDMS bottlebrushes are expected to exhibit an entanglement modulus of $G_e \cong 800\ Pa$, which (within a numerical prefactor on the order of 1) sets a lower boundary for elastic modulus of PDMS bottlebrush elastomers with $n_{sc} = 14$ and $n_g = 1$. In agreement with this prediction, Figure 1.12a shows a consistent modulus decrease down to 520 Pa with decreasing crosslinking density, which is ca. 400 times softer than $G_{e,lin} \cong 200\ kPa$ measured for linear PDMS melts. Furthermore, the effective dilution of chain entanglements in bottlebrush melts not only reduces the elastic modulus, but also allows higher deformation of the corresponding elastomers.

With the possibility of intelligently designed dry super-soft elastomer it is important to understand how they relate to other molecularly disentangled systems, such as gels. Since mechanical properties of polymeric networks at large strains are particularly sensitive to the network topology, both systems were synthesized using the same crosslinking protocol based on stoichiometric incorporation of tetra-functional cross-link junctions. As evident from the true

stress measurements in Figure 1.12b, bottlebrush elastomers exhibit superior deformability with elastomer-like compression ratio of $\lambda^{-1} = L_0/L \cong 10$ while possessing similar modulus to the gel counterpart (~2,000 Pa). The work of compression at fracture was then measured as $W \cong 0.2\ MJ/m^3$, which is approximately one order of magnitude larger than that of conventional linear PAM gel and one order of magnitude lower that the work of extension at fracture of the designer gels with sacrificial bonds.[89] Note that these bottlebrush elastomers were not designed with any sacrificial bonds or advanced toughening mechanisms, which points to great potential for further enhancement of toughness through molecular design. Figure 1.12c displays a visual comparison of the compressibility of a PAM hydrogel with a poly(dimethylsiloxane) (PDMS) bottlebrush elastomer, in which the volume fraction of backbone segments is similar to the polymer fraction of the hydrogel.

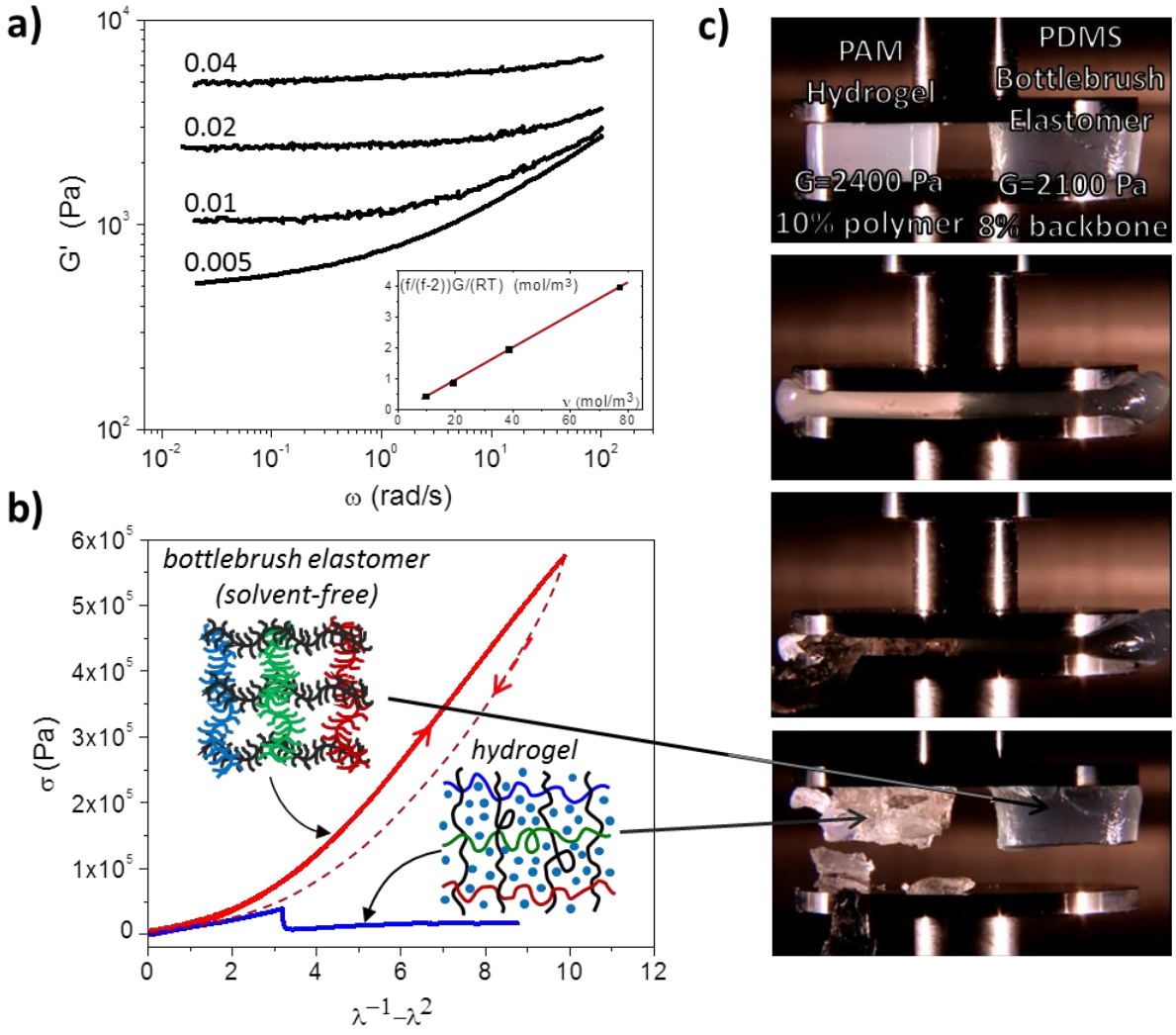

Figure 1.12: Super-soft and super-extendable elastomers. (a) Poly(dimethylsiloxane) (PDMS) bottlebrush elastomer displaying moduli on the order of 100 to 1000 times softer than linear PDMS entanglement modulus as a function of crosslinker/macromonomer fraction as indicated. Inset: The plateau modulus decreases with calculated crosslinking density, where the slope gives 5% crosslinker reactivity and the zero-ν intercept suggests ca. 10% of dangling strands. **(b)** True stress was measured during compression of a pDMS bottlebrush elastomer and poly(acrylamide) (PAM) hydrogel possessing similar volume fractions of backbones and polymer chains, respectively. The bottlebrush elastomer exhibit considerably higher fracture energy than gel counterparts, while both materials show a similar modulus of ~2000 Pa. Bottlebrush samples display considerably higher compressibility (compression ratio at break $\lambda^{-1} = L_0/L \cong 10$ for bottlebrushes and $\lambda^{-1} \cong 3$ for the PAM hydrogel). **(c)** A compression behavior of a PAM hydrogel with 10 wt.% polymer and a shear modulus of G=2100 Pa is compared with that of a (PDMS) bottlebrush elastomer with 8 wt.% cross-linked backbone and G=2400 Pa.

1.9 Conclusion and outlook

In conclusion, we have presented the scaling relations of bottlebrush entanglements and explored the scaling predictions for other branched architectures. Using a combination of NMR, GPC, and LB-AFM we have characterized a series of bottlebrush molecules to understand their three key structural parameters (n_{bb}, $n_{g,}$ n_{sc}). Rheological measurements along with three analysis protocols proved that the scaling of dense bottlebrush molecules matches perfectly with the scaling prediction of $G_e \sim (n_{sc}/n_g)^{-3}$. This was tested not only for our molecules but for similar molecules from previous studies. This work has elucidated the missing link in our understanding of bottlebrushes with respect to both common linear and comb-like polymers. In yet another step forward, has led to the discovery of previously unexpected properties in bottlebrush elastomers, opening the way for the design of new classes of soft elastic materials. Bottlebrush-based materials have redefined the limit of "dry" elasticity allowing for single component dense polymer materials with moduli on the order of 100 Pascals, which is one thousand times softer than conventional elastomers and melts. In the following chapter we see that these structure not only expand property ranges but display new property relations that can be utilized for practical materials. Before the full impact of brush-like architectures can be understood superior methods for characterizing their structures must be developed.

CHAPTER 2: CHARACTERISATION OF BOTTLEBRUSH ARCHETECTURES[2]

2.1 Introduction and objectives

The previous chapter displays the mathematical relations between modulus and brush-like architectural parameters. These relations ultimately rely on the fraction of side chains (n_{sc}/n_g) thus making accurate characterization of this quantity paramount. For this purpose we turn to the 2D properties of bottlebrushes. Bottlebrush molecules have large molecular dimensions allowing for accurate counts of individual molecules and accurate measurements of n_{bb} assuming a fully extended backbone at low values of n_g. In past studies this architectural property has been used to discover a series of interesting properties including flow-enhanced molecular diffusion, [90] epitaxial ordering,[91] and conformational transitions[92] that triggered flow instability.[93] Molecular sensors have been designed to gauge both pressure gradient and friction coefficient at the substrate.[92] These studies culminated with the discovery of scission of covalent bonds during adsorption and spreading of branched macromolecules on a substrate.[94-96] All of these fascinating properties occur due to the interactions between bottlebrush side chains and 2D substrates, however the rules governing how side chains differentiate themselves into a population which is

[2]This chapter previously appeared as an article in Macromolecules. The original citation is as follows: Burdyńska, J.; Daniel, W.; Li, Y.; Robertson, B.; Sheiko, S. S.; Matyjaszewski, K. *Macromolecules* 2015, **48**, 4813−4822.

adsorbed onto a surfaces and a population forced into a cone above the substrate. While the adsorbed side chains chain extend to maximize the area of the substrate covered by the deposited brush, the desorbed side chains form a "cap" sitting on top of the monolayer of the adsorbed side chains.[82] The conformation of surface-confined bottlebrushes, including the length, width, and flexibility, or persistence length of the backbone, is largely controlled by the fraction of adsorbed side chains. However, if the side chains exhibit broad polydispersity, the conformation also depends on the length distribution of adsorbed and desorbed side chains. There are two possible adsorption processes. In one case the adsorption process is random and the dispersity of the adsorbed side chains is equal to the overall dispersity. In another case, favoring adsorption of the longest side chains, one should observe a large separation between adsorbed macromolecules and also an increased width of single molecules due to predominate adsorption of the longest side chains. In this chapter we explore the relation between side chain distribution and side chain adsorption as well as use AFM to accurately analysis n_{sc}/n_g.

2.2 Synthesis and initial characterization

The samples with monomodal sidechains were prepared in the same fashion as the samples in Chapter 1. Bimodal samples were prepared by interrupting the growth of a select fraction of side chains via biradical coupling using a TEMPO-based persistent radical. The TEMPO capped chains halted polymerization while the uncapped chains continued to grow to the specified DP. Full synthetic details can be found in Burdyńska, J. et al. *Macromolecules* 2015, **48**, 4813−4822. Scheme 2.1 gives further information. Figure 2.1 displays a representative GPC trace confirming the bimodal nature of sidechain growth using the TEMPO mediated approach.

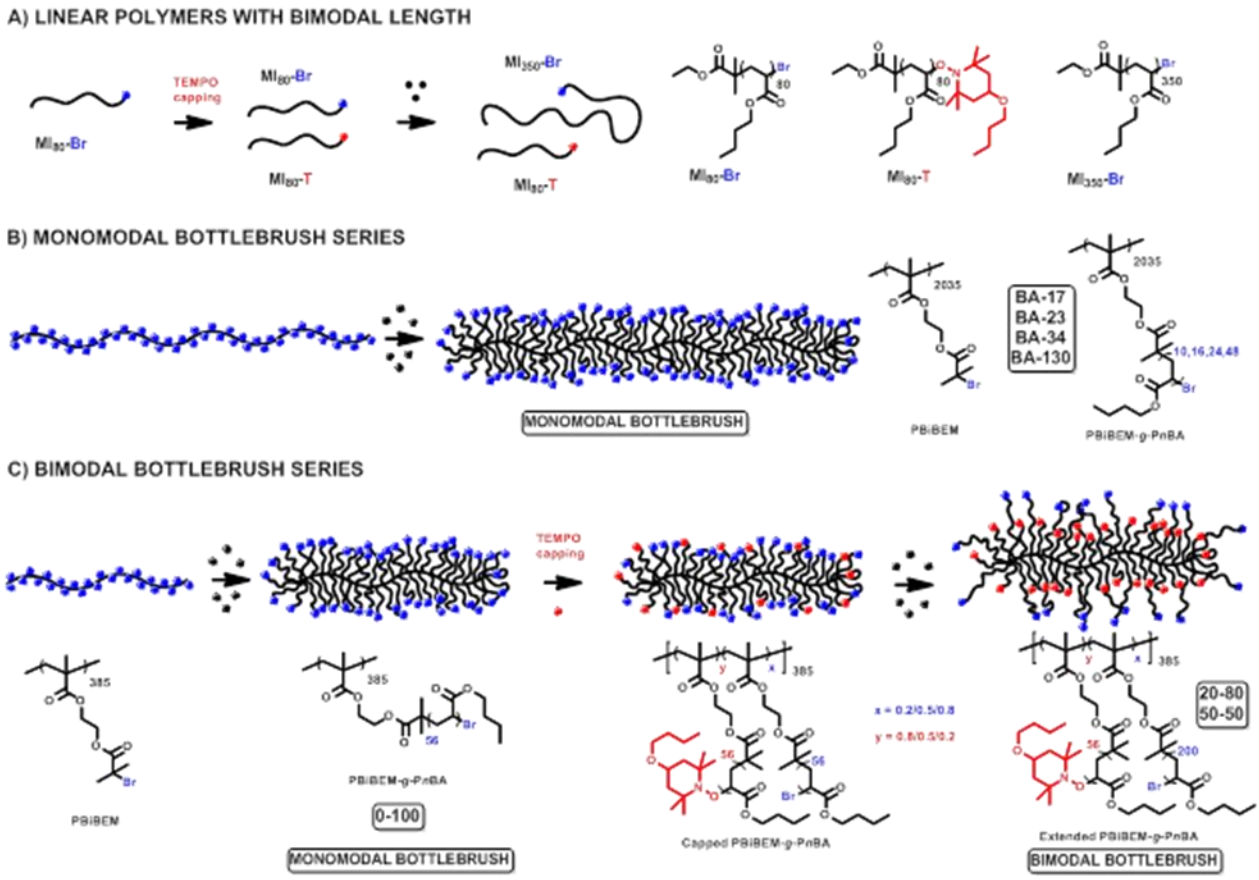

Scheme 2.1: The synthetic approach for **A)** linear polymers with a bimodal length distribution and **B)** monomodal, and **C)** bimodal bottlebrushes.

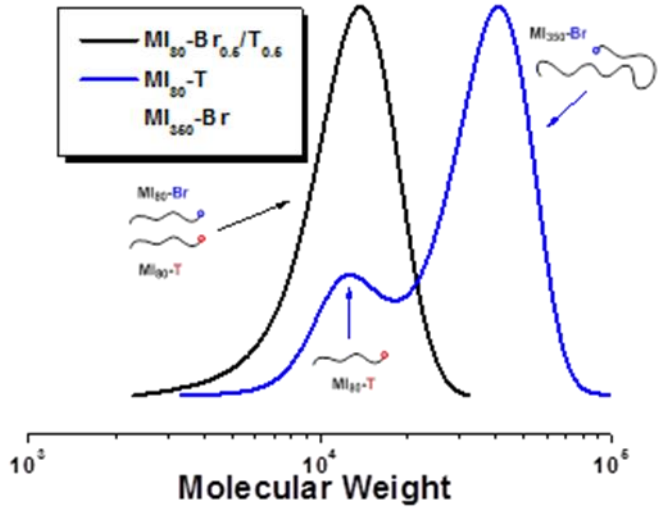

Figure 2.1: Initial GPC. GPC traces of linear **MI_{80}-Br** macroinitiator capped with 0.5 eq. of 4-butoxy-TEMPO before (black) and after (blue) extension with *n*BA.

2.3 NMR and GPC analysis

The conversion of monomers was determined from ^{1}H NMR spectra recorded in $CDCl_3$ using a Brüker 300 MHz spectrometer. Molecular weight distributions of the polymers were characterized by gel permeation chromatography (GPC) using Polymer Standards Services (PSS) columns (guard, 10^5, 10^3, and 10^2 Å), with THF eluent at 35 °C, flow rate 1.00 mL/min, and differential refractive index (RI) detector (Waters, 2410). The apparent number-average molecular weights (M_n) and molecular weight dispersities (M_w/M_n) were determined with a calibration based on linear poly(methyl methacrylate) (PMMA) standards and diphenyl ether as an internal standard, using WinGPC 6.0 software from PSS (Figure 2.2, Table 2.1). Bottlebrush samples were analyzed by GPC with light scattering detection to measure molecular weight distribution.

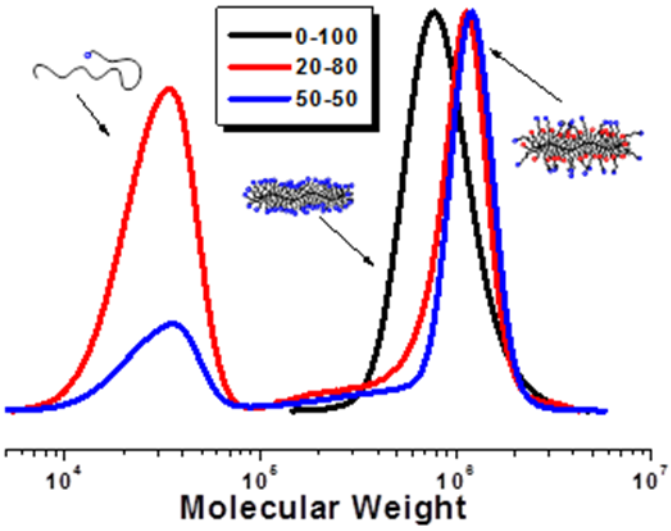

Figure 2.2: GPC of bimodal species. GPC traces of bottlebrush with P*n*BA grafts with the mole fraction of extended (long) side chains: 0 % (**0-100**, black), 20 % (**20-80**, red) and 50 % (**50-50**, blue) (low molecular weight peaks correspond to linear P*n*BA impurities formed during the extension of side chains).

The chain-extension to form bottlebrushes **20-80** and **50-50** was confirmed by the shift of GPC traces towards higher molecular weight values, when compared to sample **0-100** (Figure 2.2, blue and red). In all cases GPC signals were monomodal with narrow molecular weight distributions ($Đ$~1.2) demonstrating the formation of well-defined bottlebrushes (Table 2.1). However, a more detailed analysis of GPC traces of **20-80** and **50-50** showed the appearance of low molecular weight peaks, which was ascribed to the formation of a linear P*n*BA with yet unknown mechanistic origin. The low molecular weight impurities present in brushes **20-80** and **50-50** was removed via selective precipitation of the bottle brushes from THF solution into methanol at room temperature, providing pure samples of the bimodal bottlebrushes.

Table 2.1: GPC characterization of monomodal and bimodal bottlebrush series.

Series	Sample	$I_{eff}\ n_{sc}$ [a]	n_{sc} [b]	I_{eff} [c]	$M_n \cdot 10^{-5}$	$Đ$ [d]
Monomodal	**BA-17**	10	17	0.6	29	1.5
	BA-23	16	23	0.7	47	1.6
	BA-34	24	34	0.7	58	1.6
	BA-130	48	130	0.4	179	1.5
Bimodal	**0-100**	56	N/A	N/A	7.6	1.2
	20-80	(200-56)/85*	N/A	N/A	9.1	1.2
	20-80	(200-56)/128*	N/A	N/A	10.1	1.2

[a] Number average degree of polymerization of side chance calculated from the monomer conversion determined by ^{1}H NMR, using the equation: $I_{eff}\ n_{sc} = \left(1 - \frac{A_{[M]} \times A_{[Anisole]_0}}{A_{[M]_0} \times A_{[Anisole]}}\right) \times DP_{target}$, where I_{eff} is the initiation efficiency, $A_{[M]_0}$ and $A_{[M]}$ are areas for vinyl signals of the monomer at the beginning and end of the polymerization, and respective integrations of an internal standard, anisole protons. [b] Number average degree of polymerization of side chains after cleaving from the brush backbone, measured using THF GPC with PS standards. [c] Initiation efficiency of

the grafting process [d] Dispersity of bottlebrush polymers $Đ = M_w/M_n$ determined by THF GPC using PS standards. [*]Determined from the equation: $n_{sc} = n_{short} \times x_{short} + n_{long} \times x_{long}$, where n_{short} and n_{long} are degrees of polymerizations corresponding to short and long grafts of bimodal bottlebrushes, and x_{short} and x_{long} are their respective mole fractions.

2.4 LB-AFM analysis and results.

The combination of AFM and the LB techniques is a very powerful method for quantitative characterization of the geometric dimensions and molecular weight distribution of branched macromolecules. While the LB technique allows for preparation of well-defined monolayers under controlled surface area per monomeric unit (A_{BR0}), AFM provides images of individual bottlebrush molecules within these monolayers (Figure 2.3). By counting the number of molecules per unit area(A_{BR}^{-1}), the number average molecular weight was determined as $M = M_0 N_{Av} A_{BR} / A_{BR,0}$ where $M_0 = 128\, g/mol$ – molar mass of BA repeat unit, N_{Av} – Avogadro's number, A_{BR} – area per molecule, and $A_{BR}/A_{BR,0}$ – number of monomeric units per bottlebrush macromolecule. The molecular images also allow determination of the contour length (L) and average brush width (W). Note that the W measured from a dense monolayer agrees well with the W of a single brush molecule in a sparse monolayer prepared by spin casting (Figure 2.4).

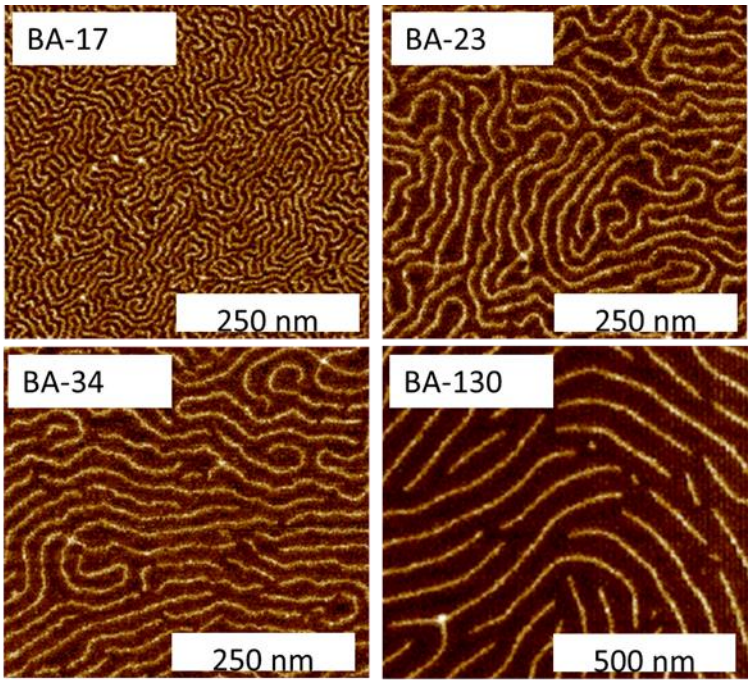

Figure 2.3: AFM of LB monolayers. AFM height images of monomodal bottlebrushes with different degrees of polymerization (n_{sc}) of the side chains. Images were taken from LB trough monolayers transferred onto mica substrates.

Van der Waals attraction between mica and P*n*BA favors spreading of the side chains on the surface of a mica substrate, thus allowing for clear resolution of individual bottlebrush molecules that demonstrate characteristic worm-like conformation (Figure 2.3). In general, longer side chains result in a greater brush width and consequently, greater intermolecular distance (Table 2.2). This behavior is ascribed to strong steric repulsion between densely grafted side chains, which prevents overlap of adsorbed bottlebrushes. The AFM micrographs also demonstrate a steady increase in the stiffness of the adsorbed bottlebrushes with increasing DP of the side chains. For all monomodal bottlebrushes, the L values remained close to 500 nm (Table 2.2), ensuring that no carbon-carbon scission occurred within bottlebrush backbones upon deposition on the substrate.[94-96]

AFM micrographs of Langmuir-Blodgett (LB) monolayers of bimodal bottlebrush series are shown in Figure 2.4a-c. As expected, both the stiffness and width of the adsorbed bottlebrushes increased with the molar fraction of longer side chains: While sample **0-100,** with 100% short side chains ($n_{short} = 56$), displayed a worm-like conformation, the **50-50** bottlebrushes with 50% of the long side chains ($n_{long} = 200$) behaved as rods with a greater macromolecular width. The measurements made on the dense LB monolayers are consistent with conformation of single bottlebrushes prepared by spin-casting as shown by the insets in Figure 2.4a-c. Unlike sample **0-100**, the **20-80** and **50-50** bottlebrushes in the insets revealed an outer halo of diffuse side chains, which was consistent with their bimodal composition (Figure 2.4a-c). From AFM images of the LB monolayers, we have determined the average lengths *L* and widths *W* of bottlebrushes (Table 2.2). In all cases, *L* was in the range of ~130 nm, which is consistent with the use of the same macroinitiator for all molecules. The brush width *W*, generally, increases with the fraction of the longer side chains. However, as discussed later in this chapter, the brush width is determined by the fraction and DP of the adsorbed side chains, which may be different from the number average DP of the side chains of the overall brush.

Table 2.2: Results of LB-AFM analyses of monomodal and bimodal bottlebrush series

Series	Entry		W^a / nm spin cast	W^a / nm LB	L^a / nm LB
Monomodal	BA-17		N/A	11±1	513±18
	BA-23		N/A	18±1	515±18
	BA-34		N/A	26±3	495±25
	BA-130		N/A	69±5	517±3
Bimodal	0-100		50±4	51±2	134±2
	20-80	short	50±7	78±4	133±3
		long	63±4		
	50-50	short	58±5	98±8	130±2
		long	82±4		

[a] Length (L) and width (W) of bottlebrushes obtained from AFM images of LB films or spin casted bottlebrushes on mica substrates.

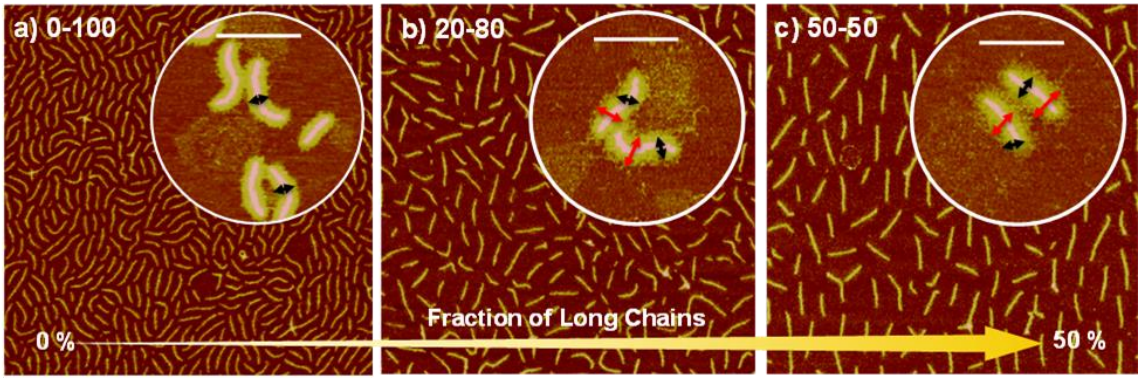

Figure 2.4: AFM of LB monolayers and spin cast bimodal materials. 2×2 μm^2 AFM height micrographs of LB monolayers prepared from bottlebrushes with **a)** monomodal, **0-100**, n_{short}=56, and bimodal graft lengths **b) 20-80**, n_{long}=200 (80%) and n_{short}= 56 (20%), and **c) 50-50**, n_{long}=200 (50%) and n_{short} = 56 (50%), on a mica surface; Images of single brush molecules prepared by spin-casting methods are shown in circles (the scale bar is 200 nm). Black and red arrows indicate the dense core of the shorter side chains and diffusive hallo of the longer grafts, respectively.

The AFM data were then combined with the LB studies to determine the number average DP (n_{sc}/n_g) of the side chains and grafting density n_g^{-1} of the side chains. From the LB isotherms (Figure 2.5a), we have obtained the area per BA monomer ($A_{BR,0}$) for each tested sample, including

that of linear PnBA ($A_{L,0}$). The ratio $\phi_m = A_{BR,0}/A_{L,0}$ provides quantitative information about the fraction of adsorbed monomers.[Error! Bookmark not defined.] In the case of monomodal brushes the $A_{BR,0}$ values were practically the same, showing no dependency on the DP of side chains (n_{sc}). Bimodal bottlebrushes, however, displayed an increase of $A_{BR,0}$ values with increasing dispersity of the side chains, which indicates a higher fraction of adsorbed monomeric units. The results of LB analysis can be found in Table 2.3. It should be noted that the value of $A_{BR,0}$ is specific to the transfer pressure of the LB monolayers. A transfer pressure of π=0.50 mN/m was chosen as it represents the onset of dense monolayer formation (Figure 2.5A). For each sample, we also controlled the transfer ratio r_T (Table 2.3).

Table 2.3: The results of AFM and LB analyses for monomodal and bimodal bottlebrushes.

Sample	$A_{BR,0}$/ nm^{2},[d]	r_T [e]	n_{sc}/n_g	n_{sc}[f]	n_g[-1 g]	ϕ_m[h]	ϕ_{sc}[i]	$Đ$[j]	n_a/n_{sc}[k]	n_{max}/n_{sc}[l]
BA-17	0.28	0.88	9	17	0.51	0.68	0.60	1.12	1.16	1.65
BA-23	0.29	0.89	14	23	0.62	0.71	0.49	1.18	1.43	1.65
BA-34	0.29	0.90	21	34	0.62	0.71	0.49	1.30	1.43	1.71
BA-130	0.27	0.98	67	130	0.53	0.66	0.58	1.10	1.15	1.63
0-100	0.28	0.82	56[a]	N/A	0.50[b]	0.68	0.61	1.20[b]	1.12	1.68
20-80	0.37	0.81	85[a]	N/A	0.50[b]	0.90	0.61	1.45[c]	1.48	1.64
50-50	0.33	0.89	128[a]	N/A	0.50[b]	0.80	0.61	1.32[c]	1.32	1.69

[a] Estimated as $x_{short}n_{short} + x_{long}n_{long}$ where x_{short} = (1-x_{long}) = 0.8/0.5 and x_{long} = 0.2/0.5 are respective mole fractions of long and short grafts, and n_{short} = 56 and n_{long} = 200 correspond to DPs of short and long grafts respectively. [b] Estimated from typical values. [c] Calculated as $\frac{(x_{short}n_{short})^2+(x_{long}n_{long})^2}{n_{sc}{}^2}$. [d] The area per *n*BA monomer in an LB film transferred at 0.5 mN/m. [e] Transfer ratio – the ratio between molecular area in LB film to the area on LB trough. [f] Number average DP of side chains determined by THF GPC of cleaved side chains, using PS standards. [g] The grafting density of the side chains see eq. 1 [h] Fraction of adsorbed monomers. [i] Fraction of adsorbed side chains [j] Number average molecular weight distribution obtained from THF GPC measurements. [k] The ratio of the adsorbed DP (n_a) over the n_{sc} as $\frac{n_a}{n_{sc}} = \frac{\sigma * A_{BR0}}{l_0{}^2 2}$. [l] n_{max}/n_{sc}, where n_{max} is the average DP of adsorbed side chains assuming the longest side chains adsorb first.

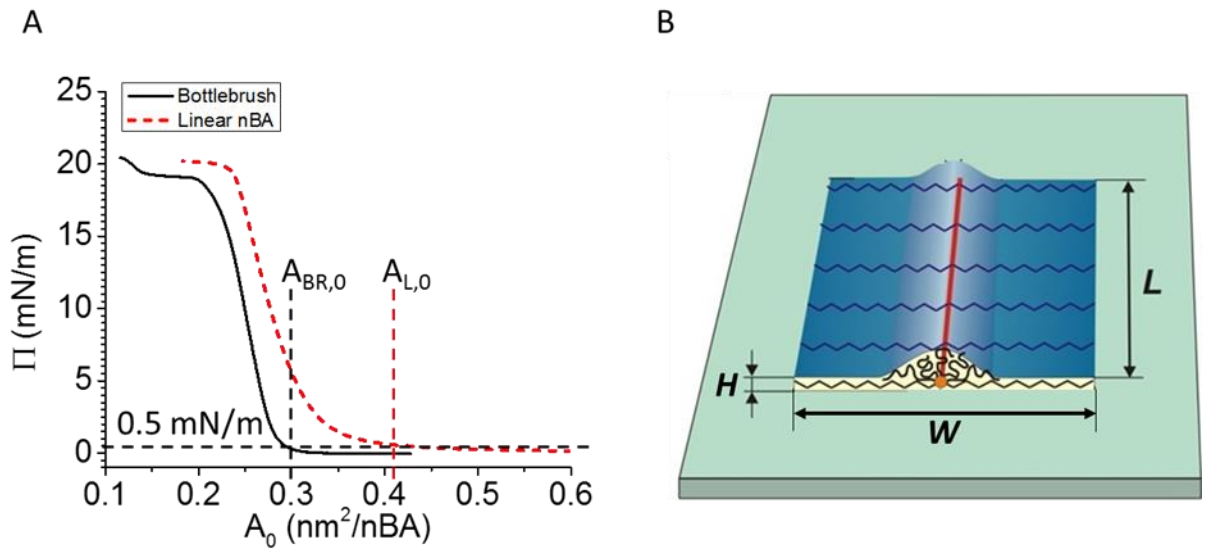

Figure 2.5: LB technique. (A) LB isotherms of surface pressure versus monomer area of linear and bottlebrush BA samples. Values of $A_{BR,0}$ and $A_{L,0}$were taken at identical surface pressures (0.5 mN/m) to insure comparison of mono layers at the same level of compression. (B) Schematic of an adsorbed bottlebrush displaying geometric dimensions (L, W, and $h \sim A_{L,0}^{-1}$) as well as fractions of the adsorbed and desorbed side chains.

The concurrent measurements of the brush width W and monomer area A_{BR0} allow for accurate calculation of n_{sc}/n_g as

$$\frac{n_{sc}}{n_g} = r_T \frac{A_{sc}}{A_{BR,0}} = r_T \frac{\alpha W l_o}{A_{BR,0}} \qquad 2.1$$

where A_{sc} – area per side chain in an LB film, $A_{BR,0}$ - area per BA on an LB trough upon transfer to a solid substrate, r_T–transfer ratio correction for the error between $A_{BR,0}$ on the LB trough and A_{BR0} on the AFM substrate, l_0=0.25 nm - length of the nBA monomer unit, and $\alpha = (1 + \pi r_T W/4L)$ - correction factor for semicircular chain ends. Note that r_T is applied only to the brush width, since L does not change upon transfer of the LB film to the solid surface and the correction becomes trivial for increasing L increases. It is also important to note that $W \sim A_{BR,0}$ and, therefore, n_{sc} does not physically depend on the transfer area $A_{BR,0}$. From Equation 2.1, we obtain the

grafting density (n_g^{-1}) using the number average side chain DP (n_{sc}) measured independently through the cleavage of the side chains. Side chain cleavage was not possible for the bimodal samples due to their degradation, which is a consequent of the synthetic method used to create the bimodal brush samples. In this case, we determined the grafting efficiency as $n_g^{-1} \cong I_{eff}$ estimated from previous syntheses (Table 2.3).

As mentioned in the introduction, adsorption of side chains leads to partitioning of the grafts into adsorbed and desorbed populations (Figure 2.5B), which is described by two quantities: (i) the fraction of adsorbed monomer units and (ii) the fraction of desorbed side chains. The fraction of adsorbed monomer units $\phi_m = \frac{Z_{m,a}}{Z_m} = \frac{A_{BR,0}}{A_{L,0}}$, where $Z_m = {A_{BR,0}}^{-1}$ – number of monomer units per unit area. $Z_{m,a} = {A_{L,0}}^{-1}$ – number of adsorbed monomers per unit area, $A_{BR,0}$ – is the area per BA monomer in LB monolayers of bottlebrushes (Table 2.3), and $A_{L,0} = 0.41\ nm^2/BA$ – area per BA monomer unit in a sample of linear P*n*BA transferred at the same film pressure of π=0.5 mN/m. The $A_{L,0}$ value from LB was verified by calculating it as $A_{L,0} = v/h$, where $v = 0.2\ nm^3$ - volume of nBA monomeric unit and $h = 0.5\ nm$ - thickness of P*n*BA monolayer.**Error! Bookmark not defined.** The fraction of adsorbed side chains $\phi_{sc} = \frac{Z_{sc,a}}{Z_{sc}} = \frac{2n_g {l_0}^2}{A_{L,0}}$, where $Z_{sc} = \left(n_g l_0\right)^{-1}$ – total number of side chains per backbone unit length in a bottlebrush macromolecule with grafting density n_g^{-1} and $Z_{sc,a} = 2l_0/A_{L,0}$ – number of adsorbed side chains per backbone unit length. The obtained ϕ_m and ϕ_{sc} values are summarized in Table 2.3. The ratio of these two fractions gives the average adsorbed side chain as

$$n_a = \frac{\phi_m}{\phi_{sc}} n_{sc} = \frac{A_{BR,0}}{2n_g {l_O}^2} n_{sc} \qquad 2.2$$

Three possible outcomes for n_a were anticipated:

(i) the sample would maximize energetic interactions with the surface by adsorbing the longest side chains resulting in $n_a = n_{max}$,

(i) the probability of adsorption of a side chain linearly increases with its DP, thus the n_a should equal to the weight average DP ($n_a = n_w$), and

(ii) the side chains would adsorb in a perfectly random manner resulting in $n_a = n_{sc}$.

As displayed in Table 2.3, the values of n_a/n_{sc} (Equation 2.2) in monomodal bottlebrushes show excellent agreement the values of $Đ$ obtained by GPC of cleaved side chains. Correspondingly, Figure 2.6A (Equation 2.2) displays the perfectly linear relation between n_a and the weight average (n_w). Although the bimodal bottlebrushes could not have their side chains cleaved to obtain exact values of n_{sc}, the LB-AFM analysis indicated that the obtained values of n_a/n_{sc} were nearly identical to $Đ$ estimated from NMR measurements of the bimodal samples. As such, both the monomodal and bimodal samples display the universality of the relationship between different brush architectures, which suggests that $n_a = n_w$. This result was unexpected as it was initially assumed that the longest side chains would preferentially adsorb maximizing the favorable energetic interactions. To definitively rule out the above assumption, a theoretical $n_{\max}$ was calculated from the GPC distribution of side chains for a given ϕ_m. As seen in Table 2.3, the ratio of n_{max}/n_{sc} consistently over estimated the value, while n_a/n_{sc} matched $Đ$ within 10% error.

With the empirical relation $n_a/n_{sc} = Đ$, which has been experimentally verified for the monomodal brushes, Equations 2.1 and 2.2 provide a relationship between the brush width and the number average DP of adsorbed side chains for any single polymer brush molecule.

$$Đn_{sc} = \frac{\alpha W}{2l_0} \qquad 2.3$$

Figure 2.6 B (Equation 2.3) displays a universal coordinate related the brush width with n_{sc}, which is valid for brushes with the same value of $Đ$. The relations slope gives the average $Đ$ of the monomodal samples side chains, within 10% error.

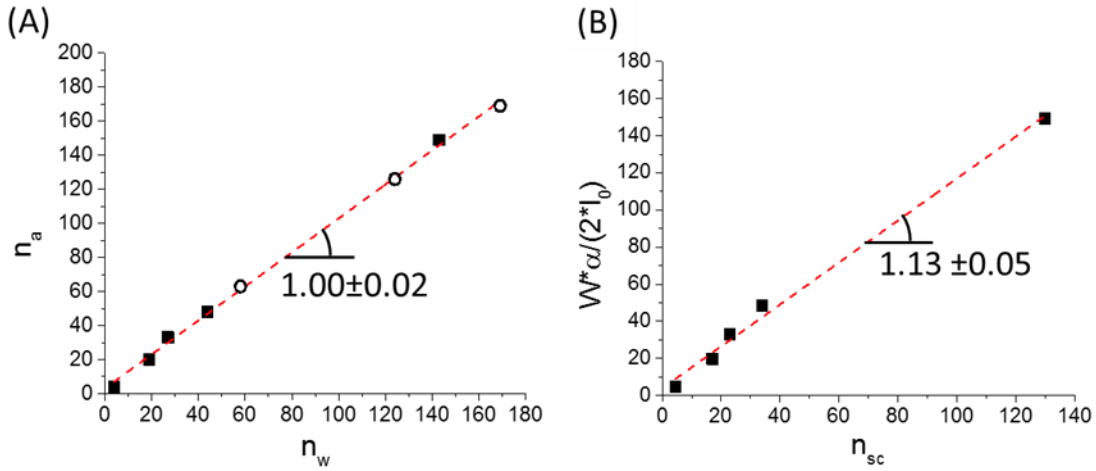

Figure 2.6: Derivation of dispersity from 2D data. **A)** The linear plot of n_a vs. n_w where n_w – is the weight average DP taken from cleavage GPC and NMR measurements. The first data point represents theoretical a macroinitiator; the monomodal and bimodal bottlebrushes are marked as black squares and open circles respectively. **B)** A universal coordinate, valid for brushes with the same vale of $Đ$, is derived from the eq. 3 vs. n_{sc} to yield the average side chain dispersity of monomodal bottlebrushes.

2.5 Conclusion and outlook

The structural details of bottlebrush polymers were explored through a combination of new bottlebrush synthesis techniques, cleavage of side chains, and an extended use of LB-AFM analysis. A procedure for the preparation of molecular bottlebrushes with a bimodal length distribution of side chains was developed. A selective and quantitative capping of propagating radicals with a persistent radical, 4-butoxy-TEMPO was utilized to deactivate a fraction of bromine end groups in polymers prepared by ATRP. A consecutive chain extension of the

remaining fraction of active side chains resulted in well-defined molecular bottlebrushes with bimodal length distribution of side chains but with overall narrow molecular weight distributions ($Đ$ ~1.2). Utilizing LB-AFM analysis in conjunctions with Equation 2.1 yields accurate analysis of the essential n_{sc}/n_g which proved to be central to the understanding of brush-like entanglement modulus in Chapter 1. Additional analysis combining of the GPC of cleaved side chains and Equation 2.2 allows for separation of the n_{sc}/n_g variable into its two distinct parts which remain important in the following chapters of this dissertation. The combination of LB-AFM, and GPC analysis is central to our ability to manipulate the properties of new soft brush-like melts and elastomers leading to unprecedented control over mechanical properties. Going further the dispersity $Đ$ of bottlebrush side chains can also be accurately measured using these techniques and Equation 2.3, strengthening the diagnostic power of the techniques presented in this chapter. The analysis of the monomodal bottlebrushes showed that the number average DP of adsorbed side chains (n_a) was equal to the weight average side-chain size n_w, suggesting that adsorption probability of the side chains was proportional to their DP. This same analytical method was then applied to a more complex bimodal bottlebrush system and led to the same conclusion, i.e. $n_a \cong n_w$ and Đ$\sim A_{BR,0} \sim W$. Understanding of how these molecules adhere to 2D surfaces will play an important role in future studies of such materials as surface coatings for antifouling properties.

CHAPTER 3: PROPERTIES OF BOTTLEBRUSH ELASTOMERS[3]

3.1 Introduction and objective

The previous chapters established the untangled nature of brush-like polymers, proved the theoretical scaling of dense bottlebrushes, and displayed the power of combined LB-AFM as a technique for analyzing architectural parameters. Beyond disentanglement, brush-like structures offer other unique properties not represented in typical linear structures. In this chapter we discuss how crosslinking dense bottlebrushes into elastomer reveals their uses as strain hardening materials. Before the limits of branched architectures as super-soft materials can be tested first reliable elastomers must first be synthesized, and a proper method for analyzing their physical properties must be developed. The objective of this chapter is to introduce techniques for producing bulk samples of molded bottlebrush elastomers suitable for mechanical testing. These samples were analyzed by linear extension experiments and using a superior method of characterizing stress profiles first developed by Dr. Dobrynin.

Elimination of polymer chain entanglements in bottle-brush systems allows tuning bulk mechanical properties over a remarkably broad range without changing chemical composition. By

[3] Much of this chapter previously appeared as an article in Macromolecules. The original citation is as follows: Vatankhah-Varnoosfaderani, M.; Daniel, W. F. M.; Zhushma, A. P.; Li, Q.; Morgan, B. J.; Matyjaszewski, K.; Armstrong, D. P.; Spontak, R. J.; Dobrynin, A. V.; Sheiko, S. S. Bottlebrush Elastomers: A New Platform for Freestanding Electroactuation. *Adv. Mater.* **2017**, *29*, 1604209.

independently varying the side-chain length and crosslink density, we can synthesize elastomers with Young's moduli ranging from 1 MPa down to ≈100 Pa and elongations at break up to ≈10.[97] In light of the unique properties achievable with bottlebrush elastomers, we first outline the basic principles elastomer stress characterization and how it relates to the bottlebrush architecture.

For a broad class of unentangled polymer networks, it has been demonstrated[98] that the stress–strain relation can be expressed in universal form as:

$$\sigma_{true}(\lambda) = \frac{G}{3}(\lambda^2 - \lambda^{-1})\left[1 + 2\left(1 - \frac{\beta I_1(\lambda)}{3}\right)^{-2}\right] \quad 3.1$$

where $I_1(\lambda) = \lambda^2 + 2/\lambda$ corresponds to the first invariant for uniaxial network deformation at a constant volume. Thus, the elasticity of a bottlebrush network is effectively described by two parameters i) the structural shear modulus ($G \cong \rho k_b T/n_s$) characterized by the number of monomeric units in the network strand $n_s \cong n_x(n_{sc}/n_g + 1)$, and ii) the strand elongation ratio at rest ($\beta = \langle R_{in}^2 \rangle / R_{max}^2$) defined as the ratio of the mean square end-to-end distance of a network strand in the as-prepared elastomer and the square of the length of a fully extended strand. Here, ρ - the monomer number density, k_B - the Boltzmann constant, and T - absolute temperature. It is important to recognize that β controls the strain-stiffening which is important to many applications requiring strain adaptive properties during high deformations. Unlike linear-chain systems ($n_{sc} = 0$), for which G and β depend only on crosslink density as $\sim n_x^{-1}$ bottlebrush elastomers allow for orthogonal control of modulus and extensibility through variation of the backbone fraction n_g/n_{sc} as Equation 3.2 and 3.3.[97]

$$G = C_1 \frac{\rho k_B T}{n_x(n_{sc}/n_g + 1)} \sim \frac{n_g}{n_{sc}} n_x^{-1} \quad 3.2$$

$$\beta = C_2\left(\frac{n_{sc}}{n_g}+1\right)^{1/2} n_x^{-1} \cong \sqrt{\frac{n_{sc}}{n_g}}\, n_x^{-1} \qquad 3.3$$

where C_1 and C_2 are numerical prefactors on the order of unity (0.3 and 3.1 obtained for our systems) that account for specific network compositions. In the following chapters these equations are expanded and the full implications of orthogonal control of G and β, however in this chapter will discuss the behavior of dense bottlebrush elastomer. From Equation 3.2 and 3.3, we can draw several important conclusions relevant to the performance of bottlebrush elastomers. First, bottlebrush networks are softer than their entangled linear-chain counterparts. Second, the additional architecture parameter $\varphi = n_g/n_{sc}$ (molar fraction of the bottlebrush backbone) allows for simultaneous reduction of the modulus ($G \sim \varphi$) and enhancement of strain-stiffening ($\beta \sim \varphi^{-1/2}$), which provides an unexplored molecular-level approach for elasticity.

3.2 Synthesis

Two series of bottlebrush elastomers with poly(dimethylsiloxane) (PDMS) side chains possessing n_{sc} = 14 and 28 have been prepared by photoinitiated radical polymerization of monofunctional macromonomers in the presence of difunctional crosslinkers. This polymerization method allowed for more mild reaction conditions that controlled radical polymerizations. Because of this the multi-gram samples could be produced in molded shapes for mechanical testing. For full synthetic details see Vatankhah-Varnoosfaderani, M., et al. *Adv. Mater.* **2017**, *29*, 1604209.

3.3 Characterization

3.3.1 PDMS Conversion

The conversion of PDMS macromonomer during atom transfer radical polymerization was determined from ^{1}H NMR spectra recorded in deuterated chloroform ($CDCl_3$) using a Brüker 400 MHz spectrometer. To measure monomer conversion in elastomers, unreacted monomers were washed out by swelling the elastomers in chloroform and deswelling in THF three times, followed by drying at ambient temperature and fully drying at 50 °C.

3.3.2 Mechanical analysis

To investigate the basic mechanical properties of the bottlebrush samples, the elastomer sample films were punched into dumbbell samples with bridge dimensions of 12 mm × 2 mm × 1–2 mm. The samples were loaded into an RSA-G2 DMA (TA Instruments) and subjected to a constant Hencky strain rate of 0.003 strain per second until rupture occurred. All bottlebrush films were subjected to triplicate testing to ensure accuracy of the data. The resulting stress strain curves were then analyzed with Equation 3.1 using Origin 2016 software.

To display the unentangled nature and highly elastic behavior of PDMS bottlebrush elastomers, rheological master curves were produced for samples with n_x = 50, 67, 100, and 200, $n_{sc} = 14$, and $n_g = 1$. The frequency (ω) dependence of the apparent storage modulus (G_0') was measured from 0.1 to 100 rad/s over temperatures ranging from 303 to 153 K and strains ranging from 0.1 to 5% using an ARES-G2 rheometer (TA Instruments). Multiple measurements at different strains at a single temperature were performed to ensure a linear response. The time-temperature superposition principle was used to construct master curves of modulus versus

frequency with a reference temperature of 298 K using the Williams-Landel-Ferry (WLF) equation.

3.4 Results and discussion

Two series of bottlebrush elastomers with poly(dimethylsiloxane) (PDMS) side chains $n_{sc} = 14$ and 28, respectively, have been prepared by photo-initiated radical polymerization of monofunctional macromonomers in the presence of difunctional crosslinkers. All molecular characteristics are summarized in Table 3.1. The method developed here readily allows *one-step* preparation of different macroscopic shapes at a gel fraction >87%. Figure 3.1A displays stress-strain curves measured upon uniaxial extension of PDMS bottlebrush elastomers with $n_{sc} = 14$ (solid lines) and $n_{sc} = 28$ (long dashed lines). All curves display enhanced strain-stiffening behavior due to finite extensibility of the intrinsically extended bottlebrush strands. As anticipated, the networks with smaller n_x and larger n_{sc} display more pronounced non-linearity due to greater extension of the network strands ($\beta \sim \sqrt{n_{sc}} n_x^{-1}$). The stress-strain curves in Fig. 3.3A are fitted using Equation 3.1 with two fitting parameters introduced earlier: G and β (short dashed lines in Fig. 3.3A). Table 3.1 lists the regressed G and β values, as well as the apparent modulus (G_0) and elongation at break ($\lambda_{max,ex}$) measured experimentally at small and high strains, respectively. In Fig. 3.3B, the values of G and β extracted from Fig. 3.3A are plotted as a function of n_x^{-1} (an effective measure of crosslink density) and demonstrate excellent agreement with the scaling relationships provided in Equations 3.2 and 3.3. Such agreement highlights the reliability of both the bottlebrush architecture and synthetic methods used.

Table 3.1: Structural parameters and mechanical properties of bottlebrush samples

Sample	n_{sc}[a]	n_x[b]	$10^3\varphi_x$[c]	G (kPa)[d]	β[e]	G_0 (kPa)[f]	λ_{max}[g]	$\lambda_{max,ex}$[h]
Series 1	14	400	1.2	1.1±0.1	0.08±0.01	1.2	3.7±0.2	3.5±0.3
	14	200	2.5	2.8±0.1	0.11±0.01	3.3	3.0±0.2	2.9±0.2
	14	100	5.0	6.2±0.2	0.17±0.01	8.1	2.4±0.1	2.1±0.2
	14	67	7.4	10±0.4	0.23±0.01	15.0	2.1±0.1	1.9±0.2
	14	50	9.9	13.5±0.5	0.28±0.02	22.0	1.9±0.1	1.5±0.1
Series 2	28	200	2.5	1.1±0.1	0.23±0.01	1.5	2.1±0.1	2.4±0.1
	28	100	5.0	1.8±0.1	0.25±0.02	2.7	2.0±0.1	2.2±0.1
	28	67	7.4	2.0±0.1	0.3±0.02	3.4	1.8±0.1	1.9±0.1

[a]Degree of polymerization (DP) of the side chain. [b]Targeted DP of the backbone between crosslinks calculated from the mole fraction of the difunctional crosslinker as $n_x = 1/(2\varphi_x)$. Though the actual n_x values may be larger due to incomplete conversion of the cross-linker moieties, precise control of the crosslink density as linearly proportional to n_x^{-1} is accomplished (Fig. 3.3B). [c]Mole fraction of crosslinker used in the synthesis. [d]Structural shear modulus and [e]extension of network strands in as-prepared bottlebrush elastomers ($\beta = \langle R_{in}^2 \rangle / R_{max}^2$) determined by fitting stress-strain curves in Fig. 3.3A with Equation 3.1. [f]Apparent shear modulus measured as the slope $G_0 = d\sigma/d\lambda$ at small deformations ($\lambda \to 1$). [g]Maximum uniaxial extension calculated as $\sqrt{\beta^{-1}}$. [h]Experimentally measured elongation at break.

Taking a closer look at Figure 3.1A, it can be seen that all materials display relatively low moduli (1–10 kPa), relatively large extensions (up to 3.5), and enhanced strain stiffening response. Figure 3.1C displays a practical example of the combinations of low modulus and high β. Two polymer films are placed in a rigid ring clamp set up and coated on both sides with a conductive grease. When a voltage is applied the non-conducting PDMS films acts as capacitors and charge accumulates on the surfaces of the polymer film. Coulombic attraction compresses the films in the vertical direction forcing them to expand in the horizontal direction and thus bulge out from their rigid frames. In typical polymer materials there is a typing point called an electro mechanical instability (EMI). [99-101] As the voltage is raised the material is further compressed (thinned) until the elastic force of the polymer can no longer counter balance the coulombic attraction and the material is rapidly and often catastrophically compressed. Strong strain hardening behavior causes

increase in modulus with increasing deformation which increases the elastic force that the polymer film is able to output. This can allow samples to survive EMI or avoid EMI altogether. In the first case, a PDMS bottlebrush elastomer with a short side chain (n_{sc} = 14) and long strand (n_x = 200) exhibits EMI, which is evidenced by a drastic snap-through at a constant nominal electric field $\Phi/h_0 = 7.6$ Vμm^{-1}. Electroactuation is stabilized by the finite extensibility of the network strands. The second example considered here (without EMI) corresponds to an elastomer with longer side chains ($n_{sc} = 28$) and exhibits steady voltage-controlled electroactuation over the entire extension range until dielectric breakdown (destructive conduction through a non-conducting media) occurs at $\lambda_a^{BD} \cong 3.2$. In both instances, the experimental data points are consistent with theoretical predictions (solid lines in Figure 3.1C given as:

$$\frac{\Phi}{d_0} = (\varepsilon\varepsilon_0)^{-1/2}\sqrt{-\lambda^2\sigma_{true}(\lambda) - \frac{PR}{4d_0}\frac{1}{\sqrt{\lambda^{-1}-1}}} \qquad 3.4$$

where $\varepsilon_0 = 8.85 \cdot 10^{-12}\,\mathrm{F \cdot m^{-1}}$is the dielectric permittivity of vacuum, $\varepsilon = 2.94 \pm 0.02$ refers to the relative dielectric permittivity of the elastomer, $P = 5 \cdot 10^{-4}$ atm represents the blowing pressure to bias the actuation direction, and R = 5 mm is the radius of the DE membrane. In addition to governing the strain-stiffening behavior, the parameter β predicts the maximum extensibility of an ideal network as $\lambda_{max} \cong R_{max}/\sqrt{\langle R_{in}^2\rangle} \cong \sqrt{\beta^{-1}}$. As evidenced in Figure 3.1D and Table 3.1, the experimentally measured elongation at break ($\lambda_{max,ex}$) correlates reasonably well with the predicted λ_{max}.

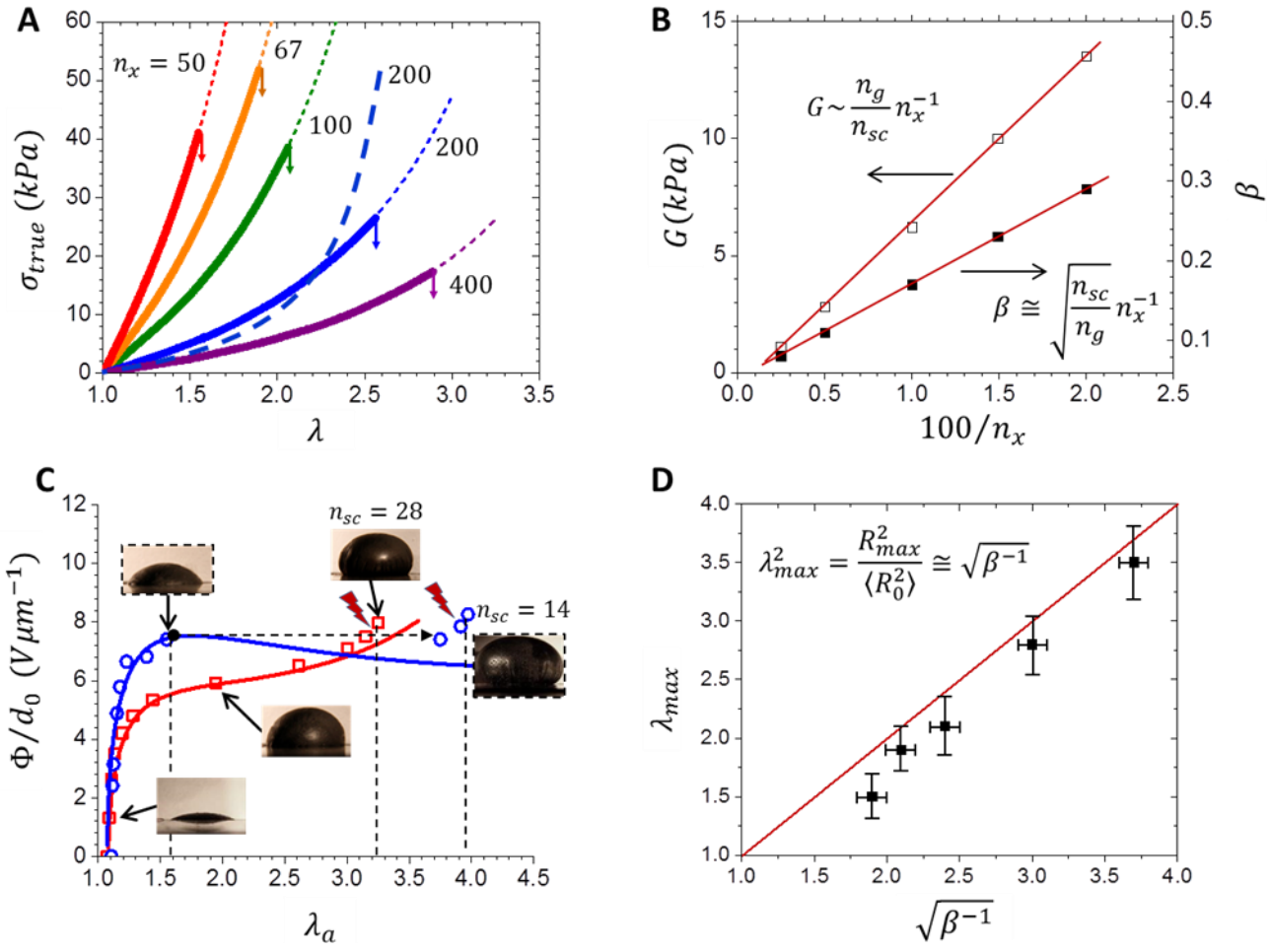

Figure 3.1: Mechancial response of dense bottlebrush elastomers. **A)** True stress is presented as a function of uniaxial extension upon tensile deformation of bottlebrush elastomers with different crosslink densities ($\sim n_x^{-1}$) and side-chain DPs ($\sim n_{sc}$). The solid and long dashed lines correspond to the sample series of samples with $n_{sc} = 14$ and 28, respectively. **B)** The shear modulus (G) and elongation ratio (β) extracted from fitting the stress-strain curves in A) with Equation 3.1 (short dashed lines) are plotted as a function of n_x^{-1}. In accord with theoretical predictions, both properties increase linearly with increasing crosslink density. From the corresponding slopes and the known values of $n_{sc} = 14$, $n_g = 1$, and $\rho = 7.7\ nm^{-3}$ for PDMS, we obtain the numerical prefactors $C_1 = 0.3$ and $C_2 = 3.1$. **C)** Electroactuation of two bottlebrush elastomers with the same network strand DP ($n_x = 200$) and two different side-chain DPs (n_{sc}): 14 and 28. The strong strain hardening behavior leads to stable actuation as evidenced by the sharp upturn in the data (hollow shapes). **D)** As expected from Equation 3.3, the maximum extension of the bottlebrush elastomers prepared here is linearly dependent on the strand extension $\sqrt{\beta^{-1}}$ in the as-prepared elastomers.

To display the unentangled nature and highly elastic behavior of PDMS bottlebrush elastomers, rheological master curves were produced for samples with $n_x = 50, 67, 100,$ and 200, $n_{sc} = 14$, and $n_g = 1$. Figure 3.2a displays the master curves of a PDMS bottlebrush exhibiting distinctly unentangled Rouse-like behavior prior to crosslinked modulus plateau and show onset of highly elastic behavior (vertical dotted lines between frequencies of ~30 s^{-1} ($n_x = 200$) and 1500 s^{-1} ($n_x = 50$) for all samples (effective strain rates of 170 and 5800 strain/s). The elastic response of bottlebrush elastomers was verified by the lack of hysteresis in tensile test (Figure 3.2b).

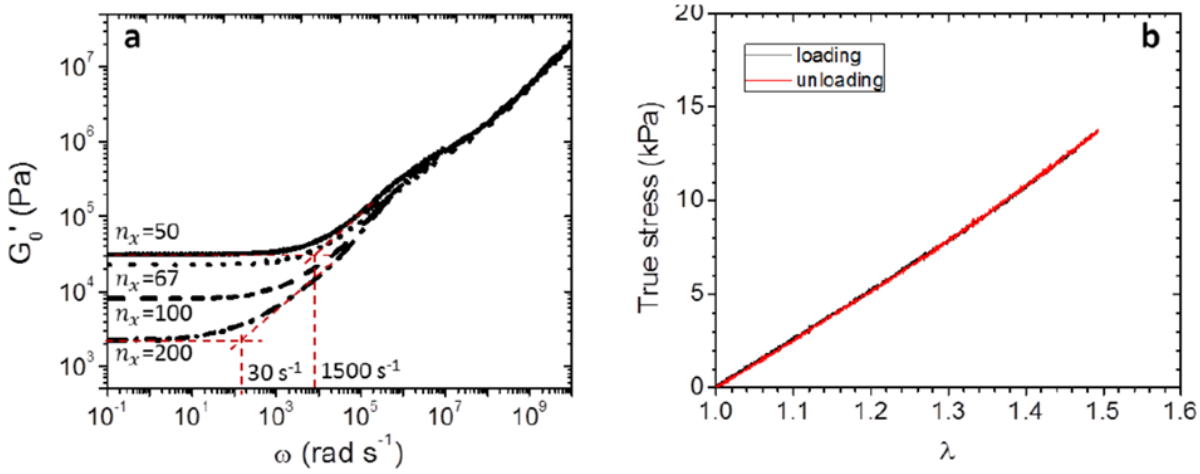

Figure 3.2: Elastic response. a) Master curves of the storage modulus of PDMS bottlebrush networks ($n_{sc} = 14$ and $n_g = 1$) with four different degrees of polymerization between crosslinks $n_x = 200$ (dash-dot line), 100 (dashed line), 67 (dashed line), and 50 (solid line), where $G_0' = (G'/3)(1 + 2(1 - \beta)^{-2}$- apparent storage modulus, G'- network storage modulus corresponds to n_x, and $\beta = \langle R_{in}^2 \rangle / R_{max}^2$- strand elongation ratio at rest in as prepared elastomers. The master curves display two major regions: (i) a Rouse-like relaxation of bottlebrush network strands and (ii) an elastic modulus plateau due to permanent stress storage of the covalently crosslinked network. For the networks possessing $n_x = 200$ and $n_x = 50$, the onset of the rubber plateau (vertical dotted lines) was observed at frequencies of ~30 s^{-1} and 1500 s^{-1}, respectively. Below these frequencies and strain rates, the corresponding elastomers demonstrate a largely elastic behavior. **b)** Stress-strain curves were measured during a loading-unloading tensile cycle of a PDMS bottlebrush elastomer ($n_{sc} = 14$ and $n_x = 100$) at a strain rate of 0.003 s^{-1}. The lack of hysteresis suggests elastic response in a broad deformation range.

3.5 Conclusion and outlook

In summary, we have developed a bottom-up synthetic strategy for producing moldable gram quantities of bottlebrush elastomer with well controlled architectural parameters. Both G and β scaled with molecular parameter as predicted indicating the success of the synthetic methods employed. The materials were analyzed using a superior method of characterizing strain that separates the properties due to crosslinking from the properties derived from strand stiffness. As was discussed in Chapter 1, the unentangled nature of bottlebrush molecules opens the path for considerable control of mechanical properties in elastomers. Applying this, we achieved elastomer modulus two orders of magnitude below that of linear materials and with extensibilities on par with linear materials. The unique preextended backbones in bottlebrushes allow for strong strain hardening behavior demonstrated in Figure 3.1A and the unusually high values of β. This effectively highlights another important aspect for the future of brush-like elastomers: tuned control of the pre-extension and strain hardening materials. The molecular design approach developed here is independent of chemistry and accesses new ranges of material properties from application specific chemistries. The fine control of mechanical properties combined with our realization of the importance of the strain hardening behavior of brush-like molecules is an important step forward in the full understanding of brush like architectures. As an example of possible applications the materials were applied to dielectric actuation. Brush-like control over strain hardening allowed for highly stable actuations which may prove key to the future of soft robotics.

CHAPTER 4: PHYSICAL NETWORKS AND GUIDED CRYSTALLIZATION[4]

4.1 Introduction and objectives

The previous chapter discuss the properties of dense bottlebrush elastomers and how the bottlebrush structure leads to disentangled network strands with strong strain hardening. Although covalent crosslinking offers numerous advantages, physical crosslinking opens a range of possible applications including recyclable networks, and shape memory. In this chapter we explore the effect of the bottlebrush structure on the formation of crystalline crosslinks. In order to create these network we turned to the ABA structure. Linear ABA block-copolymers are a valuable class of polymeric materials capable of self-assembling into physical networks through micro-phase separation of the dissimilar polymer blocks.[102-104] These linear networks are subject to intrinsic entanglements between their network strands, which set a lower limit for the elastic modulus. By replacing the linear B segments with bottlebrushes, the strands disentangle, opening an opportunity for the creation of supersoft, reversible polymeric networks. [97]

[4]This chapter previously appeared as an article in Macromolecules. The original citation is as follows: Daniel, W. F. M.; Xie, G.; Vatankhah-Varnoosfaderani, M; Burdyńska, J.; Li, Q.; Nykypanchuk, D.; Gang, O.; Matyjaszewski, K.; and Sheiko, S. S. Bottlebrush-Guided Polymer Crystallization Resulting in Supersoft and Reversibly Moldable Physical Networks *Macromolecules* **2017** *50* (5), 2103-2111.

Bottlebrush polymers are readily used as mesoscopic building blocks in the materials community and are comprised of three independently controlled structural parameters: the degree of polymerization (DP) of the backbone (n_{bb}), the DP of the well-defined pendent group side chains (n_{sc}), and the number of backbone monomers per side chain (n_g).[105-110] Because of the high density of large pendent groups, bottlebrushes display a combination of extended but still flexible backbone conformations and large effective molecular diameters leading to disentanglement of their melts.[80,81,97] By introducing crosslinks into bottlebrush melts one can create elastomers with exceedingly low moduli (down to the hundreds of Pa), while simultaneously allowing for high deformations and strong strain stiffening behavior.[27] Moreover, steric repulsion between the densely grafted side chains strongly influences phase separation behavior in ABA type materials and confines previously uncontrolled behaviors such as crystallization giving additional control over physical properties. This chapter considers crystallization of linear chain segments to physically crosslink bottlebrush polymers to create supersoft, dry elastomers with the potential to be remolded and recycled through the melting of temporary crystalline junctions. In order to create these semi-crystalline bottlebrush polymers, we turn to block copolymer bottlebrushes[111-120] specifically an ABA architecture (Figure 4.1) composed of a two crystallizable linear chain A blocks and an amorphous bottlebrush segment (B middle block). Unlike the linear ABA counterparts,[121-124] the bottlebrush block plays four distinct roles in controlling the network architecture formation. First, an increase in n_{sc} effectively reduces the crosslink density of the disentangled network strands. Second, the side chains enhance the bending rigidity of the network strands favoring bridges versus loops of the B blocks, and hence promotes network formation. Third, steric repulsion between the densely grafted side chains of the brush repel neighboring bottlebrushes, which in turn hinders crystallization of the linear A blocks leading to reduced

crosslink functionality, increased effective network strand length, and prevents crystal percolation. Fourth, the n_{sc} is a primary control parameter for tuning the mass fraction of the crystalline phase ($\varphi_{w,A}$) for a given DP of the A block as seen in Equation 4.1

$$\varphi_{w,A} \approx \frac{m_A n_A}{m_{BA} n_{bb}\left(n_{sc}/n_g\right) + \left(m_A n_A\right)} \approx \frac{m_A n_A}{m_{BA} n_{bb} n_{sc}} \sim \frac{1}{n_{sc}} \qquad 4.1$$

where m_{BA} and m_A are the monomer molar masses of BA side chains and the ODA-*stat*-DA A blocks, and n_A is the DP of the A block.

This work expanded on past experience [125, 126] and focus on the reversible network formation properties afforded by the combination of the ABA structure and the bottlebrush architecture. Depending on the DP of side chains, we anticipate three distinct scenarios for network formation: (i) short side chains (high fraction of the A blocks) will allow for unconstrained crystallization of the A blocks creating a hard crystalline scaffold effectively screening the mechanical properties of the bottlebrush B phase (Figure 4.1a), (ii) intermediate side chain sizes allow for strong phase separation into discreet A domains leading to soft percolated networks with reversible crystalline crosslinks embedded in a continuous amorphous phase (Figure 4.1b), and (iii) steric repulsion between long side chains hinder crystallization of the A blocks leading to a decrease of crosslink functionality and eventually to uncrosslinked melts of bottlebrushes (Figure 4.1c). Because the first scenario is well noted and considered trivial, we will focus on the second and third scenario and the effect of the side chains on the network formation of ABA bottlebrushes. Herein we present the synthesis, characterization, and preliminary thermomechanical exploration of semi-crystalline bottlebrush block copolymers. A series of bottlebrushes with A block tails of semi-crystalline poly(octadecyl acrylate-*stat*-docosyl acrylate) and central B blocks of amorphous

poly(*n*-butyl acrylate) bottlebrushes (poly[(ODA-*stat*-DA)-*b*-(BiBEM-*g*-*n*BA)-*b*-(ODA-*stat*-DA)]) were synthesized using ATRP[127,128] and then characterized for molecular and bulk network formation properties using DSC (differential scanning calorimetry), LB-AFM (Langmuir−Blodgett deposition Atomic-Force Microscopy), and shear rheology as a function of ODA-*stat*-DA content and bottlebrush molecular parameters.

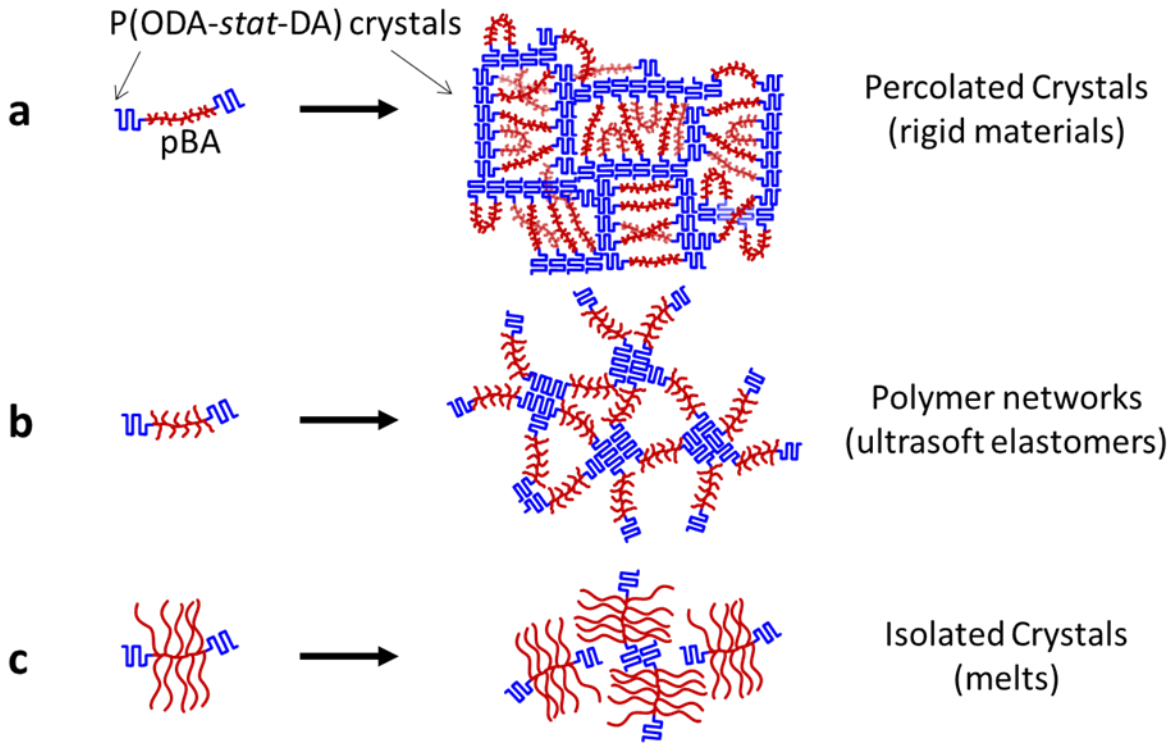

Figure 4.1: Representation of soft network formation in ABA bottlebrush polymers. **a)** Short side chains result in unconstrained crystallization leading to ridged crystal scaffolds. **b)** Intermediate side chains DPs result in association of neighboring A blocks, the formation of confined crystalline junctions, and soft bottlebrush networks. **c)** Large side chains prevent association of A blocks resulting in bottlebrush melts with isolated crystals.

4.2 Experimental section

4.2.1 Synthesis

The ABA samples in this chapter were produced via ATRP growth of bifunctional HEMA-TMS macro initiators. Subsequent reactions were used to grow two identical ODA-*stat*-DA A blocks at the ends of the macroinitiator and P*n*BA sidechains from the middle of the macroinitiator to form the bottlebrush B block. For full synthetic details see Daniel, W. F. M., et al. *Macromolecules* **2017** *50* (5), 2103-2111.

4.2.2 Size Exclusion Chromatography and Proton Nuclear Magnetic Resonance

The apparent number-average molecular weights ($M_{n,\,app}$) and dispersity (M_w/M_n) were measured by size exclusion chromatography (SEC). The SEC was conducted with a Waters 515 pump and Waters 2414 differential refractometer using PSS columns (SDV 10^5, 10^3, 500 Å) with THF as eluent at 35 °C and at a flow rate of 1 mL min^{-1}. Linear PMMA standards were used for calibration. Polymerization was monitored by ^{1}H NMR spectroscopy using a Bruker Advance 300 MHz NMR spectroscope with $CDCl_3$ as a solvent. Monomer conversion was calculated from the decrease of the monomer peak area relative to the peak areas of the internal standards. The molecular weights and dispersities can be seen for the macroinitiator (Table 4.1) ODA-*stat*-DA A block tails (Table 4.2) and final ABA molecules (Table 4.3).

Table 4.1: Experimental conditions and molecular parameters for the synthesis of P(HEMA-TMS).

Sample	[M]:[2f-BiB]:[CuBr]:[$CuBr_2$]:[dNbpy]	Solvent	Conv. [a]	$M_{n,app}$ [b]	M_w/M_n [b]
Poly(HEMA-TMS)$_{220}$	500:1:2:0.8:0.2:2	20%	43.9%	32,200	1.1
Poly(HEMA-TMS)$_{444}$	1000:1:0.8:0.2:2	20%	44.4%	62,800	1.09

[a] Conversion of HEMA-TMS measured by ^{1}H NMR; [b] Determined by SEC using linear PMMA standards.

Table 4.2: Experimental conditions and molecular parameters for the synthesis of ABA triblock macroinitiator.

Sample	Composition	[ODA]:[DA]:[poly(HEMA-TMS)]:[CuCl]:[$CuCl_2$]: [DOD-BPED*]	Solvent	Conv. [a]	$M_{n,app}$ [b]	M_w/M_n [b]
MI1	poly[(DA$_{50}$-*stat*-ODA$_{50}$)-*b*-BiBEM$_{220}$-*b*-(DA$_{50}$-*stat*-ODA$_{50}$)]	411:411:1:4.9:0.5:5.4	55%	24.3%	49,600	1.47
MI2	poly[(DA$_{105}$-*stat*-ODA$_{105}$)-*b*-BiBEM$_{220}$-*b*-(DA$_{105}$-*stat*-ODA$_{105}$)]	800:800:1:6.7:1.3:8	59%	26.2%	54,400	1.50
MI3	poly[(DA$_{122}$-*stat*-ODA$_{122}$)-*b*-BiBEM$_{444}$-*b*-(DA$_{122}$-*stat*-ODA$_{122}$)]	800:800:1:7:1:8	51%	30.4%	63,400	1.64

[a] Conversion of acrylate measured by ^{1}H NMR; [b] Determined by SEC using linear PMMA standards.

Table 4.3: Formulations used for the synthesis of ABA triblock brush.

Sample	Composition	[*n*BA]:[BiBEM]: [CuBr]:[$CuBr_2$]: [dNbpy]	Solvent	Conv. [a]
SC-23	poly[(DA_{50}-*stat*-ODA_{50})-*b*-(BiBEM-*g*-*n*BA_{23})$_{220}$-*b*-(DA_{50}-*stat*-ODA_{50})]	300:1:0.35:0.025:0.75	10%	7.6%
SC-34	poly[(DA_{50}-*stat*-ODA_{50})-*b*-(BiBEM-*g*-*n*BA_{34})$_{220}$-*b*-(DA_{50}-*stat*-ODA_{50})]	800:1:0.974:0.026:2	10%	4.3%
SC-44	poly[(DA_{50}-*stat*-ODA_{50})-*b*-(BiBEM-*g*-*n*BA_{44})$_{220}$-*b*-(DA_{50}-*stat*-ODA_{50})]	340:1:0.333:0.017:0.7	10%	12.9%
SC-110	poly[(DA_{50}-*stat*-ODA_{50})-*b*-(BiBEM-*g*-*n*BA_{110})$_{220}$-*b*-(DA_{50}-*stat*-ODA_{50})]	800:1:0.974:0.026:2	10%	13.8%
SC-67-n_ax2	poly[(DA_{105}-*stat*-ODA_{105})-*b*-(BiBEM-*g*-*n*BA_{67})$_{220}$-*b*-(DA_{105}-*stat*-ODA_{105})]	600:1:0.637:0.025:1.324	10%	11.2%
SC-60-n_ax2-n_{bb}x2	poly[(DA_{122}-*stat*-ODA_{122})-*b*-(BiBEM-*g*-*n*BA_{60})$_{444}$-*b*-(DA_{122}-*stat*-ODA_{122})]	610:1:0.737:0.025:1.524	10%	9.9%

[a] Conversion of acrylate measured by ^{1}H NMR.

4.2.3 Langmuir-Blodgett Deposition Atomic-Force Microscopy (LB-AFM)

Known volumes (30-100 μL) of bottlebrush polymer in chloroform solutions (0.03-0.06 mg/ml) were deposited dropwise onto the water air interface of a KSV 3000 series Langmuir Blodgett trough. The samples were then compressed at a rate of 20 mm/min until monolayer formation was observed. LB films were transferred onto cleaved mica substrates at a constant surface pressure of 0.5 mN/m and a controlled transfer ratio. AFM micrographs were taken in PeakForce QNM mode using a multimode AFM (Brüker) with a NanoScope V controller. Silicon probes were used with a resonance frequency of 50-90 Hz and a spring constant of ~0.4 N/m. In-house developed computer software was used to analyze the AFM images for length and width distributions. Collections of over 1000 molecules were analyzed to ensure standard deviations of the mean remained below 10%. Molecular weights of samples were then calculated by using the known mass of polymer deposited onto the trough surface and known trough surface area during

film transfer to find the mass per unit area. This was then combined with the known number of bottlebrush molecules per unit area taken from AFM micrographs to find the number average molecular weight. Thick films for AFM were produced from 10 mg/ml in chloroform solutions deposited in 0.2 ml aliquots onto cleaved mica surfaces. The films were allowed to dry in a closed Petri dish at room temperature before being imaged.

4.2.4 Differential Scanning Calorimetry (DSC)

The transition temperatures and heats of melting and crystallization were measured using a TA Q200 series DSC. Measurements were performed in a range of -100 to 100 °C using heating and cooling rates of 3 °C/min with samples sizes between 4 and 6 mg. The results are summarized in Table 4.5.

4.2.5 Small/wide angle x-ray scattering

Measurements were conducted at Brookhaven National Lab, Center for Functional Nanomaterials, using a Bruker Nanostar U instrument equipped with Vantec 2000 area detectors and Copper rotating anode as a source. Scattering patterns from the samples were measured at room temperature and collection time was set as 30s for all samples. A polynomial decay function with Savitzky-Golay filter was used for baseline fitting. After baseline subtraction, the peaks were fitted using Lorentz function.

4.2.6 Shear Rheology

Mechanical properties of the ABA bottlebrush triblock-copolymers were measured using an ARES-G2 shear rheometer from TA instruments with 8mm steel parallel plate geometries. For the stress relaxation curves, samples were loaded and their thermal histories were erased by

allowing all samples to sit at 70 °C for a period of 30 min before being compressed and trimmed into sample disks of 0.7 mm height by 8 mm diameter. The samples were then rapidly cooled to the experimental temperature, allowed to equilibrate at temperatures of 70 °C or 25 °C for 30 min, subjected to a 5% strain, and measured over period 3 to 24 hours to ensure stable stress values or complete relaxation to 0 Pa of stress. The thermal ramps were executed using an identical loading procedure to the one described above followed by equilibration at 70 °C. The samples were then subjected to 10% strain at a frequency of 1 rad/s while cooling down to 25 °C at a rate of 1 °C/min.

4.3 Results and discussion

The general synthetic procedure for the preparation of bottlebrush copolymers is shown in Scheme 4.1. Poly[(ODA-*stat*-DA)-*b*-(BiBEM-*g*-*n*BA)-*b*-(ODA-*stat*-DA)] brushes were synthesized by grafting *n*BA from poly[(ODA-*stat*-DA)-*b*-BiBEM-*b*-(ODA-*stat*-DA)] macroinitiator. The triblock backbone macroinitiator was synthesized via ATRP of HEMA-TMS using a difunctional initiator, followed by chain extension of ODA and DA from the resultant difunctional poly(HEMA-TMS)

Scheme 4.1: Synthesis of triblock molecular brushes.

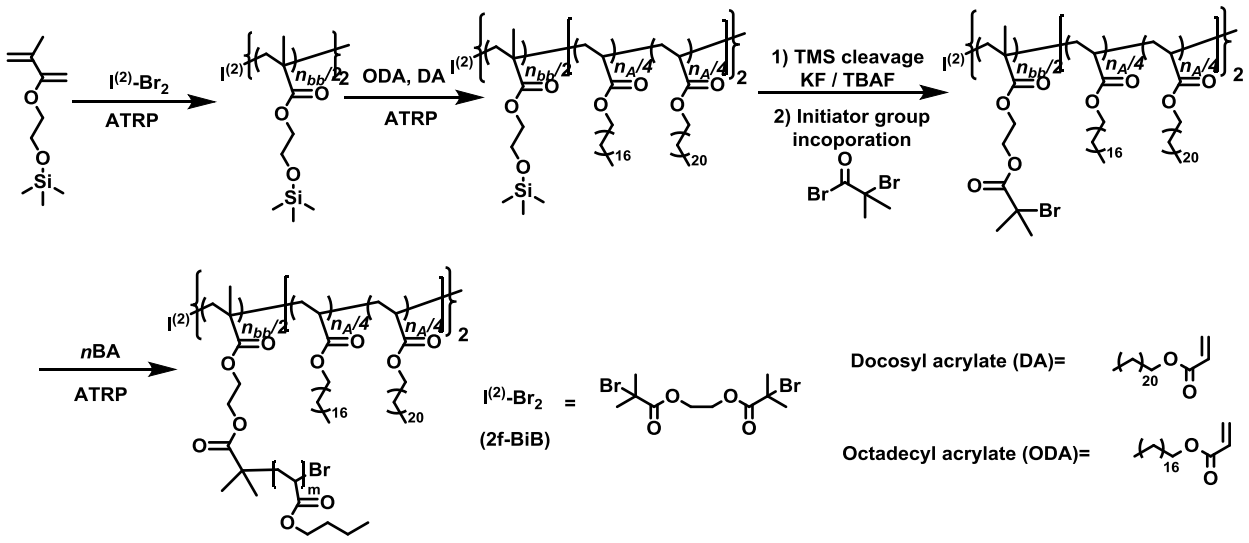

The structural parameters (n_{sc}, n_g, n_{bb}) of the bottlebrush B block (collectively called $n_B = n_{bb}(1 + n_{sc}/n_g)$) and DP of the crystalline A blocks (n_A) were precisely tuned by changing the initial monomer/initiator molar ratio and the final conversion of monomers in polymerization. ^{1}H NMR analysis combined with GPC was used to identity the targeted values of n_{sc}, n_{bb}, n_A, and molecular weight (M_w). The results of molecular characterization are summarized in Table 4.4. From SC-23 to SC-110, when the DP of side chain increases from 23 to 110, the weight fraction of crystallizable tails (ODA-*stat*-DA) correspondingly decreases from 9.0% to 2.2% (Table 4.5). The length of A block for SC-67- n_Ax2 is about twice as long as that for SC-34. Therefore, in order to have similar weight fraction of crystallizable side blocks, the DP of side chains for SC-67-n_Ax2 is almost twice as large as SC-34. Also, although having similar length of side chain and side blocks as SC-67- n_Ax2, SC-60-n_Ax2-n_{bb}x2 has significantly lower weight fraction of crystallizable blocks due to its much longer central block.

Table 4.4: Structural parameters and LB-AFM size analysis of Triblock bottlebrush polymers.

Sample	$n_{sc,}$ [a] target	$n_{bb,}$ [b] target	$n_{A,}$ [c] target	$n_{bb,}$ [d] AFM	$n_{B,}$ [e] target	L [f]	W [g]	$\varphi_{w,A}$ [h] DSC	M_n [i] GPC	M_n [j] AFM	M_n [k] target
Units						nm	nm		10^6	10^6	10^6
SC-23	23	222	2×100	224±3	5300	53.0±0.4	23.9±0.2	0.09	0.15	0.7	0.8
SC-34	34	222	2×100	224±3	7800	54.8±0.5	37.0±0.2	0.07	0.24	2.3	1.0
SC-44	44	222	2×100	224±3	10000	57.0±0.5	55.9±0.5	0.05	0.36	1.8	1.3
SC-110	110	222	2×100	224±3	25000	59.2±0.6	89.1±0.6	0.02	0.50	2.7	3.3
Increase of the crystalline block length (n_A)											
SC-67-n_Ax2	67	222	2*210	241±17	15000	64.5±0.7	71.0±0.3	0.08	0.41	3.0	2.1
Increase of both brush (n_{bb}) and linear (crystalline) (n_A) segments											
SC-60-n_Ax2-n_{bb}x2	60	444	2*243	408±4	27000	102.4±0.9	68.9±0.3	0.04	0.39	3.4	3.6

[a] Targeted DP of the side chains. [b] Targeted DP of the bottlebrush backbone. [c] Targeted DP of the semi-crystalline tails. [d] The DP of the bottlebrush backbone was determined as L/l_0 where l_0- monomer length. [e] Targeted DP of the amorphous center B block. [f] Length of the amorphous B block as measured from AFM micrographs. [g] Width of the bottlebrush B block as determined from AFM micrographs. [h] Weight fraction of ODA-*stat*-DA taken from targeted DPs of n_{sc} and n_A and measured values of n_{bb} calculated as Equation 4.1. [i] Number average molecular weight as determined by gel permeation chromatography. [j] Number average molecular weight as determined by the LB-AFM technique. [k] Number average molecular weight as calculated from targeted DPs of the bottlebrush samples.

In addition, molecular imaging by AFM was employed to find the length (L), and 2D width (W) distributions, and true molecular weights of the samples (Figure 4.2 and Table 4.4). These experiments display excellent agreement between the measured lengths (L) (calculated n_{bb}) and the targeted n_{bb}, as well as good agreement between the targeted values of n_{sc} and the widths (W) which are expected to scale as $n_{sc} = n_{sc,w}/Đ_X \sim W/Đ_X$ where $n_{sc,w}$- the weight average DP of the side chains and $Đ_X$ - the dispersity of the side chains (Figure 4.3).[129] Bottlebrush molecules

possess large molecular dimensions which can be readily resolved by AFM to find the accurate number of molecules per unit area in dense LB monolayers (Figure 4.2b). Combining this knowledge with the known mass of polymer deposited on the known area of the LB trough allows for the accurate determination of number average molecular weight ($M_{n,AFM}$). These MW values obtained from the LB-AFM analysis compare favorably with the targeted molecular weights (Table 4.4).

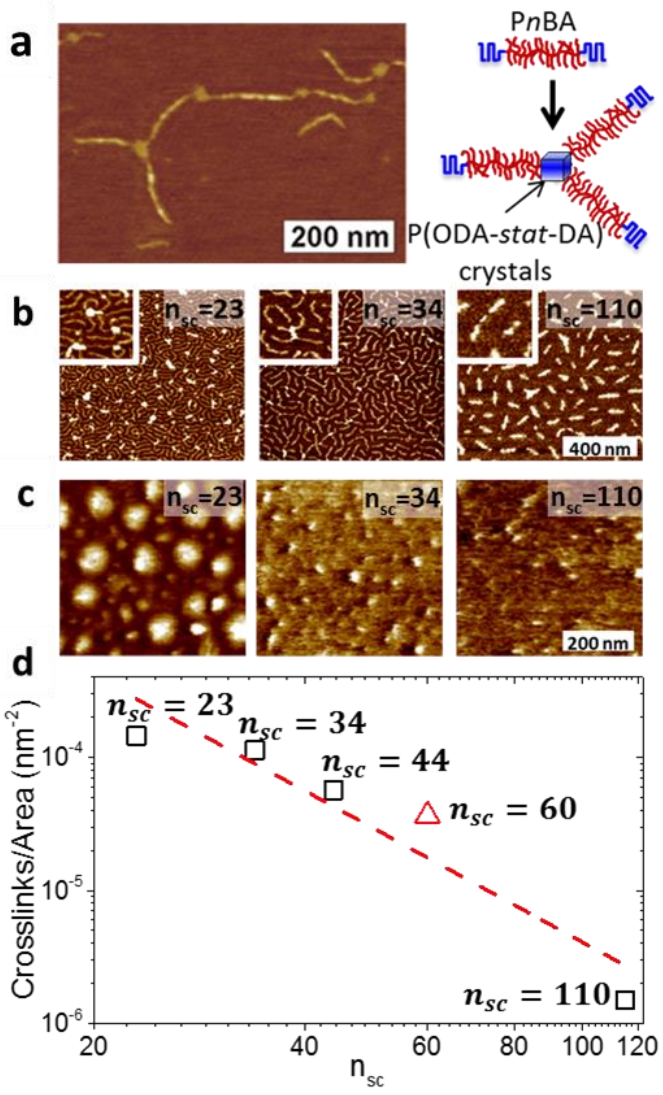

Figure 4.2: AFM of 2D crystallized bottlebrush copolymers. **a)** AFM height micrographs of single ABA bottlebrush macromolecules linked by crystalline junctions of the poly(ODA-*stat*-DA) linear tails (A block). **b)** AFM height micrographs of LB monolayers of ABA bottlebrush copolymers with varying side chain lengths. Inset images represent close-ups of crystalline junctions. **c)** Side by side AFM micrograph of a thick films of the corresponding ABA copolymers at room temperature. The crystalline domains appear as bright patches. **d)** Number of crystalline junctions connecting at least two bottlebrushes decreases with n_{sc}. Black squares (□) represent samples with n_{bb} and n_A of 224 and 2×100 respectively, and the red triangle (△) represents a sample with n_{bb} and n_A of 408 and 2×243 respectively

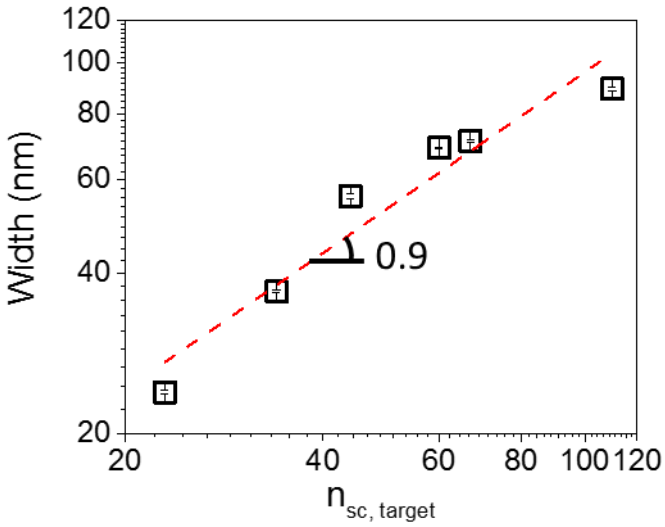

Figure 4.3: Width analysis. Scaling between 2D molecular width and n_{sc} shows close to linear relation. Error was calculated as the standard error of the mean of ensembles of over 100 molecular width measurements per sample.

Beside the MWD analysis, molecular imaging by AFM was also used to qualitatively verify network formation due to crystallization of the A tail blocks. For this purpose, we have prepared samples with different surface coverages including single molecules (Figure 4.2a), dense monolayers (Figure 4.2b), and thick films (Figure 4.2c). Samples of single molecules prepared by spin-casting from a dilute solution clearly display end-chain association of bottlebrush blocks (Figure 4.2a). The dense monolayers display large numbers of crystalline junctions which decrease with increasing n_{sc} and decreasing $\varphi_{w,A}$ (Equation 4.1), as is clearly seen in Figure 4.2b. Sample SC-23 displays a seemingly percolated network of crystalline junctions while samples SC-110 shows isolated crystals with few junctions. To reduce the effect of the substrate and approach the bulk morphology, thick films of samples SC-23, SC-44, and SC-110 were generated by drop casting from chloroform solutions (Figure 4.2c). Sample SC-23 with the shortest side chains displays large and numerous crystalline domains. Despite the apparently high fraction of the crystallites, they do not seem to merge or percolate as sketched in Figure 4.1b. SC-44 displays a

similar density of crystallites, but with smaller domains and as such larger inter-crosslink distances suggesting a softer network. In contrast the SC-110 film on the right displays only small areas of crystalline A phase and likely represents the third scenario in Figure 4.1c, where long side chains prevent association of A blocks, resulting in low crosslinking instances and failure of network formation. Even though, the 2-D images do not represent the true bulk organization of ABA networks and are strictly qualitative proof of network formation, we have plotted the areal density of the crosslink junctions versus DP of the side chains (Figure 4.2d), which shows a progressive decrease of the number of junctions per unit area of the ABA monolayers. This observation is attributed to the enhancement of steric repulsion with the side chain length, which hinders the association of the A blocks.

From AFM, it can be seen that the DP of the side chains plays a strong role in the formation of intermolecular crystallization and thus the potential crosslinking of bulk networks. While AFM gives a qualitative measure of inter-brush crystallization, it is also necessary to quantify the total crystallinity of the samples, i.e. both intermolecular (crosslinking) and intramolecular (non-crosslinking). In order to quantify the true crystallinity of the samples the degree of crystallization was measured by DSC as a function $\varphi_{w,A}$, which is directly related to the side chain DP as $\varphi_{w,A} \sim 1/n_{sc}$ (Equation 4.1). Figure 4.4a displays a representative DSC curve of sample SC-60-n_Ax2-n_{bb}x2. Despite the relatively low amount of crystalline material the sample displays a very clear crystallization and melting transitions. The values of the melting temperature T_m ranged from 53 to 55 ˚C which matches well with the measured value for free ODA-*stat*-DA chains with DP = 103 (53 ˚C). The DSC analysis is summarized in Table 4.5. Figure 4.4b displays the relative heats of melting versus the calculated weight fraction of ODA-*stat*-DA and shows a linear relation. The close match between DSC and synthetic estimations of $\varphi_{w,A}$ is strong evidence for the accurate

control of the targeted molecular parameters and gives evidence that the n_{sc} plays a strong role in regulating network formation without preventing intramolecular crystallization, i.e. the close match between the calculated values $\varphi_{w,A}$ and those values measured from DSC show that all samples fully crystalize, but only those with shorter side chains can form intermolecular junctions and networks. The temperatures of melting (T_m) group nicely between samples, however, there is an increase in the T_m for the SC-23 and SC-34. It may indicate formation of larger crystals due to the weaker effect of the shorter side chains on the crystallization of the A tails.

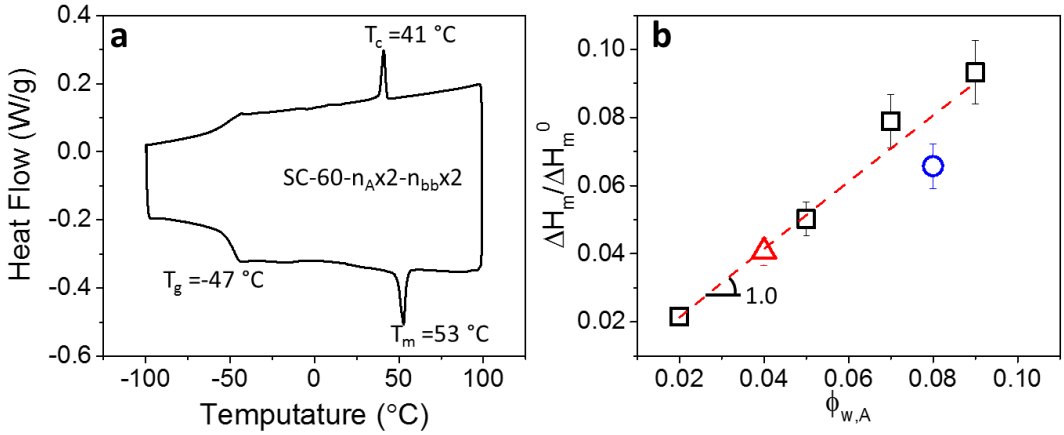

Figure 4.4: DSC of bottlebrush copolymer samples. **a)** a representative DSC curve for sample SC-60-n_Ax2-n_{bb}x2 displaying freezing peak, melting peak, and glass transition. **b)** Relative heats of melting as $\Delta H_m/\Delta H_m^0$, where ΔH_m^0 is the heat of melting for ODA-*stat*-DA (84 J/g). The values display a nearly linear relation with the targeted weight fraction of ODA-*stat*-DA. Black squares (□) represent samples with n_{bb} and n_A of 224 and 2×100 respectively and differing side chain lengths (SC-23, 24, 44, 110). The red triangle (△) represents a sample with n_{bb} and n_A of 408 and 2×243 respectively (SC-60-n_Ax2-n_{bb}x2). The blue circle (○) represents a sample with n_{bb} and n_A of 241 and 2×210 respectively (SC-67-n_Ax2).

Table 4.5: Thermal parameters of the bottlebrush samples from DSC and apparent shear moduli.

Sample	$\varphi_{w,A}$ [a] target	$\varphi_{w,A}$ [b] DSC	T_m [c] DSC	T_c [d] DSC	T_g [e] DSC	ΔH_m [f]	ΔH_c [g]	G_0 [h]
Units			°C	°C	°C	J/g	J/g	Pa
SC-23	0.09	0.09	55	41	-47	7.8	8.5	13000
SC-34	0.07	0.08	55	41	-47	6.6	7.3	5000
SC-44	0.05	0.05	53	41	-47	4.2	5.3	1900
SC-110	0.02	0.02	53	42	-49	1.8	2.1	0
SC-60-n_Ax2-n_{bb}x2	0.04	0.04	53	41	-47	3.4	4.0	NA
SC-67-n_Ax2	0.08	0.07	53	41	-49	5.5	6.1	2900

[a] Weight fraction of ODA-*stat*-DA taken from targeted DPs of n_{sc} and n_A and measured values of n_{bb} (see Table 4.4) calculated as Equation 4.1. [b] Weight fraction ODA-*stat*-DA taken from the ratio of $\Delta H_m/\Delta H_m^0$ where $\Delta H_m^0 = 84$ J/g is the heat of melting of in house synthesized free ODA-*stat*-DA tails. [c] Temperatures of melting from DSC curves. [d] Temperatures of crystallization from DSC curves. [e] Glass transition temperature taken from the middle of the heating transition from the DSC curves. [f] Heats of melting calculated from area under the melting peak of the DSC curves. [g] Heats of crystallization calculated from area under the crystallization peak of DSC curve. [h] The apparent shear modulus of the crystallized sample taken from stress relaxations after 3 hours relaxation at 25 °C. X-ray scattering was also employed to characterize the crystallinity of the samples. A characteristic peak located at q= 1.53 (Å^{-1}) was found for three samples :74, 79, and 83. This peak corresponds to a crystalline lattice with a dimension L=$2\pi/q = 4.1$ Å, which has been proven to be a paraffin-like hexagonal packing lattice of poly(n-acrylate) chains.[130,131] The more crystalline a sample is, the higher the intensity is at this peak. For the amorphous sample 78, it didn't show this characteristic peak, meaning the extinction of poly(n-acrylate) crystals. See Figure 4.5.

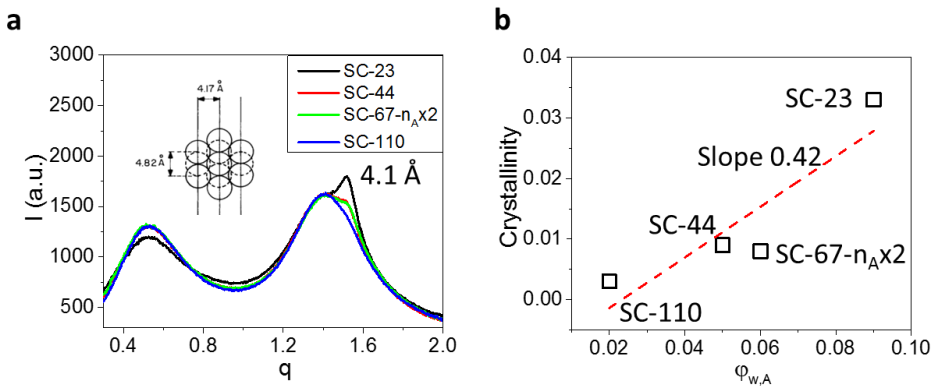

Figure 4.5: X-ray. **a)** Select samples SC-110, 44, 23, and SC-67-n_Ax2 display characteristic peak at 4.1 Å consistent with spacing of hexagonally packed acrylate chains. SC-23 possessing the highest fraction of ODA-*stat*-DA shows the strongest signal in contrast with SC-110 possessing the least crystalline material and showing almost no peak. **b)** Crystallinity as calculated from x-ray data shows a trend with $\boldsymbol{\varphi_{w,A}}$ of 0.4 qualitatively indicating that half of the ODA-*stat*-DA is in a crystalline state.

With the successful verification of molecular association and crystallization of the ABA bottlebrush copolymers, the network formation properties were assessed using shear rheology. To prove the formation of networks, samples with different side chain DPs were subjected to stress relaxation experiments at both 25 °C (well below the crystallization temperature of 41 °C seen in Table 4.5) and above the melting temperature at 70 °C. All samples were allowed to crystalize and melt at their respective experimental temperatures for a period of 30 min to ensure consistent network formation conditions. Figure 4.6a,b show stress relaxations of the bottlebrush copolymers measured below and above the crystallization and melting temperatures, respectively. At 25 °C (Figure 4.6a) the polymers displays constant network modulus after a brief period of Rouse-like and transition regime relaxations (figure inset displaying slope near -0.5 and below). The apparent shear modulus of the network (G_0) decreases with increasing n_{sc} and decreasing $\varphi_{w,A}$ displaying a relatively high modulus in the 10^4 Pa range for SC-23 and dropping down to zero network modulus for SC-110. It should be noted that sample SC-110 still displays obvious crystallization

transitions in DSC measurements but no network formation which is likely due to side chain steric hindrance preventing contact between the crystalline tails of neighboring molecules. When taken above the melting temperature all samples decay to a modulus of zero within a relatively short time span displaying the lack of any permanent crosslinking mechanisms within the samples.

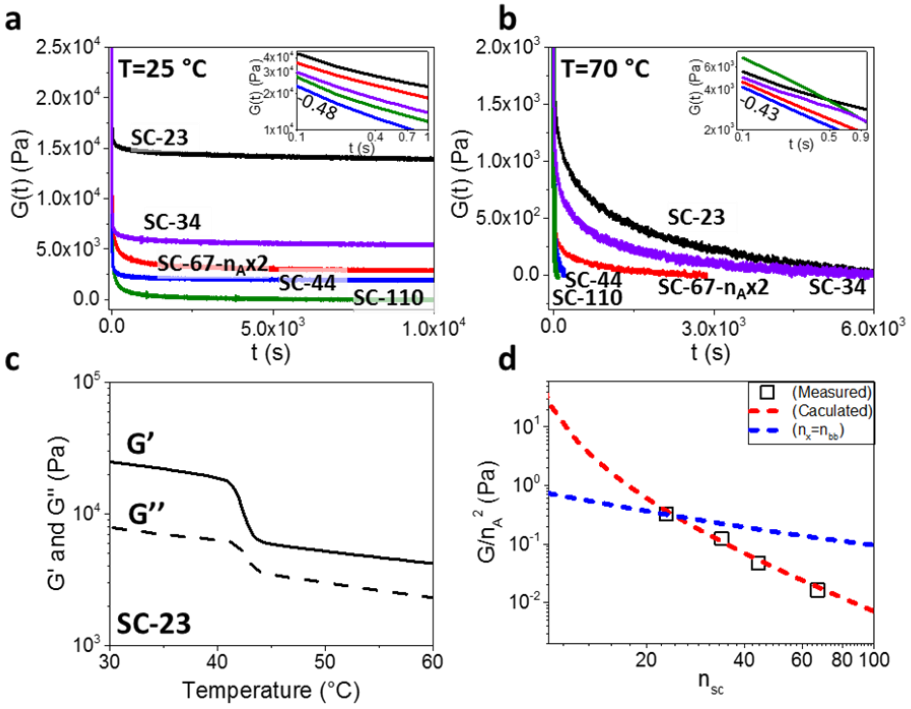

Figure 4.6: Rheological characterization of select bottlebrush copolymers. **a)** Shear relaxation modulus, $G_0(t)$, as a function of time at 25 °C (below T_c) of samples SC-23 (Black), SC-34 (Purple), SC-67-n_Ax2 (Red), SC-44 (Blue), SC-110 (Green) displays fast relaxation (inset) followed by plateaus at 13000 Pa, 5000 Pa, 2900, Pa, 1900, Pa, and 0 Pa, respectively. This indicates the presence of physically crosslinked networks. Inset: log-log plot of $G_0(t)$ at short times shows a power-law relaxation $G_0(t) \sim t^{0.42 \pm 0.06}$ consistent with the Rouse-like behavior. **b)** The relaxation modulus, $G_0(t)$, of the same samples as a function of time at 70 °C (above T_m). The curves display rapid relaxation to zero value indicating lack of network formation. **c)** Oscillatory storage and loss moduli (G' and G'') of sample SC-23 (1 rad/s, 5% strain) display sharp increases at the crystallization temperature of T=41°C. **d)** The data points (□) correspond to the normalized apparent relaxation modulus $G_0/{n_A}^2$ taken from (a) at $t = 3h$ decreases with the DP of the side chains (n_{sc}). Note that SC-110 does not form network ($G = 0$). The blue dashed line represents the expected trend in $G_0/{n_A}^2$ when $n_x = n_{bb}$ taken from Equation 4.2 substituting Equation 4.3 and 4.4. As can be seen, the networks display a stronger dependence on n_{sc} than expected. The red dashed line represents the fit of the experimental $G_0/{n_A}^2$ taken from Equation 4.2 substituting Equation 4 and 6 assuming that the crosslink density decreases with increasing n_{sc}.

Figure 4.6c displays a freezing transition for sample SC-23. There is a sharp increase in both the loss and storage modulus between 44 and 41 °C indicative of a crystallization transition and showing a relatively small change resulting in a crosslinked modulus on the order of 0.02 MPa. From the data in Figure 4.6a,b, it can be seen that this polymer architecture is capable of creating stable, but reversible physical networks with moduli below 0.1 MPa. The equilibrium apparent modulus normalized by the DP of the crystalline segments ($G_0/{n_A}^2$) were then plotted against their respective n_{sc} values (□ Figure 4.6d). Note that the modulus of bottlebrush networks (even when measured at small strains $\varepsilon \to 0$) is affected by strain-stiffening due to extended conformation of backbones in the bottlebrush strands. Due to finite extensibility of the backbone this so-called apparent modulus is higher than the structural modulus and described by the Dobrynin equation:[98]

$$G_0 = \frac{G}{3}(1 + 2(1-\beta)^{-2}) \tag{4.2}$$

where G is the structural modulus determined by the crosslink density and $\beta = \langle R_{in}^2 \rangle / R_{max}^2$ is the strand elongation ratio defined as the ratio of the mean square end-to-end distance of a network strand in the as prepared elastomer ($\langle R_{in}^2 \rangle$) and the square of the strand contour length (${R_{max}}^2$). For bottlebrush networks, the structural modulus and the strand elongation ratio depend on the architectural parameters as

$$G \cong \frac{\rho RT}{m_{BA}\, n_x \left(n_{sc}/n_g + 1\right)}(1 + \varphi_w) \cong \frac{\rho RT}{m_{BA}\, n_B}(1 + \varphi_w) \tag{4.3}$$

$$\beta \cong \left(\frac{n_{sc}}{n_g} + 1\right)^{1/2} n_x^{-1} \tag{4.4}$$

where ρ-mass density of the polymer, RT - the molar thermal energy, m_{BA}- molar mass of the amorphous monomer. In this model, the A blocks act simply as crosslinkers and each ABA molecule is assumed to span two multifunctional A block junctions making $n_x = n_{bb}$. An estimation for this trend can be seen in Figure 4d as the blue dashed line representing ${G_0}/{{n_A}^2}$ from Equation 4.2 substituting Equation 4.3 and 4.4. It became obvious that the materials possessed a much stronger dependence for both G_0 and β, which is ascribed to a decrease of the crosslink density due to increase of the side chain length. As discussed in the introduction (Figure 4.1), stronger steric repulsion between longer side chains hinder association of A tails from neighboring ABA bottlebrushes. This in turn effectively leads to a decrease in the crosslink functionality and an increase in the average network strand length. Strong evidence of this phenomenon can be seen in Figure 4.2b,c and Figure 4.6a where sample SC-110 displays small disconnected crystallite in monolayer films, sparse crystalline junctions in bulk films, and no network modulus below the sample T_m. New equations assuming that the strand length increase with n_{sc} as $n_x \approx {n_{sc}}/{n_A}$ were derived as

$$G \cong \frac{\rho RT}{m_0}\left(\frac{m_A}{m_0 n_{bb}}\frac{{n_A}^2}{{n_{sc}}^3}+\frac{n_A}{{n_{sc}}^2}\right)\sim\frac{{n_A}^2}{{n_{sc}}^3} \tag{4.5}$$

$$\beta \cong \frac{v^{\frac{1}{2}}}{l^{\frac{3}{2}}}\frac{n_A}{n_{sc}^{0.5}} \tag{4.6}$$

These equations account for the change in n_x as n_{sc} ($\varphi_{w,A}$) changes as well as an increase in the expected values of β due to repulsion between phase-separated components of the bottlebrush copolymers causing extended backbone conformations. The final expression in Equation 4.2 substituting Equation 4.5 and 4.6 accurately follows the experimental trend (red dashed line Figure

4.6d). The data presented gives strong evidence that the crosslinking of these bottlebrush copolymers are influenced by the steric repulsion created by the side chains near the crystalline tails as seen by the absence of modulus in in SC-110 despite its crystallization and the fitting of the data assuming that $n_x \sim n_{sc}/n_A$.

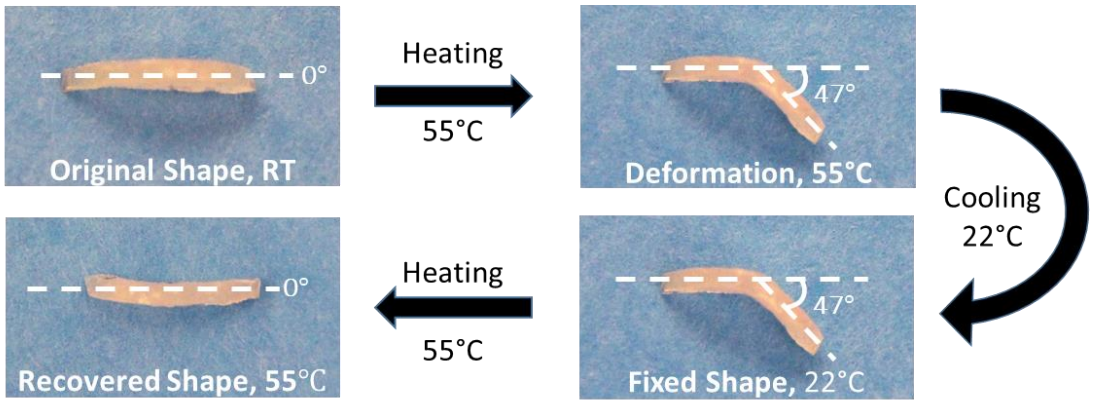

Figure 4.7: Supersoft shape memory. A shape memory cycle whereby a rectangular rod of thermally crosslinked SC-23 polymer is bent to a 47 degree angle at an elevated temperature of 55°C (above ODA melting) and then subsequently fixed by quenching to 22°C. Upon heating to 55°C, the sample recovers to its original rod-like shape.

Having demonstrated the ability of these materials to form supersoft physical networks through we moved onto the next logical step which was to test this system for potential shape memory behavior. The shape memory effect uses a weak permanent network to inforce an original shape. An external stress is applied to deform the sample into a programmed shape and temporary crosslinking elements such a crystallites are then introduced to create a stronger network to pin the programmed shape in place. Subsequent removal of the temporary crosslinking elements such as by heating allow the weaker permanent network to reassert itself and the permanent shape to reform. Figure 4.7 illustrates a shape memory experiment in which the sample of SC-23 was specially prepared with excess bromines at the end of its side chains and crosslinked by thermal

cleavage of the bromine carbon bonds followed by radical attack on nearby polymer chains. This resulted in a chemical network with modulus on the order of 200 Pa. The sample was bent to a 47 degree angle at 55˚C, then fixed by quenching to 22˚C, and subsequently returned to its original shape upon heating to 55˚C. This shape memory behavior give evidence that such systems will be suited to future applications as shape-memory biomedical implants where both the crystalline and amorphous moduli matching that of surrounding tissue.

4.4 Conclusion and outlook

In summary, a series of ABA tri-block copolymers with semi-crystalline tails and central amorphous bottlebrush blocks was synthesized. The materials were characterized by a variety of techniques to confirm their structural parameters. All of the samples display crystallization of the poly(ODA-*stat*-DA) tails, resulting in the formation of physical networks. The bottlebrush architecture plays a dual role in determining the mechanical properties of these networks. First, steric repulsion between the densely grafted side chains facilitates disentanglement of the network strands eliminating the typical lower limits for network modulus. Second, the same repulsion confines the crystallization process preventing percolations of a crystalline scaffold. This absence of entanglements pared with controlled crystallization allows for the formation of remoldable physical networks with supersoft moduli orders of magnitude below both typical semi-crystalline networks and amorphous elastomers. The apparent shear modulus G_0 of these networks decays with n_{sc} until the absence of network formation when the n_{sc} becomes comparable to n_a effectively isolating the A blocks and preventing crosslinking. Contrary to our original assumption, we discovered the system is best modeled by postulating that the n_x is controlled by changing n_{sc} rather than simply being determined by n_{bb} as would be the case in an ideal and fully

crosslinked system. The ability of the bottlebrushes to prevent percolation of crystallites and control crosslinking density in these physical networks by tuning architectural parameters enables the creation of supersoft elastomers with the capacity for reversible remolding and shape memory. In the broader context of this dissertation, the architectural control of brush-like polymer over micro-phase separation and the effects of that phase is yet another tool in the brush-like tool box. Such manipulation serves alongside the architectural control already displayed to open new limits of mechanical properties and new property trends. The next chapter discusses the final inherent control parameter of the brush-like paradigm, however, the future of advanced property control will undoubtedly build off of the interactions between architecture and chemistry as displayed here.

CHAPTER 5: GRAFTING DENSITY AND NEW PROPERTY TRENDS

5.1 Introduction and objectives

Chapters 1 and 3 discussed the mathematical link between side chains and the entanglement of a bottlebrush melt as well as the effect bottlebrush architecture and crosslinking on the strain hardening. These experimentally verified relations reviled two of the fundamental differences between brush-like architectures and linear polymers namely their highly disentangled nature and their pre-extended backbones leading to strong strain hardening. So far only two of the brush-like structural parameters have been manipulated (the network strand DP - n_x and the side chain DP - n_{sc}) leading to properties that are that are in unprecedented ranges for dry linear materials. Despite these advances, the materials described above were still beholden to traditional property relations such as the general inverse relation between modulus and extensibility. This chapter explores the effect of changing the final basic structural parameter (side chains per network strand monomer - n_g) on the properties of brush-like systems and how such structural manipulation opens unique trends in mechanical properties.

Figure 5.1a compares the deformation behavior of brush-like and linear-chain elastomers in terms of rigidity (E) and extensibility (λ_{max}). In conventional linear-chain elastomers, the degree of polymerization of the network strand (n_x) single-handedly determines both $E \sim n_x^{-1}$ and $\lambda_{max} \sim \sqrt{n_x}$; given in the full as

$$E \approx \frac{k_B T \rho}{n_x} \tag{5.1}$$

$$\lambda_{max} = \frac{R_{max}}{\langle R_{in}^2 \rangle^{1/2}} = \frac{l n_x}{\sqrt{b_k l n_x}} \approx n_x^{-\frac{1}{2}} \tag{5.2}$$

Thus, a universal relationship follows: $E \sim \lambda_{max}^{-2}$, whereby more rigid materials are less deformable (solid black line Figure 5.1a). This "*Golden Rule*" of Materials Science confines the vast majority of linear-chain mechanical behaviors to a single trend line bounded by inherent chain entanglements at $E \cong 10^5\ Pa$ and $\lambda_{max} \cong 5$ (hollow circle, Figure 5.1a)[97,132]. The relation exists in a nearly all engineering materials as shown in Figure 5.1b, and represents one of the fundamental limitations of materials design. A rich parameter space exists beneath this line, inhabited by strain-adaptive biological materials that are moderately extendable yet extremely soft and tough.[28] Using brush-like architectures, we open a wide variety of new property relations represented by number trend lines (i-iv) in Figure 5.1a, and create new materials capable of accessing properties previously only seen in biology. In this chapter we look at the preliminary results in exploring the new material property trends as well as discuss the future of studies in brush-like architectures.

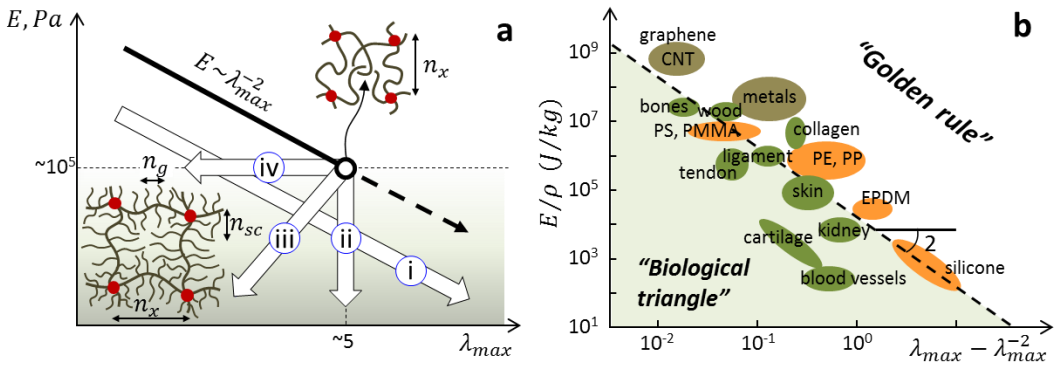

Figure 5.1: Breaking the "Golden Rule" to empower novel mechanical relations. (**a**) Conventional linear-chain elastomers exhibit, as $E \sim \lambda_{max}^{-2}$ (upper solid line), a locked inverse relationship between extensibility (elongation-at-break, λ_{max}) and rigidity (modulus, E), limited by chain entanglements to a lower $E \sim 10^5 Pa$ and an upper $\lambda_{max} \sim 5$ (hollow circle). However, the addition of two independent structural handles – n_{sc} and n_g – removes these limits, unlocks the relationship, and allows for orthogonal and single-variable control of E and λ_{max} (white arrows i-iv). (**b**) Arising from a general conjecture that materials absorb a certain density of mechanical energy ($E\varepsilon^2 \approx constant$) prior to fracture, the $E \sim \lambda_{max}^{-2}$ correlation characterizes a wide variety of materials and represents a "*Golden Rule*" of materials science: "more rigid means less extensible." Most notable deviations from this rule are embodied by mechanically-adaptive biological materials that exhibit relatively low moduli at a given moderate extensibility. Mapping the space unlocked by the $[n_{sc}, n_g, n_x]$ triplet with brush-like PDMS elastomers enables mimics of these desirable deviations and reveals.

5.2 Experimental section

5.2.1 Synthesis

The materials produced in this chapter were made using methodologies similar to those in Chapter 3. An AFM example of the uncrosslinked molecules is displayed in Figure 5.2 displaying the successful creation of long branched structures. Comb-like polymers were produced by the addition of a small molecule as diluent for the incorporation of the side chains as is shown in Figure 5.3. The quality of the synthetic methods used can be seen in Table 5.1, where examples of

uncrosslinked molecules display strong agreement between ^{1}H NMR analysis and LB-AFM analysis.

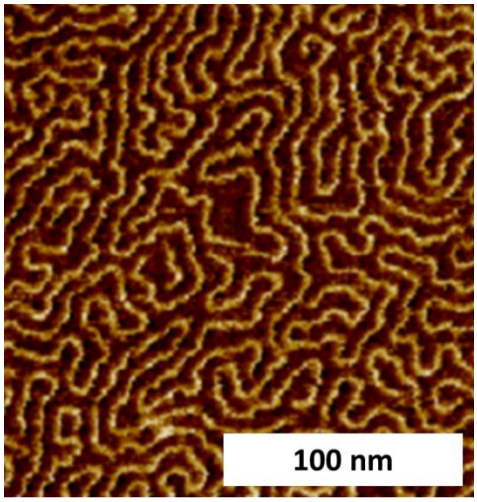

Figure 5.2: AFM of bottlebrushes. AFM height micrographs of PDMS bottlebrushes ($n_{bb} = 1200$ and $n_{sc} = 14$) deposited by spin casting on a mica substrate. The micrographs display individual worm-like molecules forming a dense film after. Molecular imaging was performed in PeakForce QNM mode using a multimode AFM (Brüker) with a NanoScope V controller and silicon probes (resonance frequency of 50-90 Hz and spring constant of ~0.4 N/m).

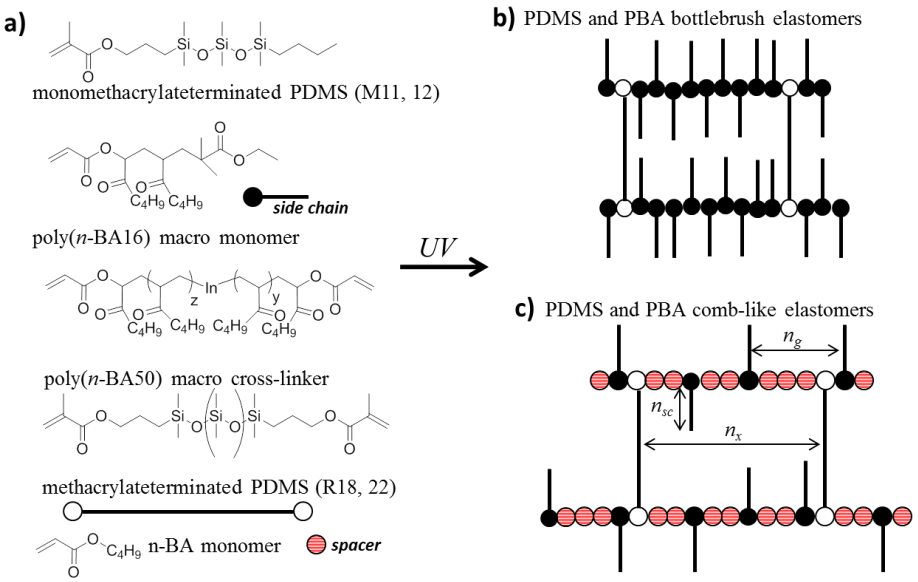

Figure 5.3: Synthesis of bottlebrush and comb elastomers. Synthesis of bottlebrush and comb-like PDMS and P*n*BA elastomers by photoinitiated radical polymerization of monofunctional macromonomers and diluent (nBA) in the presence of difunctional crosslinker. **a)** Chemical structure of macromonomers and cross-linkers and diluent, **b)** schematic of bottlebrush PDMS and P*n*BA elastomers, and **c)** schematic of comb PDMS and P*n*BA elastomers.

Table 5.1: Molecular characterization of PDMS bottlebrushes ($n_{sc} = 14$).

Sample	n_{bb} (NMR)[a]	n_{bb} (AFM) [b]	M_n (g/mol)	M_w (g/mol)	Đ (AFM) [b]
PDMS-600	600	585±40	585000	680000	1.16
PDMS-900	900	902±70	902000	1061000	1.18
PDMS-1200	1200	1163±90	1163000	1267000	1.08
PDMS-1500	1500	1315±100	1315000	1494000	1.14

[a] Number average degree of polymerization of bottlebrush backbone (n_{bb}) determined by ^{1}H-NMR, [b] n_{bb} and dispersity of bottlebrush backbone determined by AFM (Figure 5.2) as $n_{bb} = L_n/l_0$, where L_n is number average contour length and $l_0 = 0.25\ nm$ is the length of the monomeric unit. In-house software was used to measure the contour length. Typically, ensembles of 300 molecule were analyzed to ensure standard deviation of the mean below 10%.

5.2.2 AFM

Atomic force microscopy (AFM) samples were produced by spin-casting a 0.05 mg mL^{-1} PDMS bottlebrush solution onto a cleaved mica substrate at 2000 rpm for 1 min. Imaging of

individual molecules was performed in PeakForce QNM mode using a multimode AFM instrument (Brüker) equipped with a NanoScope V controller. Silicon probes were used with a resonance frequency of 50–90 Hz and a spring constant of ≈0.4 N/m.

5.2.3 NMR

The reactions were followed by ^{1}H-NMR ($CDCl_3$, Brüker 400 MHz spectrometer) of aliquots of reaction solution. The abundance of unreacted MMA was used to monitor the extent of reaction and the abundance of BA versus MMA was used to measure the evolution of the grafting density and found it to be accurate within 10% error of the reported values.

5.2.4 Stress-strain curves

To investigate the basic mechanical properties of the brush-like samples, the elastomer sample films were punched into dumbbell samples with bridge dimensions of 12 mm × 2 mm × 1–2 mm. The samples were loaded into an RSA-G2 DMA (TA Instruments) and subjected to a constant uniaxial tensile Hencky strain rate of 0.003 strain per second at 20 °C until rupture occurred. All bottlebrush films were subjected to triplicate testing to ensure accuracy of the data. The resulting stress strain curves were then analyzed with Equation 5.3 using Origin 2016 software.

5.3 Results

5.3.1 Library of polymers and mechanical testing

The possibility of synthetic material below the $G \sim \lambda_{max}^{-2}$ trend was first opened by addition of grafted side chains,[133, 79] which facilitated disentanglement of polymer melts[97] and unveiled the promise of brush-like architecture for making advanced elastomers,[27] thermos plastics,[102] and

molecular assemblies.[134,135] Fulfilling this potential, we established the foundational $[n_{sc}, n_g, n_x]$ triplet and transform the previously one-dimensional parameter space of synthetic elastomers into a vast multidimensional landscape of $E(\lambda_{max})$ correlations. In order to map this landscape, libraries of brush-like polydimethylsiloxane (PDMS) and poly(*n*-butylacrylate) (P*n*BA) elastomers were synthesized with precise and independently controlled sets of $[n_{sc}, n_g, n_x]$ (See Table 5.2). Mechanical testing in combination with analytical calculations used to characterize elasticity for broad frequency and strain ranges and to delineate universal correlations between $[n_{sc}, n_g, n_x]$ and the mechanical properties of the network libraries. Figure 5.4 displays the corresponding stress-strain curves.

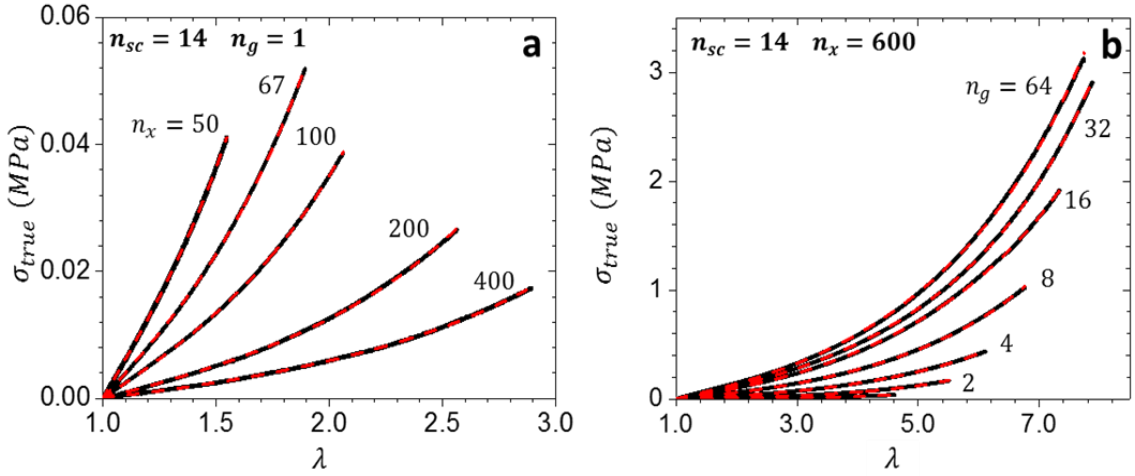

Figure 5.4: Tensile curves. **a)** Tensile true stress versus elongation $\lambda = L/L_0$ for PDMS bottlebrush elastomers with the same ($n_{sc} = 14$ and $n_g = 1$) and different DPs of the backbone in the bottlebrush network strand (as indicated). **b)** Tensile true stress versus elongation $\lambda = L/L_0$ for PDMS comb elastomers with the same ($n_x = 600$ and $n_{sc} = 14$) and different values of n_g as indicated. Each curve was collected via uniaxial extension of a 2×2×12 mm dog bone sample at $\dot{\varepsilon} = 0.002$ s^{-1}.

The curves were fit by Equation 5.3, with E and β as fitting parameters.

$$\sigma_{true}(\lambda) = \frac{E}{9}(\lambda^2 - \lambda^{-1})\left[1 + 2\left(1 - \frac{\beta(\lambda^2 + 2\lambda^{-1})}{3}\right)^{-2}\right] \qquad 5.3$$

At small deformations, Equation 5.3 relates the apparent (E_0) and structural (E) Young's moduli as

$$E_0 \equiv \lim_{\lambda \to 1} \frac{3\sigma_{true}(\lambda)}{\lambda^2 - \lambda^{-1}} = \frac{E}{3}(1 + 2(1-\beta)^{-2}) \qquad 5.4$$

Note that $E_0 \approx E$ for networks with flexible strands ($\beta \ll 1$). The resulting fitting parameters are collected in Table 5.2. The implications of this data will be discussed in the next section.

Table 5.2: Mechanical properties of PDMS bottlebrush and comb-like networks.

n_g	n_{sc}	n_x	E [kPa]*	E_e [kPa]*	β
1	14	400	3.3	N/A	0.08
1	14	200	8.4	N/A	0.11
1	14	100	18.6	N/A	0.17
1	14	67	30.0	N/A	0.23
1	14	50	40.5	N/A	0.28
1	14	600	2.6	N/A	0.066
2	14	600	7.9	N/A	0.032
4	14	600	24.6	1.2	0.027
8	14	600	42.9	20.1	0.022
16	14	600	60.3	45.0	0.017
32	14	600	70.8	66.0	0.017
64	14	600	79.5	84.0	0.015

*E represents the structural Young's modulus extracted by fitting $\sigma_{true}(\lambda)$ curves with Equation 5.3. E_e represents the modulus contribution from trapped entanglements by fitting with $\sigma_{true}(\lambda) = \frac{E}{9}(\lambda^2 - \lambda^{-1})\left[1 + \frac{9E_e}{E\lambda} + 2\left(1 - \frac{\beta(\lambda^2 + 2\lambda^{-1})}{3}\right)^{-2}\right]$.

5.3.2 New mechanical relations

Tensile tests of the PDMS libraries revealed four distinct correlations between E and λ_{max} as diagrammed by arrows i-iv in Figure 5.5a. The arrows respectively represent: (i) conventional decrease of E with λ_{max}, (ii) unprecedented concurrent increase of E and λ_{max}, (iii) regulation of E at constant λ_{max}, and (iv) regulation of λ_{max} at constant E (shown respectively in Figure 5.5c-

f). These correlations are particularly unique given the libraries' solvent less, single-component compositions. Summarized in Figure 5.5g, the diversity of corresponding phenotypes suggests that nearly any $[E, \lambda_{max}]$ pair can be realized through formulaic variation of the $[n_{sc}, n_g, n_x]$ triplet. This ability of brush-like elastomers to independently regulate E and λ_{max} is visualized by plotting $E\lambda_{max}^2$ versus n_g (Figure 5.5h). Unlike linear-chain elastomers, where all $E(\lambda_{\max})$ correlations collapse into a single point (i.e., $E\lambda_{max}^2 =$ constant), brush-like systems (exemplified here by PDMS systems with $n_{sc} = 14$) collapse onto a universal line defined by the independent control of property correlations and, thus, embody a unique opportunity for engineering specific mechanical responses in much wider range than was previously possible in a single component system.

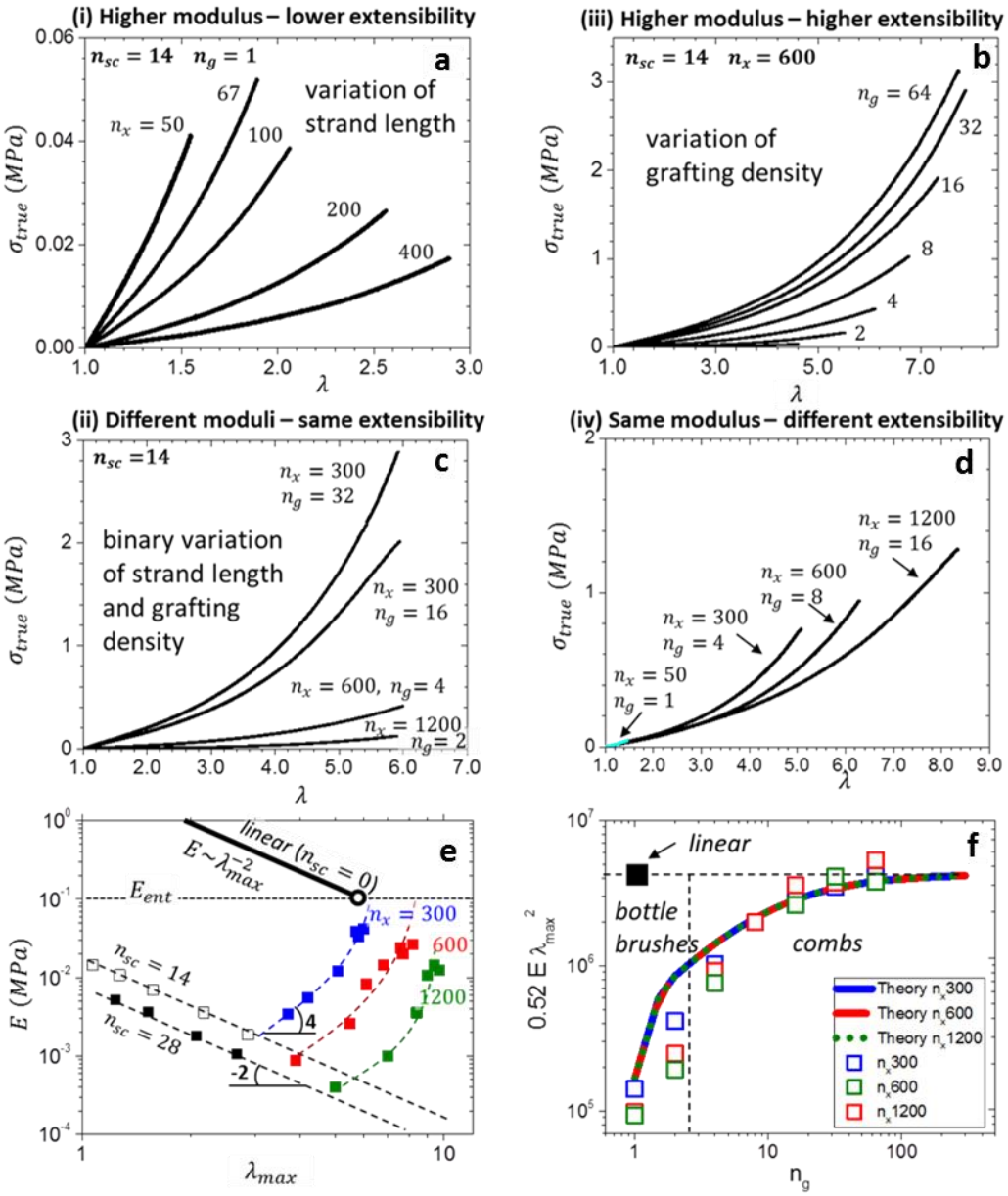

Figure 5.5: Novel mechanical relations. **a)** conventional covariation of E and λ_{max}, **b)** simultaneous increase of E and λ_{max}, **c)** variation of E at constant λ_{max}, and **d)** variation of λ_{max} at constant E. **e)** Summary of the measured $E(\lambda_{\max})$ trends including scaling relationships. **f)** Plot of $0.52E\lambda_{max}$ versus n_g illustrating the higher-dimensional nature of brush-like architectures relative to linear-chain elastomers.

5.4 Conclusion and outlook

The above chapters discuss the properties and applications of brush-like materials while individually varying one of the indices in the $[n_{sc}, n_g, n_x]$ triplet. These architectures displayed the potential for supersoft elastomers with high extensibilities and strong strain hardening potentials. In this chapter, all aspects of the brush-like architecture were brought together to form a complete understanding of the architecture. A series of materials varying all three aspects of the $[n_{sc}, n_g, n_x]$ triplet were synthesized and used to experimentally verify an expanded list of modulus extensibility relations. Breaking free from the "*Golden Rule*", the brush-like architectures allow for property combinations formerly belonging to biological materials. This opens up entirely new categories of dry and functional biological mimics.

Moving forward, brush-like architecture still possess a number of interesting properties to explore. These structures are known to be supersoft, extensible, and have strong strain hardening potential, but there is unexplored potential in the damping properties of these materials seen in Chapter 1 where the bottlebrushes display large frequency ranges of high tangent delta (G''/G'). This property has the potential to be employed in next generation sound absorbing materials and adhesives. As seen above, the brush-like architecture achieves a wide range of properties within a single chemistry, but altering the chemistry opens opportunities for new materials with specialized responsive and adaptive properties. In the immediate future the work presented in Chapter 5 will be used to establish a set of universal rules wherein mechanical behavior can be analyzed using Equation 5.3 and reproduced via a program brush-like mimic. To build on this the effects of chemical interactions and physical crosslinking seen in Chapter 4 will be added to the complexity of control mechanisms. I believe that this body of work has successfully laid the ground work for this ambitious future project and represents a significant addition to the field of materials research.

REFERENCES

[1] Brandrup, J.; Immergut, E.H. "Polymer Handbook, 4th Edition" Wiley-Interscience (1999).

[2] Takayanagi, M; Ogata, T.; Morikawa, M.; Kai, T. Polymer composites of rigid and flexible molecules: system of wholly aromatic and aliphatic polyamides. *J. Macromol. Sci. Phys.* **1980**,*17*, 591-615.

[3] Paul, D.R.; Robeson, L.M. Polymer nanotechnology: Nanocomposites. *Polymer* **2008**, *49*, 3187-3204.

[4] Bokobza, L. The Reinforcement of Elastomeric Networks by Fillers. *Macromol. Mater. Eng.* **2004**, *289*, 607-621.

[5] Ruiz-Perez, L.; Royston, G.J.; Fairclough, J.P.A.; Ryan, A.J. Toughening by nanostructure. *Polymer* **2008**, *49*, 4475-4488.

[6] Kushner, A.M.; Guan, Z.B. Modular Design in Natural and Biomimetic Soft Materials *Angew. Chem., Int. Ed.* **2011**, *50*, 9026-9057.

[7] Ahmed, S.; Jones, F.R. A review of particulate reinforcement theories for polymer composites. *Journal of Material Science* **1990**, *25*, 4933-4942.

[8] Edwards, D.C. Review polymer-filler interactions in rubber reinforcement. *Journal of Material Science* **1990**, *25*, 4175-4185.

[9] Bakis, C.; Bank, L.; Brown, V.; Cosenza, E.; Davalos, J.; Lesko, J.; Machida, A.; Rizkalla, S.; Triantafillou, T. Fiber-reinforced polymer composite for construction-state-of-the-art review. *J. Compos. Constr.* **2002**, *6*, 73-87.

[10] Lewis, T.B.; Nielsen L.E. Dynamic mechanical properties of particulate-filled composites *Journal of Applied Polymer Science* **1970**, *6*, 1449-1471.

[11] Wisse, E.; Govaert, L.E.; Meijer, H.E.H.; Meijer, E.W. Unusual Tuning of Mechanical Properties of Thermoplastic Elastomers Using Supramolecular Fillers. *Macromolecules* **2006**, *39*, 7425-7432.

[12] Fung, Y.C. "Biomechanics: Mechanical Properties of Living Tissues" 2nd ed, Springer-Verlag, New York (1993).

[13] Wellman, P.; Howe, R.D.; Dalton E.; Kern, K. "Breast tissue stiffness in compression is correlated to histological diagnosis" Harvard Biorobotics Laboratory Technical Report (1999).

[14] Gefen, A.; Dilmoney, B. Mechanics of the normal woman's breast *Technol. Health Care* **2007**, *15*, 259-271.

[15] Newman, J. Review of soft tissue augmentation in the face. *Clinical, Cosmetic and Investigational Dermatology* **2009**, *2*, 141-150.

[16] Levental, I.; Georges, P.C.; Janmey, P.A. Soft biological materials and their impact on cell function. *Soft Matter* **2007**, *3*, 299-306.

[17] Zemel, A,; Rehfeldt, F.; Brown, A.E.X.; Discher, D.E.; Safran, S.A. Optimal matrix rigidity for stress-fibre polarization in stem cells. *Nature Phys*. **2010**, 6, 468-473.

[18] Wang, H.B.; Dembo, M.; Wang, Y.L. Substrate flexibility regulates growth and apoptosis of normal but not transformed cells. *Am. J. Physiol. Cell Phisiol.* **2000**, *279*, C1345-C1350.

[19] Pelham, R.J.; Wang, Y.I. Cell locomotion and focal adhesion are regulated by substrate flexibility *PNAS* **1997**, *94*, 13661-13665.

[20] Hoffman, B.D.; Grashoff, C.; Schwartz, M.A. Dynamic molecular processes mediate cellular mechanotransduction. *Nature* **2011**, *475*, 316-323.

[21] Discher, D.E.; Janmey, P.; Wang, Y.L. Tissue cells feel and respond to the stiffness of their substrate. *Science* **2005**, *310*, 1139-1143.

[22] Swift, J.; Ivanovska, I.L.; Buxboim, A.; Harada, T.; Dingal, P.C.D.P.; Pinter, J.; Pajerowski, J.D.; Spinler, K.; Shin, J.W.; Tewari, M.; Rehfeldt, F.; Speicher, D.W.; Discher, D.E. Nuclear Lamin-A Scales with Tissue Stiffness and Enhances Matrix-directed Differentiation *Science* **2013**, *341*, 1240104/1-5.

[23] Lichter, J.A.; Thompson, M.T.; Delgadillo, M.; Nishikawa, T.; Rubner, M.F.; Van Vliet, K.J. Substrata mechanical stiffness can regulate adhesion of viable bacteria. *Biomacromolecules* **2008**, *9*, 1571-1578.

[24] Dorel, C. Manipulating bacterial cell fate: Key role of surface-sensing and signal transduction. *Current Research, Technology and Education Topics in Applied Microbiology and Microbial Biotechnology* **2010**, *2*, 791-800.

[25] Brady Jr., R.F. Properties which influence marine fouling resistance in polymers containing silicon and florine. *Prog. Org. Coat*. **1999**, *35*, 31-35.

[26] Brady Jr., R.F. A fracture mechanical analysis of fouling release from nontoxic antifouling coatings. *Prog. Org. Coat*. **2001**, 43, 188-192.

[27] Vatankhah-Varnoosfaderani, M.; Daniel, W. F. M. ; Zhushma, A. P.; Li, Q.; Morgan, B. J.; Matyjaszewski, K.; Armstrong, D. P.; Spontak, R. J.; Dobrynin, A. V.; Sheiko, S. S., Bottlebrush Elastomers: A New Platform for Freestanding Electroactuation. *Adv Mater* **2017,** *29*, 1604209(1-7).

[28] Chen, Q.; Liang, S.; Thouas, G. A., Elastomeric biomaterials for tissue engineering. *Progress in polymer science* **2013,** *38* (3), 584-671.

[29] Hines, L.; Petersen, K.; Lum, G. Z.; Sitti, M., Soft Actuators for Small-Scale Robotics. *Adv Mater* **2017**, *29*, 1603483 (1-43).

[30] Majidi, C., Soft robotics: a perspective—current trends and prospects for the future. *Soft Robotics* **2014,** *1*, 5-11.

[31] Trivedi, D.; Rahn, C. D.; Kier, W. M.; Walker, I. D., Soft robotics: Biological inspiration, state of the art, and future research. *Applied Bionics and Biomechanics* **2008,** *5*, 99-117.

[32] Kim, S.; Laschi, C.; Trimmer, B., Soft robotics: a bioinspired evolution in robotics. *Trends in biotechnology* **2013,** *31*, 287-294.

[33] Cianchetti, M.; Ranzani, T.; Gerboni, G.; Nanayakkara, T.; Althoefer, K.; Dasgupta, P.; Menciassi, A., Soft robotics technologies to address shortcomings in today's minimally invasive surgery: the STIFF-FLOP approach. *Soft Robotics* **2014,** *1*, 122-131.

[34] Lu, N.; Kim, D.-H., Flexible and stretchable electronics paving the way for soft robotics. *Soft Robotics* **2014,** *1*, 53-62.

[35] Pfeifer, R.; Lungarella, M.; Iida, F., The challenges ahead for bio-inspired'soft'robotics. *Communications of the ACM* **2012,** *55*, 76-87.

[36] Lipson, H., Challenges and opportunities for design, simulation, and fabrication of soft robots. *Soft Robotics* **2014,** *1*, 21-27.

[37] Stokes, A. A.; Shepherd, R. F.; Morin, S. A.; Ilievski, F.; Whitesides, G. M., A hybrid combining hard and soft robots. *Soft Robotics* **2014,** *1*, 70-74.

[38] Kim, S.; Hawkes, E.; Choy, K.; Joldaz, M.; Foleyz, J.; Wood, R. In *Micro artificial muscle fiber using NiTi spring for soft robotics*, 2009 IEEE/RSJ International Conference on Intelligent Robots and Systems, IEEE: 2009; pp 2228-2234.

[39] Rossiter, J.; Walters, P.; Stoimenov, B. In *Printing 3D dielectric elastomer actuators for soft robotics*, SPIE Smart Structures and Materials+ Nondestructive Evaluation and Health Monitoring, International Society for Optics and Photonics: 2009; pp 72870H-72870H-10.

[40] Shepherd, R. F.; Ilievski, F.; Choi, W.; Morin, S. A.; Stokes, A. A.; Mazzeo, A. D.; Chen, X.; Wang, M.; Whitesides, G. M., Multigait soft robot. *Proceedings of the National Academy of Sciences* **2011,** *108*, 20400-20403.

[41] Zdrahala, R. J.; Zdrahala, I. J., Biomedical applications of polyurethanes: a review of past promises, present realities, and a vibrant future. *Journal of biomaterials applications* **1999,** *14*, 67-90.

[42] Picha, G. J., Infusion device for soft tissue. U.S. Patent 5564439: 1996.

[43] Bezwada, R. S.; Scopelianos, A. G., Elastomeric medical device. U.S. 5,468,253: 1995.

[44] Mirfakhrai, T.; Madden, J. D.; Baughman, R. H., Polymer artificial muscles. *Materials today* **2007,** *10*, 30-38.

[45] Rogers, J. A.; Someya, T.; Huang, Y., Materials and mechanics for stretchable electronics. *Science* **2010,** *327*, 1603-1607.

[46] Tarascon, J.-M.; Armand, M., Issues and challenges facing rechargeable lithium batteries. *Nature* **2001,** *414*, 359-367.

[47] Nicholls, H. R.; Lee, M. H., A survey of robot tactile sensing technology. *The International Journal of Robotics Research* **1989,** *8*, 3-30.

[48] Liu, W.-R.; Yang, M.-H.; Wu, H.-C.; Chiao, S.; Wu, N.-L., Enhanced cycle life of Si anode for Li-ion batteries by using modified elastomeric binder. *Electrochemical and Solid-State Letters* **2005,** *8*, A100-A103.

[49] Owen, J. R., Rechargeable lithium batteries. *Chemical Society Reviews* **1997,** *26*, 259-267.

[50] Aurbach, D.; Zinigrad, E.; Cohen, Y.; Teller, H., A short review of failure mechanisms of lithium metal and lithiated graphite anodes in liquid electrolyte solutions. *Solid state ionics* **2002,** *148*, 405-416.

[51] Novák, P.; Müller, K.; Santhanam, K.; Haas, O., Electrochemically active polymers for rechargeable batteries. *Chemical Reviews* **1997,** *97*, 207-282.

[52] Pelrine, R.; Kornbluh, R.; Joseph, J.; Heydt, R.; Pei, Q.; Chiba, S., High-field deformation of elastomeric dielectrics for actuators. *Materials Science and Engineering: C* **2000,** *11*, 89-100.

[53] Patel, S.K.; Malone, S.; Cohen, C.; Gillmor, J.R.; Colby, R.H. Elastic modulus and equilibrium swelling of poly(dimethylsi1oxane) networks. *Macromolecules* **1992**, *25*, 5241-5251.

[54] Everaers, R. "Entanglement effects in defect-free model polymer networks" *New Journal of Physics* **1999**, *1*, 12.1-12.54.

[55] Rubinstein, M.; Colby, R.H. "Polymer Physics-Ch.7" Oxford University Press, New York (2003).

[56] Larson, R.G.; Sridhar, T.; Leal, L.G.; McKinley, G.H.; Likhtman, A.E.; McLeish, T.C.B. Definitions of entanglement spacing and time constants in the tube model. *J. Rheol.* **2003**, *47*, 809-818.

[57] Peppas, N.A.; Bures, P.; Leobandung, W.; Ichikawa, H. Hydrogels in pharmaceutical formulations. *European Journal of Pharmaceutics and Biopharmaceutics* **2000**, *50*, 27-48.

[58] Lee, K. Y.; Mooney, D. J. Hydrogels for tissue engineering. *Chem. Rev*. **2001**, 101, 1869–1879.

[59] Dong, L.; Agarwal, A. K.; Beebe, D. J.; Jiang, H. R. Adaptive liquid microlenses activated by stimuli-responsive hydrogels. *Nature* **2006**, *442*, 551–554.

[60] Qiu, Y.; Park, K. Environmnet-responcive hydrogels for drug delivery. *Advanced Drug Delivery Reviews* **2012**, 64, 49-60.

[61] Calvert, P. Hydrogels for soft machines *Adv. Mater.* **2009**, *21*, 743-756.

[62] Bastide, J.; Leibler, L. Large-Scale Heterogeneities in Randomly Cross-Linked Networks. *Macromolecules* **1988**, *21*, 2647-2649.

[63] Ker, R.F. The design of soft collagenous load-bearing tissues. *J. Exp. Biol.* **1999**, *202*, 3315-3324.

[64] Carstensen, E.L.; McKay, N.D.; Dalecki, D.; Muir, T.G. Absorption of finite amplitude ultrasound in tissues. *Acustica* **1982**, *1*, 116-123.

[65] Carstensen, E.D; Bacon, D.R. "Biomedical Applications in Nonlinear Acoustics" Eds. Hamilton, M.; Blackstock, D.T 2nd Ed., Academic Press, 421 (1998).

[66] Culjat, M.O.; Goldenberg, D.; Tewari, P; Singh, R.S. "A Review of Tissue Substitutes for Ultrasound Imaging" *Ultrasound in Medicine & Biology* **2010**, *36*, 861-873.

[67] Zagzebski, J.A. "Essentials of Ultrasound Physics" Mosby Inc. (1996).

[68] Edwards, S. F.; Doi, M. "The theory of polymer dynamics." (Oxford Univ. Press, New York 1986).

[69] de Gennes, P. G. J. Reptation of a polymer chain in the presence of fixed obstacles. *Chem Phys* **1971**, *55*, 572-579.

[70] Kavassalis, T. A.; Noolandi, J. Entanglement scaling in polymer melts and solutions. *Macromolecules* **1989**, *22*, 2709-2720.

[71] Landau, L.D.; Lifshitz, E.M Course of theoretical physics Vol 7: Theory of Elasticity (Pergamon Press, Oxford 1986).

[72] Boal, D.H. Mechanics of cell (Cambridge University Press, Cambridge 2002 2nd Ed).

[73] Zhen, C.; Carillo, J.M.; Sheiko, S.S.; Dobrynin, A.V. Computer simulations of bottlebrushes: From melts to soft networks. *Macromolecules* **2015**, *48*, 5006-5015.

[74] Paturej, J.; Sheiko, S.S,; Panyukov, S.; Rubinstein, M. Molecular structure of bottlebrush polymers in melts. *Sci, Adv*. **2016**, *2*, 1-12.

[75] Inkson, N. J.; Graham, R. S.; McLeish, T. C. B.; Groves, D. J.; Fernyhough, C. M. Viscoelasticity of monodisperse comb polymer melts. *Macromolecules* **2006**, *39*, 4217-4227.

[76] Kapnistos, M.; Vlassopoulos, D.; Roovers, J.; Leal, L.G. Linear rheology of architecturally complex macromolecules: comb polymers with linear backbones. *Macromolecules* **2005**, *38*, 7852-7862.

[77] Fetters, L. J.; Lohse, D. J.; Garcia-Franco, C. A.; Brant, P.; Richter, D. Prediction of melt state Poly(R-olefin) rheological properties: the unsuspected role of the average molecular weight per backbone bond. *Macromolecules* **2002**, *35*, 10096-10101.

[78] Yamazaki, H. et al. Dynamic viscoelasticity of poly(butyl acrylate) elastomers containing dangling chains with controlled lengths. *Macromolecules*. **2011**, *44*, 8829-8834.

[79] Pakula, T. et al. Molecular brushes as super-soft elastomers. *Polymer* **2006**, *47*, 7198-7206.

[80] Hu, M.; Xia, Y.; McKenna, G. B.; Kornfield, J. A.; Grubbs, R. H. Linear rheological response of a series of densely branched brush polymers. *Macromolecules* **2011**, *44*, 6935-6943.

[81] Dalsin, S. J.; Hillmyer, M. A.; Bates, F. S. Linear rheology of polyolefin-based bottlebrush polymers. *Macromolecules* **2015**, *48*, 4680-4691.

[82] Sheiko, S. S. et al. Measuring molecular weight by atomic force microscopy. *J. Am. Chem. Soc.* **2003**, *125*, 6725-6728.

[83]Panyukov, S. V.; Zhulina, E. B.; Sheiko, S. S.; Randall, G.; Brock, J.; Rubinstein, Tension amplification in molecular brushes in solutions and on substrates. *J. Phys. Chem. B* **2009**, *113*, 3750-3768.

[84]Williams, M. L., Landel, R. F. & Ferry J. D. The time dependence of relaxation mechanisms in amorphous polymers and other glass-forming liquids. *J. Am. Chem. Soc.* **77**, 3701–3707 (1955).

[85]Lomellini P. Effect of chain length on the network modulus and entanglement. *Polymer* **33**, 1255-1259 (1992).

[86]van Gurp, M. & Palmen, J. Time-temperature superposition for polymeric blends. *Rheol. Bull.* **67**, 5-8 (1998).

[87]Rubinstein, M. & Colby, R. H. *Polymer Physics* Ch.7 (Oxford Univ. Press, New York 2003).

[88]des Cloizeaux, J. Double reptation vs. simple reptation in polymer melts. *Europhys. Lett.* **5**, 437 (1988).

[89] Sun, T. L. *et al.* Physical hydrogels composed of polyampholytes demonstrate high toughness and viscoelasticity. *Nature Mater.* **2013**, *12*, 932–937.

[90] Xu, H.; Shirvaniants, D.; Beers, K.; Matyjaszewski, K.; Rubinstein, M.; Sheiko, S.S. Molecular Motion in a Spreading Precursor Film. *Phys. Rev. Lett.* **2004**, *93*, 206103/1-4.

[91] Xu, H.; Sheiko, S.S.; Shirvaniants, D.; Rubinstein, M.; Beers, K.L.; Matyjaszewski, K. Flow Induced Epitaxial Ordering of Brush-Like Macromolecules on Graphite. *Langmuir* **2006**, *22*, 1254-1259.

[92] Xu, H.; Shirvaniants, D.; Rubinstein, M.; Shabratov, D.; Beers, K.; Matyjaszewski, K.; Sheiko, S.S. Molecular Pressure Sensors. *Advanced Materials* **2007**, *19*, 2930-2934.

[93] Xu, H.; Shirvanyants, D.; Beers, K.L.; Matyjaszewski, K.; Dobrynin, A.V.; Rubinstein, M.; Sheiko, S.S. Molecular Visualization of Conformation-Triggered Flow Instability. *Phys. Rev. Lett.* **2005**, *94*, 237801/1-4.

[94] Sheiko, S.S.; Sun, F.C.; Randal, A.; Shirvaniants, D.; Matyjaszewski, K.; Rubinstein, M. Adsorption-Induced Scission of Carbon-Carbon Bonds. *Nature* **2006**, *440*, 191-194.

[95] Lebedeva, N.V.; Sun, F.C.; Lee, H.I.; Matyjaszewski, K.; Sheiko, S.S. Fatal Adsorption of Brush–Like Macromolecules: High Sensitivity of C–C Bond Cleavage Rates to Substrate Surface Energy. *J. Am. Chem. Soc.* **2008**, *130*, 4228-4229.

[96] Park, I.; Shirvanyants, D.; Nese, A.; Matyjaszewski, K.; Rubinstein, M.; Sheiko, S.S. Spontaneous and Specific Activation of Chemical Bonds in Macromolecular Fluids. *J. Am. Chem. Soc.* **2010**, *132*, 12487-12491.

[97] Daniel, W. F. M.; Bodynska, J.; Vatankhan-Varnoosfaderani, M.; Matyjaszewski, K.; Paturej, J.; Rubinstein, M.; Dobrynin, A., V.; Sheiko, S. S. Ultrasoft, Superelastic Solvent-free Elastomers. *Nat. Mater.* **2016**, *15*, 183-189.

[98]Dobrynin, A. V.; Carrillo, J. M. Y. Universality in Nonlinear Elasticity of Biological and Polymeric Networks and Gels Macromolecules **2011**, *44*, 140-146.

[99] Romasanta, L. J.; Lopez-Manchado, M. A.; Verdejo, R. Increasing the performance of dielectric elastomer actuators: A review from the materials perspective *Prog. Polym. Sci.* **2015**, *51*, 188-211.

[100] Ha, S. M.; Yuan, W.; Pei, Q.; Pelrine, R.; Stanford, S. Interpenetrating Polymer Networks for High-Performance Electroelastomer Artificial Muscles. *Adv. Mater.* **2006**, *18*, 887-891.

[101] Opris, D. M.; Molberg, M.; Walder, C.; Ko, Y. S.; Fischer, B.; Nüesch, F. A. New Silicone Composites for Dielectric Elastomer Actuator Applications in Competition with Acrylic Foil. *Adv. Funct. Mater.* **2011**, *21*, 3531-3539.

[102] Bates, F. S.; Fredrickson, G. H. Block Copolymer Thermodynamics: Theory and Experiment. *Annu. Rev. Phys. Chem.* **1990**, *41*, 525-557.

[103] Kim, S. H.; Misner, M. J.; Xu, M. K.; Russell, T. P. Highly Oriented and Ordered Arrays from Block Copolymers via Solvent Evaporation. *Adv. Mater.* **2004**, *16*, 226-233.

[104] Koo, C. M.; Wu, L.; Lim, L. S.; Mahanthappa, M. K.; Hillmyer, M. A.; Bates, F. S. Microstructure and Mechanical Properties of Semicrystalline–Rubbery–Semicrystalline Triblock Copolymers. *Macromolecules* **2005**, *38*, 6090-6098.

[105] Sheiko, S. S.; Sumerlin, B. S.; Matyjaszewski, K. Cylindrical Molecular Brushes: Synthesis, Characterization, and Properties. *Prog. Polym. Sci.* **2008**, *33*, 759-785.

[106] Mukumoto, K.; Li, Y.; Nese, A.; Sheiko, S.S.; Matyjaszewski, K. Synthesis and Characterization of Molecular Bottlebrushes Prepared by Iron Based ATRP. *Macromolecules* **2012**, *45*, 9243-9249.

[107] Jha, S.; Dutta, S.; Bowden, N. B. Synthesis of Ultralarge Molecular Weight Bottlebrush Polymers Using Grubbs' Catalysts. *Macromolecules* **2004**, *37*, 4365–4374.

[108] Xie, G.; Ding, H.; Daniel, W. F. M.; Wang, Z.; Pietrasik, J.; Sheiko, S. S.; Matyjaszewski, K. Preparation of Titania Nanoparticles with Tunable Anisotropy and Branched Structures from Core–Shell Molecular Bottlebrushes. *Polymer* **2016,** *98*, 481-486.

[109] Lee, H. i.; Pietrasik, J.; Sheiko, S. S.; Matyjaszewski, K. Stimuli-Responsive Molecular Brushes. *Prog. Polym. Sci.* **2010,** *35*, 24-44.

[110] Banquy, X.; Burdyńska, J.; Lee, D. W.; Matyjaszewski, K.; Israelachvili, J. Bioinspired Bottle-Brush Polymer Exhibits Low Friction and Amontons-like Behavior. *J. Am. Chem. Soc.* **2014,** *136*, 6199-6202.

[111] Müllner, M.; Müller, A. H. E. Cylindrical Polymer Brushes – Anisotropic Building Blocks, Unimolecular Templates and Particulate Nanocarriers. *Polymer* **2016**, *98*, 389-401.

[112] Verduzco, R.; Li, X.; Pesek, S. L.; Stein, G. E. Structure, function, self-assembly, and applications of bottlebrush copolymers. *Chem. Soc. Rev.* **2015**, *44*, 2405-2420.

[113] Bates, C. M.; Chang, A. B.; Momčilović, N.; Jones, S. C.; Grubbs, R. H. ABA Triblock Brush Polymers: Synthesis, Self-Assembly, Conductivity, and Rheological Properties. *Macromolecules* **2015,** *48*, 4967-4973.

[114] Fenyves, R.; Schmutz, M.; Horner, I. J.; Bright, F. V.; Rzayev, J. Aqueous Self-Assembly of Giant Bottlebrush Block Copolymer Surfactants as Shape-Tunable Building Blocks. *J. Am. Chem. Soc.* **2014**, *136*, 7762-7770.

[115] Dalsin, S. J.; Rions-Maehren, T. G.; Beam, M. D.; Bates, F. S.; Hillmyer, M. A.; Matsen, M. W. Bottlebrush Block Polymers: Quantitative Theory and Experiments. *ACS Nano* **2015**, *9*, 12233–12245.

[116] Xia, Y.; Olsen, B. D.; Kornfield, J. A.; Grubbs, R. H. Efficient Synthesis of Narrowly Dispersed Brush Copolymers and Study of Their Assemblies: The Importance of Side Chain Arrangement. J. Am. Chem. Soc. **2009**, *131*, 18525−18532.

[117] Stals, P. J. M.; Li, Y.; Burdyńska, J.; Nicolaÿ, R.; Nese, A.; Palmans, A. R. A.; Meijer, E. W.; Matyjaszewski, K.; Sheiko, S. S. How Far Can We Push Polymer Architectures? *J. Am. Chem. Soc.* **2013,** *135*, 11421-11424.

[118] Zhang, J.; Schneiderman, D. K.; Li, T.; Hillmyer, M. A.; Bates, F. S. Design of Graft Block Polymer Thermoplastics. *Macromolecules*, **2016**, *49*, 9108–9118.

[119] Zhang, J.; Li, T.; Mannion, A. M.; Schneiderman, D. K.; Hillmyer, M. A.; Bates Tough and Sustainable Graft Block Copolymer Thermoplastics. *ACS Macro Lett.*, **2016**, *5*, 407–412.

[120] Onbulak, S.; Rzayev, J. Cylindrical Nanocapsules from Photo-Cross-Linkable Core–Shell Bottlebrush Copolymers. *Polym. Chem.* **2015**, *6*, 764-771.

[121] Takano, A.; Kamaya, I.; Takashi, Y.; Matsushita, Y. Effect of Loop/Bridge Conformation Ratio on Elastic Properties of the Sphere-Forming ABA Triblock Copolymers: Preparation of Samples and Determination of Loop/Bridge Ratio. *Macromolecules* **2005**, *38*, 9718-9723.

[122] Matsushita, Y.; Nomura, M.; Watanabe, J.; Mogi, Y.; Noda, I.; Imai, M. Alternating Lamellar Structure of Triblock Copolymers of the ABA Type. *Macromolecules* **1995**, *28*, 6007-6013.

[123] Milner, T. S.; Witten, A. T. Bridging Attraction by Telechelic Polymers. *Macromolecules*, **1992**, *25*, 5495–5503.

[124] Nguyen-Misra, M.; Mattice, W. L. Micellization and Gelation of Symmetric Triblock Copolymers with Insoluble End Blocks. *Macromolecules*, **1995**, *28*, 1444–1457.

[125] Qin, S.; Matyjaszewski, K.; Xu, H.; Sheiko, S. S. Synthesis and Visualization of Densely Grafted Molecular Brushes with Crystallizable Poly(octadecyl methacrylate) Block Segments. *Macromolecules* **2003**, *36*, 605-612.

[126] Yu-Su, S.; Sheiko, S.S.; Lee, H.-il; Jakubowski, W.; Nese, A,; Matyjaszewski, K.; Anokhin, D.; Ivanov, D.I. Crystallization of Molecular Brushes with Block Copolymer Side Chains. *Macromolecules* **2009**, *42*, 9008-9017.

[127] Wang, J. S.; Matyjaszewski, K. Controlled/"Living" Radical Polymerization. Atom Transfer Radical Polymerization in the Presence of Transition-Metal Complexes. *J. Am. Chem. Soc.*, **1995**, *117*, 5614–5615.

[128] Matyjaszewski, K.; Xia, J. Atom Transfer Radical Polymerization. *Chem. Rev*. **2001,** *101*, 2921-2990.

[129] Burdyńska, J.; Daniel, W.; Li, Y.; Robertson, B.; Sheiko, S. S.; Matyjaszewski, K. Molecular Bottlebrushes with Bimodal Length Distribution of Side Chains. *Macromolecules* **2015**, *48*, 4813−4822.

[130] Lee, J. L.; Kwei, T. K. Side-Chain Crystallization in Alkyl-Substituted Semiflexible Polymers, *Macromolecules* **1997**, *30*, 6877-6883.

[131] Plate, N. A. and Shibaev, V. P. 'Comb-Shaped Polymers and Liquid Crystals,' Plenum Press, New York, 1987, 1-104.

[132] Patel, S. K.; Malone, S.; Cohen, C.; Gillmor, J. R.; Colby, R. H. Elastic modulus and equilibrium swelling of poly(dimethylsiloxane) networks. *Macromolecules* **1992**, *25*, 5241-5251.

[133] Fetters, L. J.; Lohse, D. J.; García-Franco, C. A.; Brant, P.; Richter, D. Prediction of Melt State Poly(α-olefin) Rheological Properties: The Unsuspected Role of the Average Molecular Weight per Backbone Bond. *Macromolecules* **2002**, *35*, 10096-10101.

[134] Xia, Y., Olsen, B. D., Kornfield, J. A. & Grubbs, R. H. Efficient synthesis of narrowly dispersed brush copolymers and study of their assemblies: the importance of side chain arrangement. *J. Am. Chem. Soc.*, **2009**, *131*, 18525–18532.

[135] Bolton, J. & Rzayev, J. Synthesis and Melt Self-Assembly of PS–PMMA–PLA Triblock Bottlebrush Copolymers. *Macromolecules* **2014**, *47*, 2864-2874.